The European Master in Advanced Structural Analysis and Design using Composite Materials is a join initiative of:

Universidade do Minho

Universitat de Girona

Università degli Studi di Napoli Federico II

INSA Institut National des Sciences Appliquées Toulouse

Université de Toulouse

Assessment of Ply Joint Configurations in the Production of Composite Laminates Derived from Wind Turbine Blade Waste

Alvaro Souviron Vicente

FRP++ Advanced structural analysis and design using composite materials

UMinho | 2026

Universidade do Minho
Escola de Engenharia

Alvaro Souviron Vicente

Assessment of Ply Joint Configurations in the Production of Composite Laminates Derived from Wind Turbine Blade Waste

FRP++
Advanced structural analysis and design using composite materials

Funded by the European Union

September 2026

Universidade do Minho
Escola de Engenharia

Alvaro Souviron Vicente

Assessment of Ply Joint Configurations in the Production of Composite Laminates Derived from Wind Turbine Blade Waste

FRP++
Advanced structural analysis and design using composite materials

Master Dissertation
European Master Advanced Structural Analysis and Design using Composite Materials

Work developed under the supervision of
Professor Doctor José Sena Cruz
Doctor Luís Correia

Funded by the European Union

September 2026

DIREITOS DE AUTOR E CONDIÇÕES DE UTILIZAÇÃO DO TRABALHO POR TERCEIROS

Este é um trabalho académico que pode ser utilizado por terceiros desde que respeitadas as regras e boas práticas internacionalmente aceites, no que concerne aos direitos de autor e direitos conexos.

Assim, o presente trabalho pode ser utilizado nos termos previstos na licença abaixo indicada.

Caso o utilizador necessite de permissão para poder fazer um uso do trabalho em condições não previstas no licenciamento indicado, deverá contactar o autor através do RepositóriUM da Universidade do Minho.

Licença concedida aos utilizadores deste trabalho



Atribuição CC BY

https://creativecommons.org/licenses/by/4.0/

ACKNOWLEDGEMENTS

This work was supported by the R&D Project "CirWind-Development of innovative sustainable urban furniture and equipment in composites from waste produced by the wind energy industry for circularity", project no. 15232, operation code COMPETE203-FEDER-00889600, co-funded by Innovation and Digital Transition Program (COMPETE 2030), by Portugal 2030 and the European Union, in its FEDER component.

The student would like to gratefully acknowledge the financial support provided by the European Union for participation in the Erasmus Mundus FRP++ European Master Course in Advanced Structural Analysis and Design using Composite Materials (Project no. 101048961). This work was also supported by FCT/MCTES under the R&D Unit Institute for Sustainability and Innovation in Structural Engineering (ISISE), under the references UID/4029/2025 (DOI: 10.54499/UID/04029/2025), UID/PRR/04029/2025 (DOI: 10.54499/UID/PRR/04029/2025) and UID/PRR2/04029/2025 (DOI: 10.54499/UID/PRR2/04029/2025), and under the Associate Laboratory Advanced Production and Intelligent Systems ARISE under reference LA/P/0112/2020 (DOI: 10.54499/LA/P/0112/2020).

The student would also like to acknowledge the contributions of both their supervisors, Professor Doctor José Sena Cruz and Doctor Luís Correia; as well as PhD student Hévar Hámid, who was integral to the development of the work.

STATEMENT OF INTEGRITY

I hereby declare having conducted this academic work with integrity. I confirm that I have not used plagiarism or any form of undue use of information or falsification of results along the process leading to its elaboration.

I further declare that I have fully acknowledged the Code of Ethics and Conduct of the University of Minho.

DECLARATION ON THE USE OF ARTIFICIAL INTELLIGENCE (AI) TOOLS

I hereby declare having acted on this academic work with integrity and confirm that I have not resorted to any form of undue use of AI tools, nor to the falsification or omission of information, sources, data, results or processes in any of the stages leading to its elaboration.

I further declare that any use of AI tools was done in a transparent and responsible manner, being duly noted in the work, and that I critically verified the accuracy of the content produced with their support, assuming full responsibility for what I submit.

I further declare that I have fully acknowledged the Code of Ethics and Conduct of the University of Minho, as well as the applicable standards of academic integrity and data protection.

Avaliação de Configurações de Juntas de Camadas na Produção de Laminados Compósitos Derivados de Resíduos de Pás de Aerogeradores

RESUMO

A crescente utilização de materiais compósitos nas pás das turbinas eólicas tem gerado uma quantidade cada vez maior de resíduos de compósitos de fibra de vidro durante o fabrico. Parte destes resíduos consiste em material virgem descartado que ainda preserva as suas propriedades mecânicas originais e poderá ser utilizado noutras aplicações. Assim sendo, a sua reutilização representa uma oportunidade para reduzir o desperdício de materiais e melhorar a sustentabilidade da produção de compósitos.

Esta dissertação investiga a otimização de configurações de juntas feitas a partir de tecidos de fibra de vidro descartado de pás de turbinas eólicas. Para o efeito, são considerados dois tipos principais, nomeadamente, (i) topo a topo e (ii) com sobreposição, de modo a compreender-se como a disposição das camadas, a geometria da junta e a estratégia de união influenciam a distribuição de tensões, o início de dano e o comportamento à rotura sob estados de tensão de tração.

As simulações numéricas são realizadas através do software Abaqus/CAE para avaliar a resposta mecânica das configurções propostas. Os modelos incorporam o comportamento de dano do compósito e a modelação da zona coesiva, permitindo identificar regiões críticas no laminado e na interface de união. São também realizados ensaios experimentais de tração para obter dados mecânicos reais e fundamentar a validação dos resultados numéricos. Ao combinar a modelação numérica e os ensaios experimentais, este trabalho visa identificar configurações de juntas com melhor desempenho mecânico e promover a reutilização de resíduos de compósitos provinientes da frabicação de pás de turbinas eólicas noutras aplicações estruturais

PALAVRAS-CHAVE: Resíduos de pás de turbinas eólicas; Compósitos de fibra de vidro; Configurações de juntas; Modelação de zona coesiva; Ensaios de tração.

Assessment of Ply Joint Configurations in the Production of Composite Laminates Derived from Wind Turbine Blade Waste

ABSTRACT

The increasing use of composite materials in wind turbine blades has led to a growing amount of glass fibre composite waste generated during manufacturing. Part of this waste consists of discarded virgin material that still retains its original mechanical properties and could be used for other applications. Its reuse therefore represents an opportunity to reduce material waste and improve the sustainability of composite production.

This dissertation investigates the optimisation of joint configurations made from discarded wind turbine blade glass fibre material. The study includes material characterisation of both the composite laminate and the resin or matrix system associated with the cohesive bonding region. Two main joint types are considered, namely, (i) end-to-end and (ii) overlap configurations, to understand how ply arrangement, joint geometry, and bonding strategy affect stress distribution, damage initiation, and failure behaviour under tensile loading

Numerical simulations are carried out using Abaqus/CAE to evaluate the mechanical response of the proposed configurations. The models include composite damage behaviour and cohesive zone modelling, allowing the identification of critical regions within the laminate and bonded interface. Experimental tensile tests are also performed to obtain real mechanical data and support the validation of the numerical results. By combining numerical modelling and experimental testing, this work aims to identify joint configurations with improved mechanical performance and to support the reuse of wind turbine blade composite waste in other structural applications.

KEYWORDS: Wind turbine blade waste; Glass fibre composites; Joint configurations; Cohesive zone modelling; Tensile testing.

TABLE OF CONTENTS

Acknowledgements iii
Resumo V
Abstract VI
List of Figures IX
List of Tables XIV
List of Abbreviations and Symbols XVI
1. Introduction 1
1.1. Motivation 1
1.1.1. CirWind project 1
1.2. Objectives 2
1.3. Organisation and structure of the dissertation 4
2. Literature Review 7
2.1. Waste in the wind energy generation industry 7
2.1.1. General waste streams in wind energy production 7
2.1.2. Manufacturing waste from wind turbine blades 8
2.1.3. Environmental and technical challenges of composite materials 8
2.1.4. Reuse of glass fibre offcuts and manufacturing waste 9
2.1.5. Relevance to the CirWind and the dissertation scope 10
2.2. Ply joint configurations for composites manufacturing 11
2.2.1. Need for joining in composite structures 11
2.2.2. End-to-end ply joints 12
2.2.3. Relationship between joint configuration and numerical modelling 20
2.3. Numerical modelling of composites with discontinuities 21
2.3.1. Abaqus CAE software and modelling 21
2.3.2. Cohesive zone modelling 22
2.4. Final Remarks 25
3. Numerical modelling 27
3.1. Modelling strategy 27

3.1.1. Abaqus CAE dynamic/explicit simulation mode 27
3.1.2. Cohesive element usage and definition 28
3.2. Modelling process 28
3.2.1. Component definition 28
3.2.2. Material property definition 35
3.2.3. Assembly and part interaction definition 41
3.2.4. Step definition 42
3.2.5. Boundary conditions 43
3.2.6. Mesh 44
3.3. Design of ply end-to-end ply joint configurations 52
3.3.1. Critical parameter study of ply end-to-end joints 52
3.3.2. Possible complex configurations 53
3.4. Numerical simulation results 54
3.4.1. Study of end-to-end joint configuration critical parameters 56
3.4.2. Complex end-to-end ply joints numerical results 74
4. Experimental characterisation of glass fibre/epoxy composite laminates 79
4.1. Specimen manufacturing process 79
4.1.1. Materials used for the production of the composite material laminates 79
4.1.2. Manufacturing process 81
4.1.3. Tensile testing data acquisition 94
4.2. Experimental results and discussion 100
4.2.1. Aligned ply joint configurations 100
4.2.2. Stepped ply joint configuration 106
5. Conclusion and future work 111
5.1. Overall conclusions 111
5.2. Future works 112
6. References 115

LIST OF FIGURES

Figure 2.1: Example of an end-to-end ply joint [19] 12
Figure 2.2: Resin-rich pocket size [19] 13
Figure 2.3: Distance between resin-rich pockets [19] 14
Figure 2.4: Finger-type end-to-end ply joint example [19] 16
Figure 2.5: Asymmetric scarf-type end-to-end ply joint example [19] 17
Figure 2.6: Symmetric scarf-type end-to-end ply joint example [19] 17
Figure 2.7: Asymmetric Interleafed scarf-type end-to-end ply join example [19] 18
Figure 2.8: Symmetric interleafed scarf-type end-to-end ply joint example [19] 19
Figure 2.9: Bilinear cohesive law material behaviour graph [39] 25
Figure 3.1: Example of biaxial 0°/90° stitched glass fibre mat [45] 29
Figure 3.2: Individual fibre direction shell element modelling strategy 1 (upper half) and bidirectional glass fibre mat shell element modelling strategy 2 (lower half) 29
Figure 3.3: Individual fibre direction modelling strategy shell element disposition before the simulated failure point of the laminate 30
Figure 3.4: Individual fibre direction modelling strategy shell element disposition after the simulated failure point of the laminate 31
Figure 3.5: ISO 527-4:2023 geometrical restrictions for tensile tests for fibre-reinforced plastic composites [47] 32
Figure 3.6: Overall dimensions for the length and width for the laminate and fibre directions 32
Figure 3.7: Section definition of the composite shell element to define the different fibre direction regions 33
Figure 3.8: Representation of upper, lower and cohesive layers in relation to the symmetry plane in a 4-composite-mat layered laminate 34
Figure 3.9: Representation of fibre orientation regions within the upper and lower composite shell elements in a 4 composite mat layered laminate 34
Figure 3.10: Boundary conditions defined 44
Figure 3.11: Composite continuum shell element rectangular prism face selection for assigning a correct staking direction in the “mesh” module of the Abaqus CAE numerical simulation software 45
Figure 3.12: Laminate geometry for the numerical simulation of the mesh element size sensitivity analysis 46

Figure 3.13: Manually calculated load-displacement curve for a continuous 4-layer composite laminate 48
Figure 3.14: Load-displacement curve of the mesh sensitivity study 49
Figure 3.15: Example of meshing strategy for a simulated test ply-joint laminate 51
Figure 3.16: Ply joint discontinuity disposition utilised for performing the end-to-end ply joint critical parameter study 52
Figure 3.17: Ply joint discontinuity disposition where the voids have been placed aligned on top of each other 53
Figure 3.18: Asymmetric interleafed misaligned scarf ply configuration 53
Figure 3.19: Symmetric interleafed aligned scarf ply joint configuration 54
Figure 3.20: Symmetric interleafed misaligned scarf ply joint configuration 54
Figure 3.21: "Gap" and "Pocket" measurements on the ply joint discontinuity disposition utilised for performing the end-to-end ply joint critical parameter study 56
Figure 3.22: Nomenclature used for the gap and pocket lengths and thickness of a single layer of glass fibre mat 56
Figure 3.23: Load-displacement curve of the effect of pocket size variation study 57
Figure 3.24: Engineering stress-strain curve of the effect of pocket size variation study 58
Figure 3.25: Evolution of the stress ratios vs. the resin pocket aspect ratio in all three numerical simulations performed for the effect of pocket size study 61
Figure 3.26: Location of the middle cohesive element 62
Figure 3.27: QUADSCRT-Displacement curves for the three numerical simulations performed for the effect of pocket size study 63
Figure 3.28: SDEG-Displacement curves for the three numerical simulations performed for the effect of pocket size study 63
Figure 3.29: Post-failure Hashin fibre tensile damage initiation criterion (HSNFTCRT) analysis of the 0° fibre orientated regions of a numerically simulated laminate for the effect of pocket size study 64
Figure 3.30: Load-displacement curve of the effect of the length between resin pockets variation study 65
Figure 3.31: Engineering stress-strain curve of the effect of the length between resin pockets variation study 66
Figure 3.32: Location of the critical cohesive regions in the aligned ply joint variant (longitudinal direction) 67

Figure 3.33: Evolution of the stress ratios vs. the normalised step length in all five numerical simulations for the effect of the length between resin pockets variation study 69
Figure 3.34: QUADSCRT-Displacement curves for the three numerical simulations performed for the effect of the length between resin pockets variation study 70
Figure 3.35: SDEG-Displacement curves for the three numerical simulations performed for the effect of the length between resin pockets variation study 71
Figure 3.36: SDEG values for all cohesive element edges close to the resin pockets right before complete laminate failure for the numerically simulated normalised step length equal to 10 variant (composite shell elements removed) 72
Figure 3.37: QUADSCRT-Displacement curve obtained from the numerical simulation of the aligned ply joint variant 73
Figure 3.38: SDEG-Displacement curve obtained from the numerical simulation of the aligned ply joint variant 73
Figure 3.39: SDEG values for all cohesive element edges close to the resin pocket right before complete laminate failure for the numerically simulated “aligned” variant (composite shell elements removed) . 74
Figure 3.40: Load-displacement curves of all three numerically simulated complex end-to-end ply joint configurations 75
Figure 3.41: Engineering stress-strain curves of all three numerically simulated complex end-to-end ply join configurations 75
Figure 4.1: Composition data of G-0/1/0/1-1264 waste bi-axial glass fibre mats [48] 79
Figure 4.2: G-0/1/0/1-1264 waste bi-axial glass fibre mat used in the test laminate manufacturing process 80
Figure 4.3: Alignment and measurement of the glass fibre mat sections desired for cutting 82
Figure 4.4: Manual cutting of the waste glass fibre mats 82
Figure 4.5: Weight measurement for the mixing of the matrix 83
Figure 4.6: Careful stirring of the mixed matrix 84
Figure 4.7: Preparation of the flat working surface 84
Figure 4.8: First two layers of glass fibre mat, with a fibre discontinuity having been applied to one of them 85
Figure 4.9: LUNA™ optic fibre used to measure strain 85
Figure 4.10: Position securing method used for the optic fibre LUNA™ strain sensors 86
Figure 4.11: Peel ply and infusion mesh positioning 87

Figure 4.12: Positioning of tube supports and spiral feed tube positioning..... 87
Figure 4.13: Resin flow front during the infusion process..... 88
Figure 4.14: Vacuum bag application and sealing process..... 88
Figure 4.15: Full vacuum infusion system..... 89
Figure 4.16: Aligned 3mm length resin pocket ply joint configuration..... 90
Figure 4.17: Measurement of resin-rich pocket length..... 90
Figure 4.18: Fibre sagging experienced in the aligned 3mm resin pocket length ply joint configuration laminate..... 90
Figure 4.19: Aligned 0mm length resin pocket ply joint configuration..... 91
Figure 4.20: Stepped 10mm gap 0mm length resin pocket ply joint configuration..... 91
Figure 4.21: Composite laminate after the CNC cutting process..... 92
Figure 4.22: Hand-cut final separation of the various specimens from the parent ply joint configuration laminate..... 92
Figure 4.23: Example of excessive cutting speed leading to the burning of the matrix resin..... 93
Figure 4.24: Specimen during end tab adhesive curing process..... 94
Figure 4.25: Example of contrasting paint applied to a specimen..... 95
Figure 4.26: Virtual extensometer ends placement on top of painted spots before the tensile testing.. 95
Figure 4.27: Video extensometer calibration process..... 96
Figure 4.28: Width and thickness numbered measurement points of the laminate coupons for all ply join configurations produced, marked with red lines..... 97
Figure 4.29: Video extensometer output signals average calculation..... 99
Figure 4.30: Experimental and simulated load-displacement curves for the aligned 3mm resin pocket length laminate..... 101
Figure 4.31: Experimental and simulated load-displacement curves for the aligned 0mm resin pocket length laminate..... 101
Figure 4.32: Experimental and simulated stress-strain curves for the aligned 3mm resin pocket length laminate..... 103
Figure 4.33: Experimental and simulated stress-strain curves for the aligned 0mm resin pocket length laminate..... 103
Figure 4.34: Delamination failure between inner discontinuous layers and outer continuous layers... 105
Figure 4.35: Tensile failure of an outer continuous layer..... 105

Figure 4.36: Delamination areas experienced in the numerically simulated aligned 3mm pocket length ply joint configuration..... 105
Figure 4.37: Composite material failure at the end tab gripping area 106
Figure 4.38: Experimental and simulated load-displacement curves for the stepped 0mm resin pocket length, 10mm gap between resin pockets laminate 107
Figure 4.39: Experimental and simulated stress-strain curves for the stepped 0mm resin pocket length, 10mm gap between resin pockets laminate 108
Figure 4.40: Delamination mechanisms experienced in all valid specimens of the BD4-P0-o10 ply joint configuration laminate coupons 109
Figure 4.41: Delamination areas experienced in the numerically simulated stepped 10mm pocket gap length, 3mm pocket length ply joint configuration..... 109

LIST OF TABLES

Table 2.1: Advantages and disadvantages of the three main types of end-to-end ply joint configurations and their variants 19
Table 3.1: Individual material properties for the fibre reinforcement and matrix of the composite laminate used in the numerical simulations [54, 55] 36
Table 3.2: Combined composite shell element elastic properties and density 37
Table 3.3: Hashin damage composite material property values 38
Table 3.4: Hashin damage evolution settings selection and composite material property values 39
Table 3.5: Density and elastic behaviour settings selection and cohesive element material property values 39
Table 3.6: QUADS damage settings and cohesive element material properties [65] 40
Table 3.7: QUADS damage evolution settings and cohesive element material properties [66] 40
Table 3.8: Simulation times for each numerical simulation of the mesh sensitivity analysis 50
Table 3.9: Performance analysis chart of the effect of pocket size study 58
Table 3.10: Peak stress values recorded in all three numerical simulations performed for the effect of pocket size study 60
Table 3.11: Stress ratios of all three numerical simulations performed for the effect of pocket size study 61
Table 3.12: Performance analysis chart of the effect of the length between resin pockets variation study 67
Table 3.13: Peak stress values recorded in all three numerical simulations performed for the effect of the length between resin pockets variation study 68
Table 3.14: Stress ratios of all three numerical simulations performed for the effect of the length between resin pockets variation study 68
Table 3.15: Performance analysis chart of the three different complex end-to-end ply joint configurations 76
Table 3.16: Percentage of the theoretical maximum load achieved by each of the complex end-to-end ply joint configurations 76
Table 4.1: Test specimen type naming nomenclature 94
Table 4.2: Aligned 3mm length resin pocket laminate average specimen cross-section calculations ... 97
Table 4.3: Aligned 0mm length resin pocket laminate average specimen cross-section calculations ... 98

Table 4.4: Stepped 10mm gap 0mm length resin pocket laminate average specimen cross-section calculations 98

List of Abbreviations and Symbols

Abbreviations

QUADS	Quadratic nominal stress failure criterion
ROM	Rule of mixtures
BK	Benzeggagh-Keane mixed mode behaviour
QUADSCRT	Quadratic nominal stress damage initiation criterion
SDEG	Scalar stiffness degradation
HSNFTCRT	Hashin fibre tensile damage initiation criterion

Symbols

σ_n	Cohesive stress in tension (direction 1)
σ_s	Cohesive stress in shear (direction 2)
σ_t	Cohesive stress in tear (direction 3)
k_{nn}	Stiffness matrix component (direction 1)
k_{ss}	Stiffness matrix component (direction 2)
k_{tt}	Stiffness matrix component (direction 3)
δ_n	Relative displacement between the top and bottom points of the cohesive layer (direction 1)
δ_s	Relative displacement between the top and bottom points of the cohesive layer (direction 2)
δ_t	Relative displacement between the top and bottom points of the cohesive layer (direction 3)
E	Elastic modulus
G	Shear modulus
t_A	Cohesive element/Adhesive thickness
σ_n^0	Maximum value of nominal stress in tension (direction 1)
σ_s^0	Maximum value of nominal stress in shear (direction 2)
σ_t^0	Maximum value of nominal stress in tear (direction 3)
δ_m^0	Effective initial displacement

δ_m^{max}	Effective maximum displacement
δ_m^f	Effective final displacement
E	Elastic modulus
E_f	Fibre reinforcement elastic modulus
E_m	Matrix elastic modulus
E_1	Composite longitudinal elastic modulus
E_2	Composite in-plane transverse elastic modulus
E_3	Composite through-thickness transverse elastic modulus
ν	Poisson's ratio
ν_f	Fibre reinforcement Poisson's ratio
ν_m	Matrix Poisson's ratio
ν_{12}	Composite in-plane longitudinal Poisson's ratio
ν_{13}	Composite longitudinal through-thickness Poisson's ratio
ν_{23}	Composite transverse Poisson's ratio
G	Shear modulus
G_f	Fibre reinforcement shear modulus
G_m	Matrix elastic modulus
G_{12}	Composite in-plane longitudinal shear modulus
G_{13}	Composite longitudinal through-thickness shear modulus
G_{23}	Composite longitudinal through-thickness shear modulus
ρ	Density
ρ_f	Fibre reinforcement density
ρ_m	Matrix density
ρ_c	Composite density
ρ_{coh}	Cohesive element density
V	Volume fraction
V_f	Fibre reinforcement volume fraction
V_m	Matrix volume fraction
P_f	Fibre reinforcement property
P_m	Matrix property
P_c	Composite property

X_T	Longitudinal tensile strength
X_C	Longitudinal compressive strength
Y_T	Transverse tensile strength
Y_C	Transverse compressive strength
S_L	Longitudinal shear strength
S_T	Transverse shear strength
G_{XT}	Longitudinal tensile fracture energy
G_{XC}	Longitudinal compressive fracture energy
G_{YT}	Transverse tensile fracture energy
G_{YC}	Transverse compressive fracture energy
E/E_{nn} or K_{nn}	Normal/opening stiffness
$G1/E_{ss}$ or K_{ss}	First shear/sliding stiffness
$G2/E_{tt}$ or K_{tt}	Second shear/tearing stiffness
t_n^0	Nominal stress, normal-only mode
t_s^0	Nominal stress, first direction
t_t^0	Nominal stress, second direction
G_{IC}	Normal mode fracture energy
G_{IIC}	Shear mode fracture energy, first direction
G_{IIIC}	Shear mode fracture energy, second direction
$\varepsilon_{f,0°}$	Theoretical strain at the point of failure of the 0° orientated fibre regions
$\varepsilon_{f,90°}$	Theoretical strain at the point of failure of the 90° orientated fibre regions
$\Delta l_{f,0°}$	Elongation at the point of failure of the 0° orientated fibre regions
$\Delta l_{f,90°}$	Elongation at the point of failure of the 90° orientated fibre regions
$l_{0,laminate}$	Initial length of the laminate
$F_{f,0°}$	Theoretical load experienced at the point of failure of the 0° orientated fibre regions
$F_{f,90°}$	Theoretical load experienced at the point of failure of the 90° orientated fibre regions
$F_{max,config.,sim}$	Maximum load experienced by a ply joint configuration during a simulation
$F_{max,theoretical}$	Theoretical maximum load that a laminate can withstand
$w_{1\ ply,0°}$	Width of 1 ply of 0° fibre orientated composite material
$w_{1\ ply,90°}$	Width of 1 ply of 90° fibre orientated composite material
$w_{1\ ply}$	Width of 1 layer of glass fibre mat

$w_{1\ coh.\ layer}$	Width of 1 cohesive layer
$t_{1\ ply,0°}$	Thickness of 1 ply of 0° fibre orientated composite material
$t_{1\ ply,90°}$	Thickness of 1 ply of 90° fibre orientated composite material
$t_{1\ ply}$	Thickness of 1 layer of glass fibre mat
$t_{1\ coh.\ layer}$	Thickness of 1 cohesive layer
n_{plies}	Number of plies of composite material
XY_T	Combined fibre orientation region tensile strength
σ_{eng}	Engineering stress
RF_1	Longitudinal reaction force
$A_{0,coss-section,total}$	Original initial cross-sectional area of the whole laminate
ε_{eng}	Engineering strain
U_1	Longitudinal displacement
$l_{0,total}$	Total initial length of the laminate
l_{gap}	Length of the gap between resin-rich pockets
l_{pocket}	Length of the resin pocket
$l_{pocket}/t_{1\ ply}$	Resin pocket aspect ratio in relation to the glass fibre mat layer thickness
$\sigma_{11}^{peak}/\sigma_{eng}$	Peak longitudinal stress to engineering stress ratio
$\tau_{13}^{peak}/\sigma_{eng}$	First peak interlaminar shear stress to engineering stress ratio
$\tau_{23}^{peak}/\sigma_{eng}$	Second peak interlaminar shear stress to engineering stress ratio
$\sigma_{33}^{peak}/\sigma_{eng}$	Peak normal opening/peel stress -engineering stress ratio
σ_{11}	Longitudinal stress
τ_{13}	First interlaminar shear stress
τ_{23}	Second interlaminar shear stress
σ_{33}	Normal opening/peel stress
ΔL	Measured specimen displacement
$\varepsilon_{videoextensometer,avg}$	Average strain measured from both extensometers
L_0	Measured initial specimen length
$F_{measured}$	Measured load applied to the specimen
$A_{cross-section,avg}$	Average measured cross-sectional area of the specimen
$l_{gap}/t_{1\ ply}$	Normalized step length in relation to the glass fibre mat layer thickness

THIS PAGE WAS INTENTIONALLY LEFT BLANK

1. INTRODUCTION

1.1. Motivation

Nowadays, increasingly, the reduction of waste and pollution is a very important issue that needs to be tackled. The composite material industry has always been a great producer of waste, due to a combination of the inability to recycle selected materials and the economic impossibility of taking the steps necessary to ensure waste and pollution minimisation. Current waste management routes for composite materials include landfill, incineration, co-processing, mechanical recycling, chemical recycling, and reuse [1, 2]. However, many of these options either reduce the value of the original material or require additional processing.

The wind energy generation industry has always been one of the biggest contributors to this environmental problem, due to the large and widespread use of composite materials, especially with the use of wind turbine blades, being almost entirely made of such materials. However, the production of such components results in a large amount of discarded virgin glass fibre material cut-outs, resulting from the shaping process of the different layers of glass fibre mats that form the blades [3].

The scope of this dissertation is the evaluation of possible joint configurations made from discarded virgin glass fibre laminate material. The study is limited to two principal joining concepts: end-to-end configurations and overlap configurations. These configurations are selected because they represent practical methods for connecting smaller laminate sections to produce larger composite elements. The intended application of these joined pieces is not primarily structural or safety-critical use, but rather secondary, lightly loaded, or non-critical components.

1.1.1. CirWind project

The work developed in the context of this dissertation was carried out based on the ongoing work in the CirWind project, which is focused on the development of innovative and sustainable urban furniture and equipment manufactured from composite materials obtained from waste generated during the production of wind turbine blades. Its main purpose is to promote circularity by giving a new use to materials that would otherwise be discarded, while also supporting sustainability and the integration of renewable energy

concepts within communities. In this context, CirWind connects the wind energy sector with urban design by transforming composite manufacturing waste into practical products for public spaces.

The project has a multidisciplinary character, bringing together knowledge from civil and composites engineering, environmental engineering, architecture, and product design. This combination of disciplines is important because the proposed solutions must not only present adequate mechanical performance, but also meet environmental, functional, and design requirements. The products considered within the project include different types of urban furniture, such as benches and bins, as well as urban equipment, such as road signs and manhole covers. These applications may require different structural concepts, including sandwich structures, shell elements, thin plates, and thick plates.

A key innovation of CirWind is the use of waste produced by the wind energy industry as a resource for new composite products. The project also explores innovative design solutions, nature-based approaches, and optimised configurations from the perspective of cost, material consumption, and sustainability. In addition, it includes the investigation of thermoplastic resins and the possible incorporation of waste powder into the material system. The mechanical and durability response of the developed solutions is also assessed to ensure that the final products can perform adequately in their intended applications.

Overall, CirWind aims to demonstrate that waste from wind turbine blade manufacturing can be redirected into useful urban products instead of being discarded. Through recyclability assessment, life cycle analysis, pilot projects, and stakeholder engagement, the project supports the development of circular strategies for composite materials and contributes to more sustainable urban infrastructure.

The work developed in this MSc Dissertation contributes to increasing the knowledge about the performance of adhesive joint configurations between composite material elements that will be used in the creation of larger elements to repurpose the wind turbine blade discarded material.

1.2. Objectives

The main objective of this MSs Dissertation is to evaluate the mechanical feasibility of reusing discarded virgin glass fibre composite material generated during wind turbine blade manufacturing. This work is developed in the context of the CirWind project, which aims to transform composite waste from the wind energy sector into useful urban furniture and equipment. Therefore, the purpose of this dissertation is not only to study the mechanical behaviour of reused composite laminate sections, but also to contribute to the broader goal of promoting circularity and material efficiency in composite manufacturing.

A first objective of the work is to characterise the relevant material properties required for the mechanical analysis of the proposed joints. Particular attention is given to the matrix or resin material used in the bonded region, since its behaviour strongly influences the load transfer between joined laminate sections. The characterisation of these properties is necessary to define the cohesive material model used in the numerical simulations and to represent the initiation and evolution of damage in the adhesive interface. This stage provides the material input data required to obtain more realistic numerical predictions.

Another important objective is to investigate different joint configurations that could allow smaller discarded laminate sections to be assembled into larger composite components. The study focuses on two main types of configurations: (i) end-to-end joints and (ii) overlap joints. The end-to-end configuration represents a simple joining strategy, while the overlap configuration provides a larger bonded area and may improve the transfer of tensile loads between laminate sections. By comparing these configurations, the dissertation aims to identify which geometrical and ply arrangement strategies offer better mechanical performance.

The numerical part of the dissertation is carried out using Abaqus/CAE. The proposed joint configurations are modelled under tensile loading conditions to evaluate stress distribution, damage initiation, and failure behaviour. Composite damage modelling is used to represent failure within the laminate plies, while cohesive zone modelling is used to simulate the behaviour of the bonded interface. These simulations allow critical regions of the joint to be identified and provide a basis for comparing the expected performance of the different configurations before experimental testing.

Experimental tensile tests are also performed to obtain real-world mechanical results. These tests provide information about the load-bearing capacity, deformation behaviour, and failure modes of the different joint configurations. The experimental results are then compared with the numerical predictions to assess the accuracy of the Abaqus models and to improve confidence in the simulation approach. This validation step is essential because it connects the numerical analysis with the actual mechanical response of the manufactured specimens.

Ultimately, the objective of this dissertation is to support the CirWind project by providing technical knowledge on how discarded virgin glass fibre laminate material can be joined and reused effectively. By identifying promising joint configurations and evaluating their mechanical behaviour through both simulation and testing, this work contributes to the development of sustainable composite solutions for non-critical urban applications, such as furniture and equipment, and to identify experimental and numerical protocols to test, model and analyse composite solutions made from the wind energy sector waste.

1.3. Organisation and structure of the dissertation

This dissertation is organised in a sequence that follows the development of the research work, starting from the general motivation and literature background, continuing with the numerical and experimental methodologies, and finishing with the discussion of the results, conclusions and future work.

Chapter 1 introduces the motivation of the dissertation and presents the relevance of reusing discarded virgin glass fibre material generated during wind turbine blade manufacturing. This chapter also introduces the CirWind project, defines the main objectives of the work, and explains the general scope of the study, which focuses on the evaluation of composite joint configurations for secondary and non-critical applications.

Chapter 2 presents the literature review. This chapter first discusses waste generation in the wind energy sector, with particular attention to manufacturing waste and glass fibre offcuts. It then introduces the need for ply joint configurations in composite manufacturing, focusing especially on end-to-end ply joints, resin-rich pockets, ply discontinuities, spacing between terminations and through-thickness alignment. Finally, the chapter reviews the numerical modelling of composite laminates with discontinuities, including Abaqus/CAE modelling and cohesive zone modelling.

Chapter 3 describes the numerical modelling work performed in Abaqus/CAE. This chapter explains the modelling strategy, the use of Dynamic/Explicit simulations, the definition of composite shell elements and cohesive elements, the material properties, interactions, boundary conditions, step definition and meshing strategy. It also presents the numerical study of end-to-end ply-joint configurations, including the influence of resin pocket size, distance between resin pockets, aligned discontinuities and more complex interleaved scarf-type configurations.

Chapter 4 presents the experimental programme developed to obtain real mechanical data from manufactured glass fibre/epoxy laminates. This includes the preparation of the reused glass fibre mats, the selection and mixing of the matrix resin, the vacuum infusion manufacturing process, the cutting of tensile specimens and the test setup. The experimental results are then used to evaluate the real tensile response of the manufactured specimens and to compare their behaviour with the numerical predictions.

The final **Chapter 5** presents the main conclusions obtained from the work carried out. It summarises the influence of the joint geometry on tensile performance, highlights the importance of resin pocket spacing and through-thickness alignment, and discusses the differences observed between the Abaqus simulations and the experimental results. This chapter also presents the recommended future work, including further material characterisation, calibration of the cohesive and damage models, microscopic

inspection of the resin-rich regions and a larger experimental campaign to improve the reliability of the proposed modelling approach.

THIS PAGE WAS INTENTIONALLY LEFT BLANK

2. LITERATURE REVIEW

2.1. Waste in the wind energy generation industry

2.1.1. General waste streams in wind energy production

Wind energy is widely considered a key renewable energy technology, but the industry still generates material waste during manufacturing, operation, maintenance, and end-of-life decommissioning [3, 5]. A wind turbine is composed of several major material groups, including steel, copper, concrete, polymers, coatings, adhesives, and fibre-reinforced composite materials [6, 7]. Many metallic components can be recycled through established routes, but wind turbine blades are more challenging because they are commonly manufactured from thermoset fibre-reinforced polymer composites. These composites are designed to be durable, lightweight, fatigue-resistant, and difficult to degrade during service, but the same characteristics make them difficult to recycle at the end of their useful life [5, 7].

The waste generated by the wind energy sector can be divided into three broad categories: manufacturing waste, operation and maintenance waste, and end-of-life waste [3, 5]. Manufacturing waste is produced during the production of blades and other components; operation and maintenance waste is generated during repair, replacement, surface treatment, or blade upgrading; and end-of-life waste corresponds to decommissioned blades and other turbine components after the turbine has reached the end of its service life [3, 5].

Most public discussion focuses on end-of-life blade waste because large numbers of blades are expected to be decommissioned in the coming decades [3, 5]. However, manufacturing waste is also important because it is generated continuously during blade production and includes dry fibre off-cuts, composite off-cuts, resin residue and vacuum consumables [3]. In the case of the present dissertation, discarded virgin glass fibre material generated during manufacturing is the relevant material to be taken into account; more specifically, the offcuts of excess glass fibre mats that otherwise would be discarded.

2.1.2. Manufacturing waste from wind turbine blades

Wind turbine blades are commonly manufactured using large moulds and layered fibre architectures [7, 8]. Glass fibre mats, fabrics, core materials, resin systems, peel plies, flow media, vacuum bags, and auxiliary consumables are arranged to form the blade shell, spar caps, shear webs, and root regions [7, 8, 9]. During this process, glass fibre mats must be cut and shaped to match the geometry of the blade. Since blades have curved and tapered geometries, not all supplied fibre material can be used directly in the final lay-up. Cutting and trimming operations generate dry fibre offcuts and other pieces of virgin pristine material [3, 5, 9]. These offcuts may have the same material quality as the reinforcement used in the blade, but they are often too small or irregular to be used in the original production process.

As mentioned before, the literature specifically recognises this type of waste as consisting mainly of dry fibre offcuts, composite offcuts, resin residue, and vacuum consumables [3, 5]. The focus on glass fibre cut-outs from the shaping of virgin fibre mats is particularly relevant because glass fibre is the dominant reinforcement in many wind turbine blades [3, 7]. These dry cut-outs may still be clean, unaged, and mechanically valuable; in contrast with the other types of manufacturing wastes, which may end up damaged, contaminated or bonded at the point of discarding. If they are discarded directly, the material value embedded in fibre production, transport, handling, and preparation is lost [2]. In some cases, manufacturing waste may also include partially cured or cured composite offcuts, trimming dust, resin-rich waste, and consumables contaminated with resin [2, 3, 5]. However, the best reuse strategy depends strongly on the exact form of the waste. Dry fabric cut-outs can potentially be reintroduced into composite manufacturing, while cured composite offcuts may be more suitable for mechanical reuse, secondary components, fillers, or recycling routes [2, 10].

2.1.3. Environmental and technical challenges of composite materials

Fibre-reinforced polymer composite waste is difficult to manage because the fibres and polymer matrix are strongly bonded. In thermoset composites, the crosslinked matrix cannot simply be melted and reshaped like thermoplastic materials [2, 11, 12]. There are main ways of recycling fibre-reinforced polymer waste: mechanical, thermal and chemical recycling.

Mechanical recycling can reduce the material to particles or fibres, but often lowers the value of the original reinforcement [11, 12, 13]; thermal recycling and pyrolysis may recover fibres but can degrade fibre properties, require energy input, and generate emissions or secondary products that must be managed [2, 11, 13]; while chemical recycling can be more selective but may require solvents, catalysts,

pressure, or temperature conditions that are not always economically attractive [2, 11]. Reviews of FRP recycling show that multiple methods exist, but each has limitations related to cost, scalability, fibre quality, environmental performance, and market demand for recycled products [2, 11, 12].

The environmental issue is not only the physical accumulation of waste, but also the loss of embodied energy and resources. Glass fibres and resin systems require raw materials and energy to produce [13]. When virgin offcuts are discarded before ever being used in a final product, the environmental burden of producing that material has already occurred, but no useful service life is obtained. From a circular economy perspective, this is inefficient. Direct reuse of clean virgin offcuts can therefore be preferable to destructive recycling because it maintains more of the original material structure and value [1, 14]. This is one of the main motivations behind this dissertation and the CirWind R&D project.

Landfills are increasingly seen as undesirable for composite blade waste because it does not recover material value and do not align with circular economy objectives [1, 13]. Incineration may recover some energy but can destroy the fibre reinforcement and produce residues [1, 13]. Co-processing in cement kilns can use composite waste as fuel and mineral input, but it is still a recovery route rather than a high-value reuse route [1, 13]. Reviews of wind turbine blade end-of-life management emphasise that reuse, recycling, and recovery strategies are needed to reduce reliance on landfill and improve the sustainability of the wind energy sector [1, 3, 5]. Although these studies often focus on end-of-life blades, the same logic applies to manufacturing waste: a waste hierarchy should prioritise prevention, reuse, and high-value recovery before disposal [1, 3].

2.1.4. Reuse of glass fibre offcuts and manufacturing waste

Novais et al. [15] studied the incorporation of glass fibre fabric waste into geopolymer matrices and explicitly described the material as glass fibre fabric offcuts from wind turbine blade production. Their work used non-woven glass fibre mat waste produced during blade manufacture to reinforce inorganic polymer composites. This is an important reference for the present dissertation because it demonstrates that glass fibre offcuts from blade production can be treated as a useful material resource rather than only as waste [15].

However, the approach in the present dissertation is different. Instead of incorporating cut fibres or fabric pieces into another matrix as reinforcement, the aim is to preserve the laminate or ply-based nature of the composite material and join glass fibre mat sections into larger pieces. This represents a higher-level reuse concept because the existing fibre architecture and laminate form are maintained as much as

possible. The material is not reduced to filler, powder, or short fibres. Instead, the research investigates whether joined configurations can provide sufficient mechanical performance for non-critical or lightly loaded applications associated with urban furniture and equipment [13, 14].

This approach is consistent with the logic of circular material use. When a material remains clean and structurally meaningful, direct reuse should be considered before lower-value recycling [11, 14]. For manufacturing offcuts, the challenge is that the pieces may have limited dimensions and may not individually match the shape required for a new product. Joining is therefore essential. By developing end-to-end glass fibre mat joint configurations, smaller pieces can potentially be combined into larger panels, plates, or components. This makes the mechanical performance of the joint the central technical question, since the efficiency of bonded composite joints is strongly influenced by the joint geometry, overlap configuration, and stress distribution in the bonded region [4].

2.1.5. Relevance to the CirWind and the dissertation scope

The R&D Project "CirWind - Development of Innovative sustainable urban furniture and equipment in composites from waste produced by the wind energy Industry for circularity", reference 15232, operation code COMPETE2030-FEDER-00889600, cofounded by Innovation and Digital Transformation Program (COMPETE 2030), by the Portugal 2030 and by the European Union, in Its FEDER component, aims to transform composite waste from the wind energy sector into sustainable urban furniture and equipment. In this context, manufacturing waste from wind turbine blade production is particularly attractive because it can be available before the material has been exposed to service conditions [3, 5]. Virgin glass fibre cut-outs from the shaping of fibre mats may therefore offer a cleaner and more predictable material stream than end-of-life blade fragments. This distinction is relevant because end-of-life blade material may have been affected by fatigue, moisture, environmental exposure, impact damage, repairs, or other service-related degradation [7, 16, 17, 18]. This does not remove the need for characterisation, because manufacturing, storage, cutting, and handling can still introduce variability. However, it supports the idea that these materials may be suitable for secondary applications if their mechanical performance can be demonstrated [15].

The potential applications considered by CirWind, such as benches, bins, road signs and manhole covers, being composed of thin and thick composite plates, shell elements or sandwich structures, mean that they do not necessarily require the same qualification level or mechanical resistance as primary structural components that may be required in larger, higher-stressed structures. Nevertheless, they still require

adequate stiffness, strength, durability, and reliability for their intended use. This creates an appropriate space for reuse strategies, as the intended end products of this project need to perform satisfactorily in urban products where sustainability, cost, and material efficiency are also major design criteria [13, 14]. The dissertation contributes to this objective by focusing on the mechanical evaluation of joined glass fibre ply configurations into larger composite structures. By testing and simulating end-to-end joints, the work addresses one of the practical barriers to direct reuse: how to convert smaller discarded pieces into larger usable components. The waste problem is therefore not treated only as an environmental issue, but as a materials engineering problem. The question is how to preserve value, design reliable joints, and provide evidence that the reused material can serve a practical function. For this reason, the mechanical behaviour of the joint becomes a key design factor, since bonded composite joints are strongly influenced by the geometry, stress distribution, and the behaviour of the adhesive or cohesive region [4].

2.2. Ply joint configurations for composites manufacturing

2.2.1. Need for joining in composite structures

In the present dissertation, ply joints are required because the available material is not a continuous roll or a newly designed laminate, but discarded virgin glass fibre material generated during wind turbine blade manufacturing. These offcuts can retain useful material quality, but their dimensions and shape may not be suitable for direct use in larger urban furniture or equipment components. A jointing strategy is therefore needed to transform smaller pieces into larger plates, panels or shell-type elements without reducing the material to filler or short fibres.

A ply joint can be understood as a joint created at the level of the individual laminate plies rather than only at the level of the complete laminate. Ahamed [19]defines ply joints as co-cured joints produced by forming butt-splices or overlaps between individual plies while controlling the position and spatial distribution of the ply terminations; the main mechanical challenge of these ply joints is that fibres cannot carry load across a pure end-to-end discontinuity unless load is transferred through the surrounding matrix and neighbouring continuous plies. At every ply termination, a local discontinuity is formed. Since the stiffness and strength of the polymer matrix are much lower than those of the fibres, the resin-rich region disturbs the stress field and can become a preferential location for damage initiation [19, 20].

2.2.2. End-to-end ply joints

Since the joining strategy of plies is very important in determining the overall behaviour of the end component, end-to-end ply joints are attractive in this context because they can preserve a large part of the original ply architecture while avoiding the local thickness increase; as these types of joints position the end of one ply directly opposite and at the same level as the ply that Is being connected to, as it can be seen in Figure 2.1. During resin infusion and cure, the polymer matrix bonds the plies and fills the small region between opposing ply ends, producing a local resin-rich pocket, as represented in the figure below in blue.

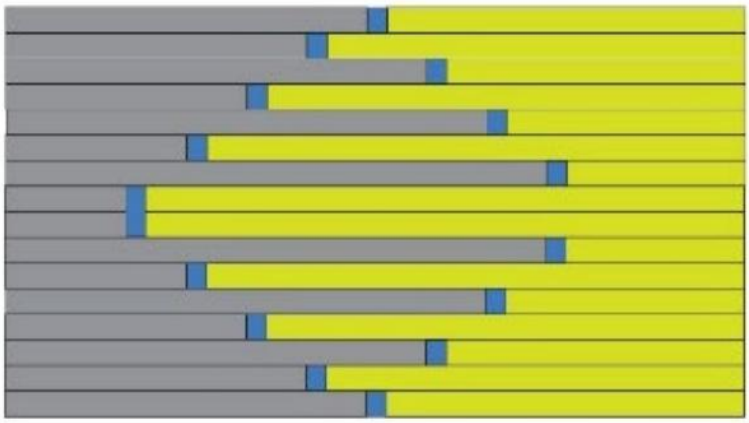


Figure 2.1: Example of an end-to-end ply joint [19]

The practical benefit of this approach is that it can produce a nearly flush laminate. This is important for urban products such as thin plates, shell elements, sandwich skins, benches or cover panels, where excessive local thickness can complicate moulding, joining to other elements, finishing and dimensional control. A flush end-to-end joint also avoids the bending eccentricity associated with external overlaps [19]. For reused material, this is particularly relevant because the objective is not to make the strongest possible primary structural joint, but to obtain a repeatable configuration that can provide sufficient tensile stiffness and strength for secondary or non-critical components.

Critical design parameters in end-to-end ply joints

Due to all the particularities of these types of ply joints, they must be designed so that load transfer is distributed over several ply terminations instead of concentrated at a single through-thickness line. This

makes the spatial distribution of ply ends a central design variable rather than a secondary manufacturing detail.

The literature on tiled laminates and discontinuous laminates confirms the importance of this design philosophy. Baucom et al. [20] showed that changing the spatial arrangement of resin-rich tile-to-tile interfaces strongly influences stress concentrations and strength retention in discontinuous composite laminates. Malkin et al. [21] also demonstrated that ply cuts and ply-cut spacing affect the stress state and failure process in discontinuous laminate designs. These studies provide useful evidence that discontinuities can be engineered rather than treated only as defects. In the present dissertation, the same logic is applied to virgin glass fibre mat offcuts: the discontinuity is unavoidable, but its position, spacing and alignment can be controlled.

Resin-rich pocket size

The resin-rich pocket is the local region of matrix created between opposing ply ends. It is unavoidable in an end-to-end ply joint, but its size and shape must be controlled. In Ahamed's discontinuous laminate study, the resin pocket was treated as a strength-critical feature because its stiffness and strength are lower than those of the reinforcing fibres; consequently, it acts as both a material and geometric discontinuity [19]. The same reasoning applies to glass fibre mats produced by vacuum infusion.

The effect of pocket size is not simply that smaller is always better. A very large resin-rich pocket increases the volume of weak matrix and may reduce local stiffness. However, a very small and sharp pocket can create intense stress concentrations at the opposing corners. Ahamed's finite element study of discontinuous laminates found that reducing the resin pocket length increased the peak longitudinal stress more noticeably than the peak interlaminar shear stress [19]. Malkin et al. [21] also showed that the ply-end geometry associated with resin pockets is important for the damage sequence in discontinuous laminates. For the present dissertation, the relevant design target is therefore a controlled, as much as possible, repeatable pocket geometry, pocket length, thickness and edge shape.

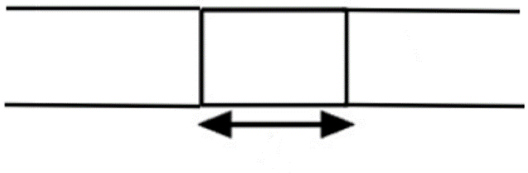


Figure 2.2: Resin-rich pocket size [19]

Distance between resin-rich pockets

The longitudinal distance between resin-rich pockets is commonly described as the step length, joint length or spacing between ply terminations. This distance controls whether the stress fields around neighbouring ply ends interact. If adjacent resin pockets are too close, the ineffective load-transfer zones overlap, and a larger region of the laminate carries less than the intended load. If the distance is large enough, the pockets become approximately elastically isolated and each discontinuity can transfer load without strongly amplifying the next one [19, 20].

Ahamed [19] reports that step length has a strong influence on interlaminar shear stress concentration and on joint strength, going on to study the effect of this length relative to the ply thickness. This methodology provides a useful scaling concept: the spacing between critical terminations should be selected relative to ply thickness and then verified experimentally.

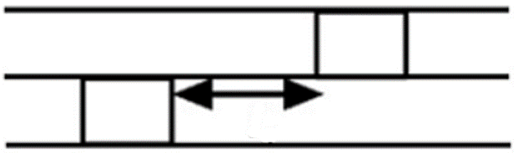


Figure 2.3: Distance between resin-rich pockets [19]

Through-thickness alignment of resin-rich pockets

Through-thickness alignment refers to whether resin-rich pockets from different plies are positioned directly above one another. This is one of the most important design parameters for end-to-end ply joints. If several pockets are stacked through the thickness, the joint contains a nearly continuous resin-rich path. Such a path can promote damage coalescence and rapid delamination because cracks initiated at one ply termination can easily connect with neighbouring terminations. The list of figures in Ahamed's thesis [19] explicitly distinguishes configurations with through-thickness alignment of tile-to-tile interfaces from configurations in which terminations are offset.

Avoiding through-thickness alignment is therefore a central design rule. In practice, this means that the terminations of adjacent plies should be staggered, and critical terminations should be separated by at least one continuous ply whenever possible. This does not remove damage initiation, but it can make damage more progressive and prevent the joint from behaving as a single pre-cracked section. [19, 20]

For the present dissertation, through-thickness alignment should be treated as an experimental variable: one configuration may intentionally align pockets to provide a baseline, while optimized configurations should distribute them.

Ply orientation, symmetry and manufacturability

The configuration of an end-to-end ply joint cannot be defined only by the position of the ply ends. Ply orientation, laminate symmetry, joint length and manufacturing tolerance are also important [19, 20].

For tensile testing, plies aligned with the loading direction are likely to dominate the axial load path. Off-axis plies contribute to shear transfer, transverse stiffness and damage containment, but their discontinuities may not have the same effect as terminations in the main load-bearing direction [19, 22]. This is important for glass fibre mats that combine different fibre orientations within one supplied material layer.

Symmetry is also relevant as unsymmetric termination patterns can create eccentric load paths, resulting in local bending and increased peel stresses [19, 23]. Peel stresses are undesirable because delamination resistance under opening mode is generally lower than under shear-dominated transfer [24].

Lastly, manufacturability also contributes as a limiting factor. The more optimized configurations require precise cutting, identification of each ply, stable placement during lay-up and controlled resin infusion. If these conditions cannot be achieved, a theoretically superior configuration may perform poorly because of misalignment, waviness or excessive resin accumulation [19, 25, 26].

Possible end-to-end ply joint configurations

Out of all the possible end-to-end ply joint configurations that can be designed, three main types of joints can be distinguished as the most important or significant, as there are infinite ways of performing these joints.

Of course, each of the variants that will be displayed can be tweaked in order to include or avoid through-thickness resin-rich pocket alignment.

Staggered/Finger-type end-to-end ply joints

The first main type is the staggered or finger-type joint, where the termination of each ply is shifted by a defined distance relative to adjacent plies. Ahamed identifies finger configurations as one of the main ply-interleaved concepts, and the supplied thesis reports that finger-type layouts can be investigated in both aligned and offset forms [19]. The benefit of the finger arrangement is manufacturability: each ply can be

cut square, and the joint length can remain relatively short. The drawback is that, if the spacing between neighbouring terminations is too small, the stress fields around adjacent resin pockets may interact. This reduces the effective load-transfer length and can make the joint sensitive to cutting tolerances [19, 20, 25].

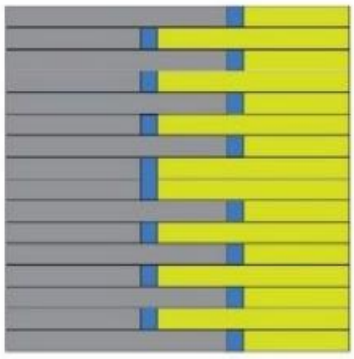


Figure 2.4: Finger-type end-to-end ply joint example [19]

Scarf-type end-to-end ply joints

In this category of ply joints, two main types can be Identified: asymmetric and symmetric scarf ply joints. Firstly, the asymmetric scarf ply joint has the ply terminations arranged along an inclined line through the thickness, creating a gradual transition from one laminate section to the other, as it can be seen in Figure 2.5; being created by cutting individual plies to different lengths before lay-up. The main advantage is that ply terminations are distributed over a longer distance, reducing the severity of a single local discontinuity [19, 20]. The main disadvantage is the increased joint length and the need for more accurate ply positioning. For reused glass fibre cut-outs, this may be difficult if the available pieces are irregular or short [26].

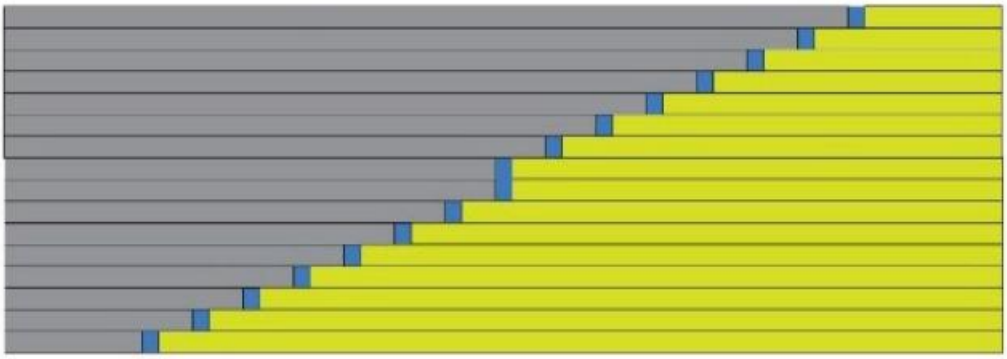


Figure 2.5: Asymmetric scarf-type end-to-end ply joint example [19]

Continuing with this category of ply joints, symmetric scarf ply joints place the termination pattern approximately symmetrically with respect to the laminate mid-plane. This is preferable when the objective is to reduce secondary bending and peel stresses, as in thin plates and shell elements; even a small eccentricity can introduce local bending under tensile loading [19, 23]. A symmetric end-to-end joint is therefore more appropriate for components where surface flatness and dimensional stability are important. Its drawback is that it requires a more controlled lay-up sequence and may be less tolerant of variable offcut shapes [26].

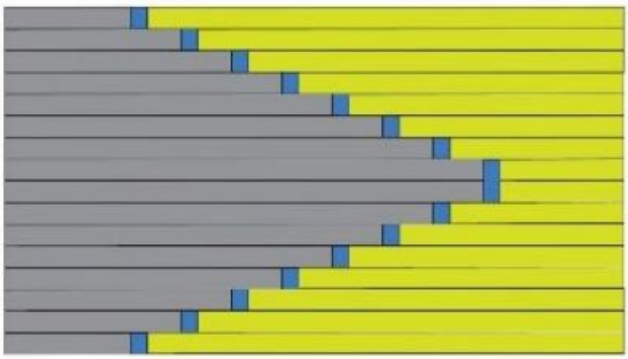


Figure 2.6: Symmetric scarf-type end-to-end ply joint example [19]

Interleafed scarf-type end-to-end ply joints

The interleaved-scarf configuration is a more advanced variant in which ply terminations are distributed in opposing directions through the laminate thickness. Baucom et al. [20] reported that an interleaved-scarf tiled architecture retained more than 92% of the strength of a continuous reference laminate, demonstrating the potential benefit of carefully distributing discontinuities. Ahamed [19] also investigated

interleaved-scarf concepts for ply-interleaved joints and identified the spatial distribution of terminations as a major design factor. For the present glass/glass case, the interleaved-scarf is attractive because it distributes resin-rich pockets and avoids creating a single dominant crack path [19, 20]. However, it is also the most demanding configuration in terms of cutting, labelling and placing each ply [26]. Similarly to the regular scarf-type ply joints, the Interleafed scarf-type ply joints can be distinguished between both asymmetric and symmetric varieties.

The asymmetric interleaved-scarf joint distributes the ply terminations in opposing directions, but the resulting pattern is not mirrored about the laminate mid-plane, as seen in Figure 2.7. The main benefit of this configuration is that it can reduce the severity of a single aligned discontinuity while potentially allowing a shorter or more adaptable joint layout than a fully symmetric design [19, 20]. However, the drawback is that the lack of symmetry may introduce eccentric load transfer, local bending and increased peel stresses, particularly in thin plates or shell-like components. This is important because previous work on asymmetric tapered laminates has shown that unsymmetric thickness transitions can promote delamination under tensile loading [23].

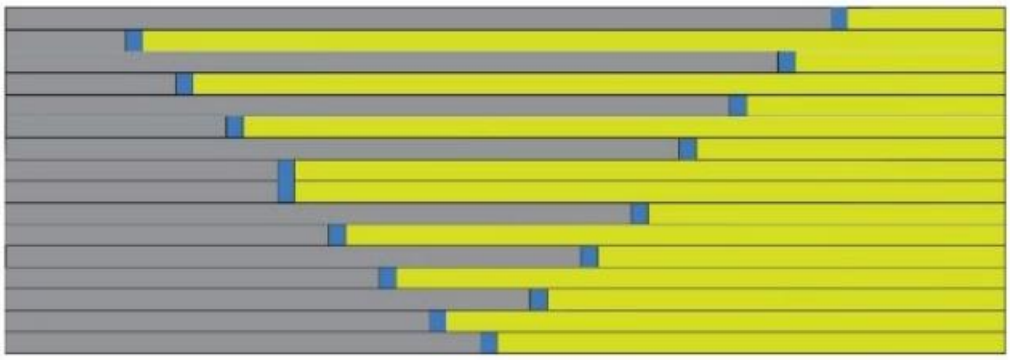


Figure 2.7: Asymmetric Interleafed scarf-type end-to-end ply join example [19]

The symmetric interleaved-scarf joint arranges the opposing ply terminations so that the joint pattern is approximately mirrored about the laminate mid-plane. This configuration is mechanically attractive because it helps balance the load path through the thickness and reduces the tendency for secondary bending under tensile loading. [23, 25]. Its main limitation is manufacturability. It requires accurate ply identification, controlled cutting lengths, careful stacking sequence control and stable placement during vacuum infusion. If these requirements are not achieved, the theoretical advantage of symmetry may be reduced by ply misalignment, waviness or excessive resin accumulation, decreasing the overall mechanical performance of the ply joint [26].

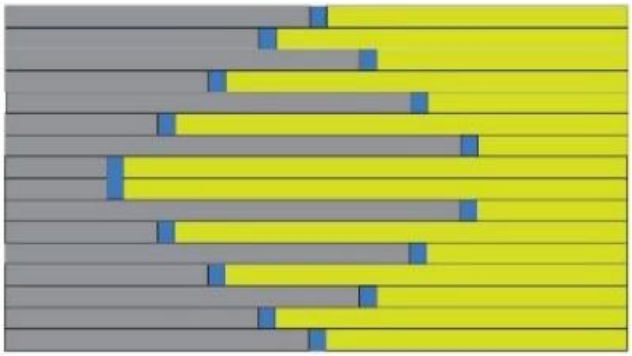


Figure 2.8: Symmetric interleafed scarf-type end-to-end ply joint example [19]

In summary, the advantages and disadvantages of each type of end-to-end ply joint configuration can be seen in Table 2.1.

Table 2.1: Advantages and disadvantages of the three main types of end-to-end ply joint configurations and their variants

Configuration	Mechanical benefit	Main drawback	Manufacturing comment
Staggered / finger joint	Distributes terminations over a finite length.	Sensitive to step length and cutting tolerance.	Good compromise between simplicity and performance.
Asymmetric scarf	Gradual transition in termination positions.	Can introduce bending if not balanced.	Requires accurate ply-length control.
Symmetric scarf	Reduces eccentricity and peel stresses.	Longer and more complex lay-up.	Better for flat plates and shell elements.
Asymmetric interleaved scarf	Reduced sensitivity of single weak through-thickness plane	Possibility of introduction of local bending and increased peel stresses	More adaptable to irregular off-cuts than symmetric variant.
Symmetric interleafed scarf	Balanced load path and transfer, reduced secondary bending	Most demanding to manufacture.	Suitable when great overall manufacturing control can be achieved

2.2.3. Relationship between joint configuration and numerical modelling

The selected joint configuration directly determines the numerical modelling strategy. A smeared laminate model may be sufficient for global stiffness predictions, but it cannot represent the stress concentrations produced by individual ply terminations. For end-to-end ply joints, the numerical model must therefore include the local geometry of resin-rich pockets or, at minimum, represent the discontinuities and interfaces where delamination may initiate [19, 20, 21]. Ahamed [19] used both analytical models and high-fidelity finite element models, combining continuum damage mechanics for intralaminar damage with cohesive zone modelling for interlaminar damage. This combined approach is relevant to the present dissertation because failure is expected to involve both ply-level damage and delamination at or near the resin-rich pocket [19, 24].

For the glass fibre reuse problem, there are two possible modelling levels. The first is a simplified design model, where each ply or orientation block is represented by continuum shell or solid elements and the interface between relevant layers is represented by cohesive elements or cohesive contact [19, 24]. This approach can predict how damage initiates and propagates between plies without requiring an extremely detailed representation of the cured resin microgeometry. The second is a local high-detail model of the joint region, where resin-rich pockets are explicitly included as resin material zones or simplified void-like regions. Ahamed [19] used void idealisation in part of the discontinuous laminate study because the resin pocket was much weaker than the fibres and because the objective was to understand stress concentration. For the present dissertation, modelling the pocket as real resin may be more physically representative if resin properties are characterised experimentally; if not, the resin-rich areas might be best left as simplified low-stiffness or void-like regions, since the stiffness of the matrix is considerably lower than that of the fibres [19, 21].

Cohesive zone modelling is particularly appropriate because end-to-end ply joints contain several potential delamination paths [19, 24]. Camanho et al. [24] described cohesive elements for mixed-mode progressive delamination, where tractions are related to displacement jumps, and damage evolves until the interface loses its load-carrying capacity. Turon et al. [27] further showed that cohesive simulations are sensitive to mesh size and that the cohesive zone length must be considered when selecting element dimensions. In practical Abaqus modelling, this means that a mesh sensitivity analysis is not optional. The mesh near the resin-rich pockets and cohesive interfaces must be fine enough to capture the stress gradients and the damage process, but not so fine that the model becomes impractical for multiple configurations [19, 27].

The relationship between configuration and model validation is also important. If the experimental programme compares aligned, finger, scarf and interleaved-scarf joints, the numerical model should reproduce not only the maximum load but also the observed failure location and sequence [19]. A model that predicts a similar ultimate force but fails in the wrong region should not be considered fully validated. The relevant outputs include axial stress in the main load-bearing plies, interlaminar shear and peel stresses near resin pockets, cohesive damage variables, matrix damage variables and global load-displacement response [19, 24]. Experimental tensile tests, optical inspection and post-failure fractography can then be used to confirm whether the model captures the real load-transfer mechanism [19, 26].

Overall, end-to-end ply joints should be treated as engineered discontinuities. Their performance depends on how resin-rich pockets are sized, spaced and aligned through the thickness [19, 20, 21, 25]. The numerical model must therefore be built around the configuration: the joint geometry defines the expected stress concentrations, the possible delamination paths and the mesh requirements [19, 24, 27]. This makes joint design, tensile testing and cohesive zone simulation parts of the same optimisation problem rather than independent tasks.

2.3. Numerical modelling of composites with discontinuities

2.3.1. Abaqus CAE software and modelling

Finite element analysis is an essential tool for studying and/or predicting the mechanical response of composite laminates because it allows the stress state, damage initiation and damage propagation to be examined in regions that are difficult to observe experimentally [19, 24]. In the present dissertation, Abaqus/CAE is used to construct the tensile-test models, define the laminate lay-up, assign material behaviour, introduce cohesive interfaces, apply boundary conditions and analyse the resulting damage fields. This is especially relevant for end-to-end glass fibre ply joints, where the critical behaviour is expected to occur near ply terminations and resin-rich pockets rather than in the uniform region of the laminate [19, 20, 21].

The modelling strategy must represent both intralaminar and interlaminar failure. Intralaminar failure refers to damage inside the plies, such as matrix cracking, fibre failure or shear-related degradation. Interlaminar failure refers to the separation of neighbouring plies, which is normally described as delamination [19, 24]. Ahamed [19] used high-fidelity finite element models for ply joints and combined

continuum damage mechanics for ply-level failure with cohesive zone modelling for delamination. This approach is relevant to the present dissertation because tensile failure of an end-to-end joint is expected to involve the interaction between local ply damage and delamination around resin-rich discontinuities [19, 24].

Abaqus FEA software (or simply Abaqus in this work) simulations can be performed using implicit or explicit procedures. Abaqus/Standard is generally associated with implicit solution schemes, whereas Abaqus/Explicit uses an explicit central-difference integration procedure [28]. Abaqus documentation states that explicit increments are relatively inexpensive because they do not require the solution of a global system of simultaneous equations at every increment [28]. Although the explicit procedure is fundamentally dynamic, its advantages can also be used for slower quasi-static processes when inertial effects are kept under control [29]. This is the reason why dynamic/explicit analysis can be appropriate for quasi-static tensile simulations of composite joints [29, 30].

In this dissertation, the dynamic/explicit approach is preferred because cohesive damage and composite damage introduce strong nonlinearities. When damage begins, interface stiffness is reduced, and the local load path changes rapidly. In an implicit static analysis, these sudden stiffness changes can cause convergence difficulties, especially when delamination grows unstably or when several damage mechanisms interact [30]. Static/implicit analysis is therefore not used as the main numerical approach, not because it is inappropriate for all composite problems, but because the progressive degradation of cohesive and composite materials makes the explicit procedure more robust for the intended simulations [30].

However, the use of an explicit step for a quasi-static tensile test requires careful verification. The loading should be applied gradually, normally through a smooth displacement amplitude, and the total step time must be selected so that the response is not dominated by inertia [29]. Abaqus documentation recommends monitoring kinetic energy relative to internal energy in quasi-static explicit simulations, with kinetic energy kept as a small fraction of the internal energy [29]. For this reason, energy plots are part of the numerical validation procedure, together with the comparison of load-displacement curves and the inspection of damage variables [19, 27].

2.3.2. Cohesive zone modelling

Cohesive zone modelling is a numerical method used to simulate crack initiation and crack propagation along interfaces. Instead of assuming that a crack already exists, a cohesive law is assigned to an interface

that can initially transmit tractions and later degrade as separation increases, also known as traction-separation behaviour [24, 31]. In composite laminates, this approach is particularly useful because delamination often develops between plies, around resin-rich regions or near geometric discontinuities [24]. Abaqus documentation describes cohesive elements as elements capable of modelling the initial loading, damage initiation and damage propagation leading to eventual failure [32]. For end-to-end ply joints, cohesive zone modelling is appropriate because the fibres are interrupted at the ply ends. The load must therefore be transferred through the resin and neighbouring plies, generating interlaminar shear and, depending on the configuration, local peel stresses [19].

In a detailed finite element model, cohesive elements can be inserted between continuum shell or solid representations of the plies. This allows the in-plane response of the composite plies to be separated from the interlaminar failure process [19, 24]. However, cohesive models must be meshed carefully. Turon et al. [27] showed that cohesive zone simulations are sensitive to element size and proposed an engineering approach to reduce mesh-size effects in delamination simulations. A mesh sensitivity analysis is also necessary in order to keep the simulations computationally practical, especially when many of them need to be carried out [27].

Traction-separation behavior laws

Cohesive zone modelling can be used to represent the mechanical connection between coincident nodes belonging to adjacent elements, allowing a zero-thickness interface between different materials to be simulated [32]. It can also be applied between separated surfaces to represent a thin layer with finite thickness, such as an adhesive bond [32]. In this approach, the cohesive law describes how the tractions transmitted across the interface vary with the relative opening or separation displacement between the connected surfaces [24, 31]; where this law is described by Eq. (2.1) [33].

$$\sigma_i = k_{ii}\delta_i \;\; (i = n, s, t); \quad \begin{pmatrix}\sigma_n \\ \sigma_s \\ \sigma_t\end{pmatrix} = \begin{bmatrix}k_{nn} & 0 & 0 \\ 0 & k_{ss} & 0 \\ 0 & 0 & k_{tt}\end{bmatrix} \begin{Bmatrix}\delta_n \\ \delta_s \\ \delta_t\end{Bmatrix} \tag{2.1}$$

where σ_n refers to the cohesive stresses of the material in tension, and σ_s and σ_t the cohesive stresses in shear in directions 2 and 3 respectively, with direction 3 also referred to as tearing. Moreover, the stiffness matrix contains the three parameters k_{nn}, k_{ss} and k_{tt}; with δ_n, δ_s and δ_t being the relative displacements between the top and bottom of the cohesive layer in their respective directions [33]. Additionally, the ratio between normal modulus relative to the cohesive element thickness represents the stiffness matrix component in the normal direction, as seen in Eq. (2.2), with the shear stiffness matrix

components being defined by the ratio between the shear modulus and the adhesive thickness, also seen in Eq. (2.3) [33].

$$k_{nn} = \frac{E}{t_A} \tag{2.2}$$

$$k_{ss} = k_{tt} = \frac{G}{t_A} \tag{2.3}$$

In order to define the behaviour evolution of the cohesive material, a behaviour law must be selected. Initially, a linear-elastic behaviour is assumed up until the damage initiation point, where the material starts to degrade. After this point, the behaviour of the cohesive material can be defined with various Interface failure criteria, which will dictate the point at which, if the stresses surpass it, the material will become damaged [33].

Based on previous studies [34, 35, 36], a quadratic nominal stress criterion, also known as QUADS, is the most suitable failure criterion for this dissertation, as the cohesive regions in the joint are subjected to mixed-mode loading, involving both normal and shear tractions [24, 31, 37]. This criterion is more suitable than a simple maximum stress criterion because it accounts for the combined contribution of peel and shear stresses to damage initiation [37]. This is particularly relevant for end-to-end and overlap ply joints, where local stress concentrations develop near ply terminations and resin-rich regions [19, 33]. The criterion is therefore appropriate for predicting the onset of cohesive damage, while the subsequent damage evolution is controlled through the fracture energy-based cohesive law [24, 31, 38]. Eq. (2.4) represents the behaviour that is followed by the QUADS failure criterion, as damage is predicted to initiate once it is satisfied.

$$\left\{\frac{\langle \sigma_n \rangle}{\sigma_n^0}\right\}^2 + \left\{\frac{\sigma_s}{\sigma_s^0}\right\}^2 + \left\{\frac{\sigma_t}{\sigma_t^0}\right\}^2 = 1 \tag{2.4}$$

In the previous equation, the maximum values of the nominal stress in tension, shear and tearing are represented by σ_n^0, σ_s^0 and σ_t^0 respectively. Moreover, the Macauly brackets ($\langle \quad \rangle$) represent the fact that damage cannot be initiated by stresses in pure compression [33].

As the damage needs to be defined, a scalar variable is defined to model the linear softening. The law that this variable, D, follows can be observed in Eq. (2.5) [33].

$$0 < D < 1; \quad D = \frac{\delta_m^f(\delta_m^{max} - \delta_m^0)}{\delta_m^{max}\left(\delta_m^f - \delta_m^0\right)} \tag{2.5}$$

where the effective displacements are defined for the initial moment by δ_m^0, the maximum value by δ_m^{max}, and the final moment by δ_m^f. Each of these effective displacements can be calculated by following the expression presented in Eq. (2.6) [33].

$$\delta_m = \sqrt{\langle \delta_n \rangle^2 + {\delta_s}^2 + {\delta_t}^2} \tag{2.6}$$

Having established the previous statements, the stresses in the softening region are defined by complying with Eq. (2.7) [33].

$$\sigma_i = \begin{cases} k_{ii}\delta_i & 0 \le \delta_i \le \delta_i^0 \\ (1-D)k_{ii}\delta_i & \delta_i^0 \le \delta_i \le \delta_i^f \\ 0 & otherwise \end{cases} \quad i = n, s, t \tag{2.7}$$

This behaviour progression can be observed more visually in Figure 2.9.

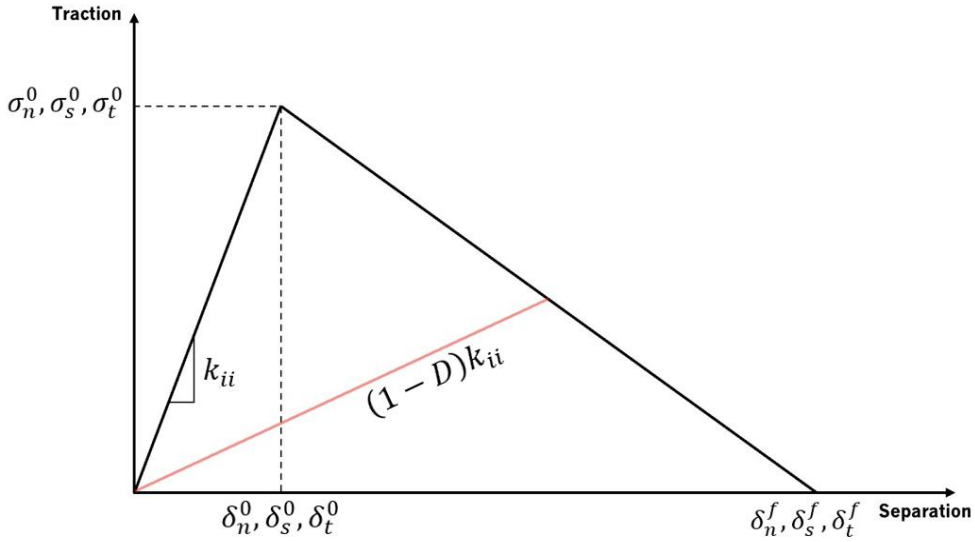


Figure 2.9: Bilinear cohesive law material behaviour graph [39]

2.4. Final Remarks

The development of this dissertation is important because it addresses a specific but underexplored route for improving the circular use of composite materials in the wind energy sector. Wind turbine blade production generates several waste streams, including dry fibre offcuts, composite offcuts, resin residues and vacuum consumables [3, 5]. At the same time, fibre-reinforced polymer composites remain difficult to recycle because of the strong bond between fibres and thermoset matrices, and many recycling routes reduce the original material value or require additional energy, cost and processing [2, 11, 12]. For this reason, the direct reuse of clean virgin glass fibre manufacturing waste is a valuable alternative, since it

preserves more of the original fibre architecture and avoids treating mechanically useful material as low-value waste [13, 14, 15].

The main benefit of this dissertation is that it connects waste management with a practical materials-engineering solution. Instead of focusing only on recycling, filler production or end-of-life blade reuse, the work investigates whether discarded virgin glass fibre mats can be joined into larger laminate components through end-to-end configurations. This is relevant for the CirWind project because the intended applications, such as urban furniture and equipment, do not require the same qualification level as primary wind turbine blade structures, but still require sufficient stiffness, strength, durability and reliability. Therefore, the dissertation can help identify joint configurations that allow small or irregular manufacturing offcuts to be transformed into useful non-critical components [4, 19, 20, 33].

Based on research done for the literature review, no previous work appears to address the exact combination proposed in this dissertation: the reuse of discarded virgin glass fibre mat cut-outs from wind turbine blade manufacturing, joined through optimised end-to-end and overlap ply configurations, assessed by both experimental tensile testing and Abaqus cohesive zone simulations. Previous studies have investigated wind turbine blade waste and recycling routes [1, 2, 3, 5, 11, 12], reuse of blade-derived composites [14], glass fibre fabric offcuts in geopolymer matrices [15], adhesive and ply-joint mechanics [4, 19, 20, 21, 22, 23, 25, 33], and cohesive zone modelling of delamination [24, 27, 31, 32, 34, 35, 36, 37, 38]. However, these works do not specifically combine the material stream, joint concept, application context and numerical-experimental validation strategy proposed here. This gives the dissertation its novelty and practical relevance within the broader transition from disposal-based composite waste management to circular composite material use [13, 14, 15].

3. NUMERICAL MODELLING

3.1. Modelling strategy

3.1.1. Abaqus CAE dynamic/explicit simulation mode

Dynamic/Explicit analysis was selected for the numerical simulations because the mechanical response of the joint models involves progressive damage, stiffness degradation and possible delamination growth [19, 24, 31, 40]. In these conditions, the numerical problem becomes highly nonlinear, particularly when cohesive elements begin to lose stiffness, and the load path is redistributed through the laminate [24, 31, 40]. Abaqus/Explicit is well suited to this type of problem because it does not require convergence iterations at each increment, unlike implicit procedures, and can therefore handle sudden damage evolution and complex contact or interface degradation more robustly [28, 30, 41]. For this reason, the explicit procedure was considered more appropriate than a static/implicit approach for simulating the tensile failure of the composite joint configurations.

However, although a Dynamic/Explicit step was used, the physical objective of the simulations was to reproduce a quasi-static tensile test. Therefore, the response of the model must not be dominated by inertial effects [29, 42]. The loading must be applied gradually, using a sufficiently smooth displacement history and an adequate step time, so that the kinetic energy remains small in comparison with the internal energy of the system [29, 42, 43]. This is especially important in composite and cohesive zone simulations, where excessive loading rate effects may artificially increase or decrease the predicted failure load and modify the damage progression [42, 43].

For this reason, the verification of the energy balance is an essential part of the numerical methodology. For every simulation performed, the evolution of kinetic energy, internal energy, artificial strain energy, viscous dissipation, external work and total energy must be checked to confirm that the analysis remains quasi-static [42, 44]. In particular, the kinetic energy should remain much lower than the internal energy during most of the simulation, and any significant increase should be carefully analysed to ensure that it is associated with physical damage progression rather than inertial effects [29, 42, 43]. Only simulations that satisfy these energy requirements can be considered suitable for comparison with experimental tensile tests. This energy verification ensures that the Dynamic/Explicit formulation is used as a numerical

tool for robust damage simulation, while still representing the quasi-static behaviour required for the dissertation [29, 42, 43, 44].

3.1.2. Cohesive element usage and definition

Cohesive elements were used to represent the resin-rich interlaminar regions where damage and delamination may initiate between adjacent bidirectional glass fibre plies. In the numerical model, these elements were placed at every interface where one bidirectional ply comes into contact with another bidirectional ply, allowing the load transfer between neighbouring layers to be governed by a cohesive traction–separation law. This modelling strategy makes it possible to simulate the initial elastic response of the interface, the onset of cohesive damage, and the progressive degradation of the interface as separation increases [31, 32].

3.2. Modelling process

Since the numerical modelling process was carried out before any experimental tensile campaign and without any material properties being determined in advance, its main objectives were to define a suitable protocol for simulating the different ply joint configurations and develop a model capable of reproducing the approximate expected experimental behaviour. Following this initial stage, material characterisation and model fine-tuning should be performed to improve the accuracy of the numerical model in predicting the behaviour of waste glass fibre composite laminates.

3.2.1. Component definition

Glass fibre composite elements

Shell element definition

According to the research done by Ahamed et. al. [19], the best way to model different fibre composite plies in a numerical simulation is to do it individually. However, this approach has a great computational cost, as the number of elements that need to be modelled is very high.

In the scope of the CirWind project, waste bi-directional glass fibre mats, composed of two layers of fibres stitched together and orientated perpendicularly one on top of each other, in 0°/90° orientations, as seen in Figure 3.1; a preliminary study was performed to determine if modelling each bidirectional mat

layer (and not the two individual plies) was a viable modelling strategy due to the time requirements that this method needs.

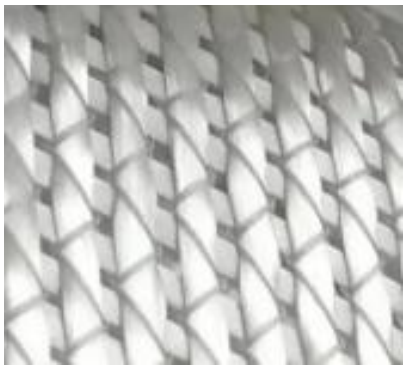


Figure 3.1: Example of biaxial 0°/90° stitched glass fibre mat [45]

Firstly, a numerical simulation was run with each layer of unidirectional glass fibres modelled as an individual continuum shell element with cohesive elements in between them (strategy 1), as solid elements are not allowed for use with composite materials by the numerical simulation software Abaqus CAE. Lastly, the same was done with shell elements that each represented each section of bidirectional mat (two 0°/90° plies), where the fibre directions were later defined in relation to their thickness; with once again, cohesive elements connecting all the different shell elements (strategy 2). The differences in modelling strategy (1 and 2) can be seen in Figure 3.2, where the thicker elements represent the continuum shells representing the composite material, while the very thin elements that sit in between those continuum shells represent the cohesive elements that bound them together.

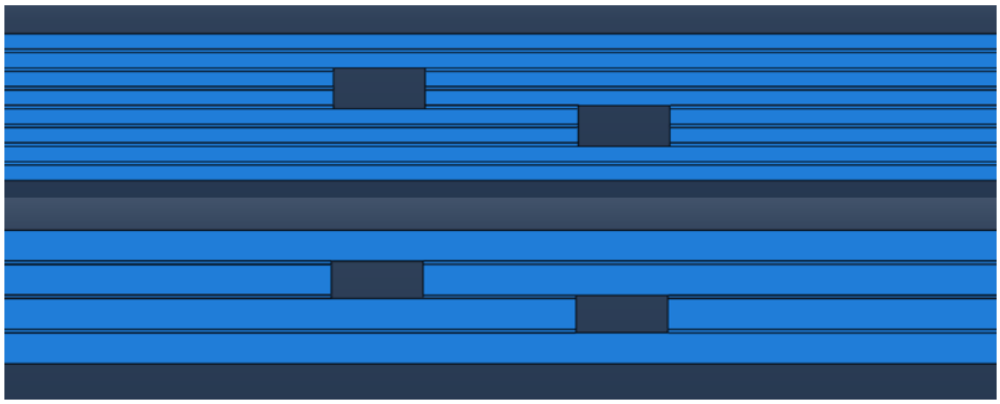


Figure 3.2: Individual fibre direction shell element modelling strategy 1 (upper half) and bidirectional glass fibre mat shell element modelling strategy 2 (lower half)

As can be seen in the previous figure, in the upper half of the picture, the individual glass fibre direction shell element modelling strategy can be observed in comparison to the bidirectional glass fibre mat shell element modelling strategy, where each shell element contains both 0° and 90° directions of the glass fibres. It is quite apparent that the difference in size and number of elements is quite large, leading to the increased simulation times required by the individual fibre direction simulation strategy, which are in the order of 3 times higher compared to the bidirectional shell element modelling strategy. It must be mentioned that the stacking, configuration and location of elements that have been showcased in Figure 3.2 are consistent with the study of the critical ply end-to-end joint parameters that was performed during the work carried out to complete this dissertation.

The main objective of this study is to observe the delamination pattern of the individual fibre direction modelling strategy, in order to determine if any type of delamination occurs between the 0° and 90° fibre direction shell elements, under a longitudinal unidirectional tensile stress state applied at laminate level. If any delamination is detected between the 0° and 90° directions that come pre-stitched in the waste glass fibre mats, it would render the bidirectional glass fibre shell element modelling strategy unviable, as delamination is impossible to simulate with a singular multi-fibre-direction shell element [46].

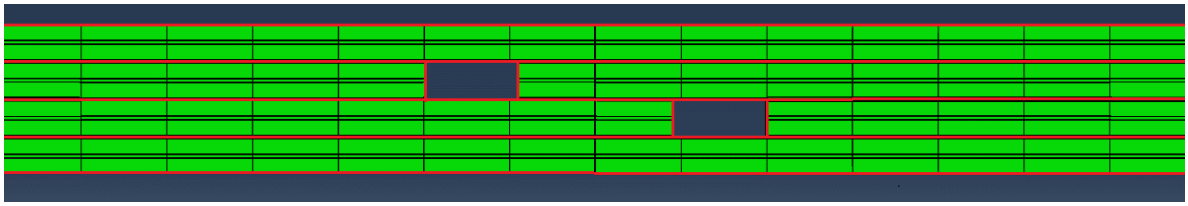


Figure 3.3: Individual fibre direction modelling strategy shell element disposition before the simulated failure point of the laminate

In Figure 3.3, the shell elements representing each of the directions of the fibres of the mats used in this ply joint configuration can be observed before any delamination caused by the failure of the cohesive elements that sit between them in the numerical simulation. Red lines have been added to help delineate the boundaries between separate bidirectional waste glass fibre mats. For the purpose of clarity, from a visual point of view, all the cohesive elements of the system have been eliminated in both Figure 3.3 and Figure 3.4.

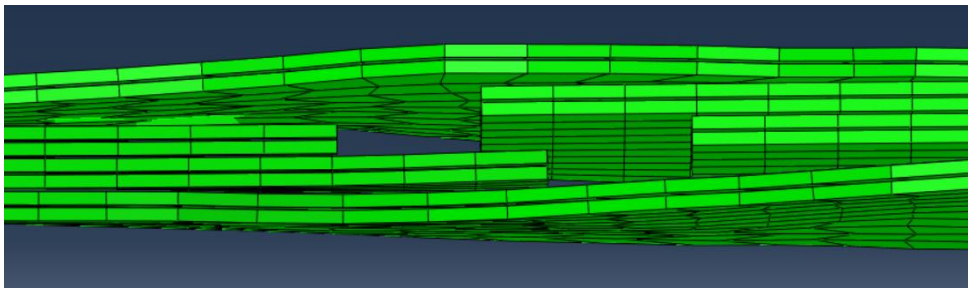


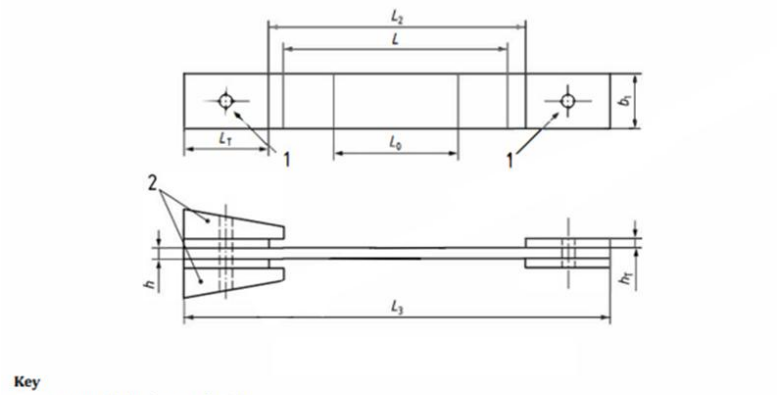
Figure 3.4: Individual fibre direction modelling strategy shell element disposition after the simulated failure point of the laminate

In Figure 3.4, the distribution of the shell elements after the simulated laminate failure can be observed. When compared to Figure 3.3, it can be seen that, even after overall laminate failure, the shell elements that belong to the same stitched glass fibre mat but represent the two different fibre directions of that same mat stay together, presenting no signs of delamination. The only simulated delamination is between different bidirectional waste glass fibre mats, as the cohesive elements located in the delamination locations fail.

After the simulations were carried out, making use of the material properties defined in Section 3.2.2 of this dissertation, it was concluded that no delamination was to be expected between the pre-stitched 0° and 90° glass fibre direction sections. It is also pertinent to mention that the stress-strain and load-displacement curves produced by both modelling methods were very similar, but the results will be analysed in Section 3.4 of this dissertation.

Composite laminate geometry

Since this project aims to test different ply joint configurations with the waste glass fibre material, tensile tests will have to be performed. It is because of this that the laminate geometry modelled in the numerical simulations has to be in accordance with norm ISO 527-4:2023 of the determination of tensile properties in plastics; more specifically, the test conditions for isotropic and orthotropic fibre-reinforced plastic composites. More details about this norm can be observed in Annex A; but in summary, it specifies that the laminate has to have an overall length of 250mm or more, an overall width either 25 or 50mm with a tolerance of 0.5mm in both cases, and a thickness between 2 and 10mm in total [47].



Key

1 centrings holes (optional), ϕD

2 jaws

Symbol	Name	Dimensions in millimetres	
		Type 2	Type 3
L_3	Overall length	≥250	≥250
L_2	Distance between end tabs	—	150 ± 1
b_1	Width	25 ± 0,5 or 50 ± 0,5	25 ± 0,5 or 50 ± 0,5
h	Thickness	2 to 10	2 to 10
L_0	Gauge length (recommended for extensometers)	50 ± 1	50 ± 1
L	Initial distance between grips (nominal)	150 ± 1	150 ± 1
L_T	Length of end tabs	—	≥50
h_T	Thickness of end tabs	—	1 to 3
D	Diameter of centring holes	3 ± 0,25	3 ± 0,25

NOTE Requirements on specimen quality and parallelism are given in ISO 527-1:2019, 6.4.

Figure 3.5: ISO 527-4:2023 geometrical restrictions for tensile tests for fibre-reinforced plastic composites [47]

The G-0/1/0/1-1264 waste biaxial glass fibre mats will be used in the dissertation. The datasheet indicated that each layer of biaxial glass fibre woven mat has a total thickness of 1.01mm [48]. This is the same thickness that will be given to each of the shell elements that will represent every layer of biaxial glass fibre mat; with half of its thickness being defined as having the fibres oriented in the 0° direction and the other with the fibres oriented in the 90° direction. See Figure 3.6 for clarification of these directions.

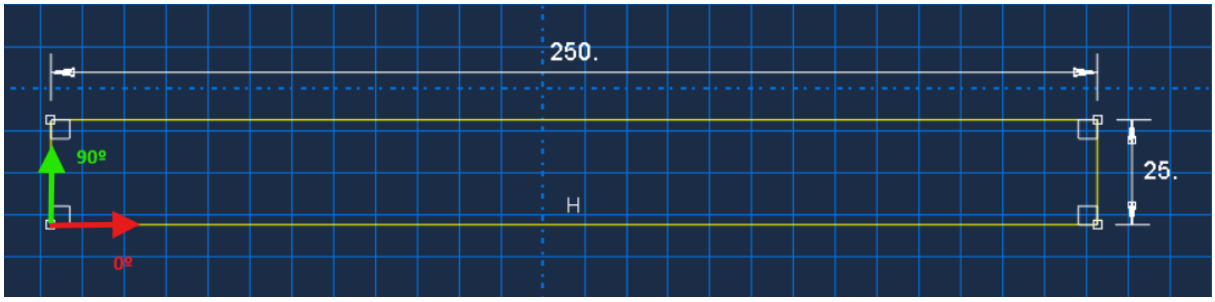


Figure 3.6: Overall dimensions for the length and width for the laminate and fibre directions

Composite shell element section definition

As previously mentioned, each layer of biaxial glass fibre mat is 1.01mm thick; hence, each layer of fibres in the perpendicular direction needs to be defined as 0.5005mm thick, and stacked one on top of the other. For this, in the "property" menu of the Abaqus CAE interface, a composite continuum shell section must be created and assigned to each composite element that is being included in the system. After doing this, the thicknesses and orientations of each directional layer of the glass fibre mat must be defined similarly to the one shown in Figure 3.7.

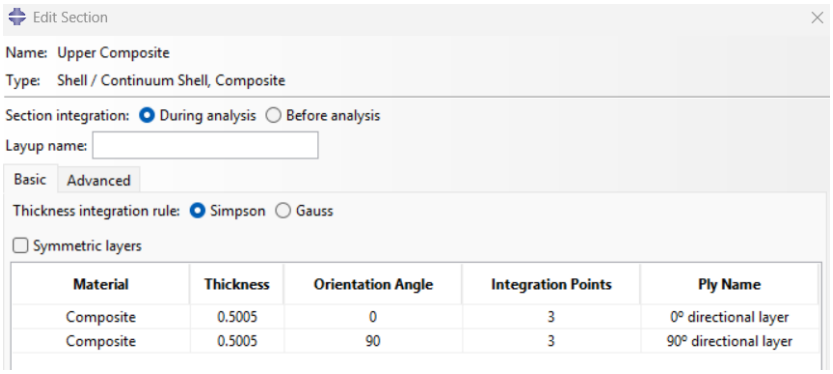


Figure 3.7: Section definition of the composite shell element to define the different fibre direction regions

As for the arrangement of the staking sequences, the 0° direction-oriented fibre regions have always been placed closer to the symmetry plane of the laminate. This means that for the layers positioned on top of the symmetry plane of the laminate, the 0° fibre-oriented region will always be on the bottom half of that particular layer, and for the layers positioned lower than the symmetry plane of the laminate, the 0° fibre-oriented region will always be on the top half of that particular layer. This can be seen more easily in Figure 3.8, where the upper composite layers in relation to the symmetry plane have been coloured in blue, the lower composite layers in green and the cohesive layers in orange; with the symmetry plane being represented by the yellow line. Moreover, in Figure 3.9, the layers of 0° and 90° fibre-oriented regions have been highlighted with red lines and black circles, respectively, to represent how the fibres would be seen in a real composite laminate.



Figure 3.8: Representation of upper, lower and cohesive layers in relation to the symmetry plane in a 4-composite-mat layered laminate

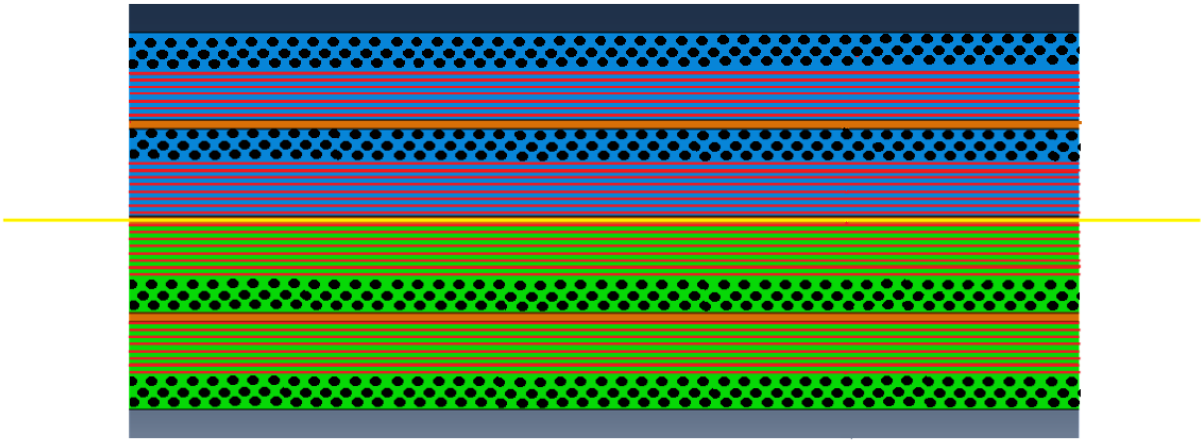


Figure 3.9: Representation of fibre orientation regions within the upper and lower composite shell elements in a 4 composite mat layered laminate

Cohesive elements

As for the cohesive elements that will be placed in between the continuum shell elements when performing the numerical simulations, a nominal cohesive thickness of 0.1 mm was selected because it provides a physically reasonable representation of the resin-rich interlaminar region expected between vacuum-infused composite laminates [19, 49, 50]. A smaller thickness, such as 0.05 mm, may under-represent the resin-rich volume and increase the local interface stiffness if the cohesive stiffness is derived from the layer thickness [49, 50]. A larger thickness, such as 0.2 mm, may introduce excessive resin-rich compliance and alter the load transfer path, making the model behave more like a thick adhesive joint than an interlaminar interface [33, 51, 52]. Therefore, 0.1 mm is used as a balanced initial value, but its influence should be verified through a cohesive-thickness sensitivity analysis [27, 33].

Cohesive element section definition

The correct section that should be applied to the cohesive elements when performing a numerical simulation in Abaqus CAE should be selected in the "other" type of section, selecting the cohesive option.

3.2.2. Material property definition

Before the explanation of the material definition for the numerical simulations, it is necessary to recall that these simulations were done before the specimen tensile testing, having defined the material data before knowing what materials would be used for such tensile tests. This is why, for the numerical material data, common values for glass fibre-epoxy composites have been extracted from online sources.

Glass fibre composite

Elastic engineering constants and density

Since the mechanical properties of fibre-reinforced composites depend on the relative volume fractions of the reinforcement and matrix phases, the overall material properties must be calculated by considering the contribution of each constituent to the final composite response [53].

For the numerical simulations, for the continuum shell elements representing each of the layers of biaxial glass fibre, a fibre-matrix ratio of 0.6 was assumed. A fibre volume fraction of 0.6 is a reasonable starting point because it represents a highly reinforced composite while still allowing sufficient matrix for fibre bonding and stress transfer. Since composite stiffness and strength depend strongly on the fibre/matrix volume fractions, this value provides a realistic first estimate for numerical material definition [53]. It is also suitable for vacuum-infused laminates, where fibre compaction and resin infiltration determine the final reinforcement content [8]. However, this value should be treated as an initial assumption and later adjusted using experimental density, burn-off, microscopy, or supplier data.

Having established this parameter, the individual material properties for the glass fibres and the matrix must be compiled. For the glass fibre reinforcement, generic E-glass properties were used [54]; whereas for the matrix, the SR InfuGreen 810 / SD 882X epoxy system was used as a representative matrix reference because it is specifically formulated for injection and vacuum infusion processes and provides the density and elastic properties required for the initial numerical material definition [55]. The compiled individual material properties that are relevant for both the fibre reinforcement and the matrix can be observed in Table 3.1, where each numerical value has been displayed along with its symbol and measurement units.

Table 3.1: Individual material properties for the fibre reinforcement and matrix of the composite laminate used in the numerical simulations [54, 55]

Parameter	**E-Glass fibre reinforcement** (f) [54]	**SR InfuGreen 810 / SD 882X epoxy matrix** (m) [55]
Elasticity modulus $\boldsymbol{E}$	72400 MPa E_f	3040 MPa E_m
Poisson ratio $\boldsymbol{\nu}$	0.2 ν_f	0.32 ν_m
Density $\boldsymbol{\rho}$	2570 kg/m³ ρ_f	1160 kg/m³ ρ_m
Shear modulus (calculated) $\boldsymbol{G}$	30167 MPa G_f	1152 MPa G_m
Volume fraction $\boldsymbol{V}$	0.6 V_f	0.4 V_m

where the shear modulus was calculated by using the following formula [56]:

$$G = \frac{E}{(2 \cdot (1 + \nu)} \tag{3.1}$$

To obtain the engineering constants for the combined material properties of the composite, the rule of mixtures or ROM was used, which states that the overall property of a composite material can be estimated from the weighted contribution of its constituents, usually the fibre and matrix, according to their respective volume fractions [53]:

$$P_c = V_f P_f + V_m P_m \tag{3.2}$$

where P_c is the composite property, P_f and P_m are the fibre and matrix properties, and V_f and V_m are their volume fractions respectively.

For the engineering constants of the elasticity modulus (E), Poisson ratios (ν) and shear modulus (G) in all three directions, the classical ROM approach was selected for its simplicity, even though it is not the most precise method of determining the elastic engineering constants of a composite laminate [57]; since obtaining a working numerical simulation model is the priority, with precision being pursued later. The expressions used to calculate these elastic properties and the density for the composite shell elements can be observed from Eq. (3.3) to Eq. (3.9). Micromechanical rule of mixture methods such as the one used by C. C. Chamis [58] should be pursued in the future for more accurate results. It must be noted

that direction 1 represents the fibre direction, direction 2 the transverse in-plane direction in relation to the fibres, and direction 3 the through-thickness direction.

$$E_1 = V_f E_f + V_m E_m \tag{3.3}$$

$$\frac{1}{E_2} = \frac{1}{E_3} = \frac{V_f}{E_f} + \frac{V_m}{E_m} \tag{3.4}$$

$$\nu_{12} = \nu_{13} = V_f \nu_f + V_m \nu_m \tag{3.5}$$

$$\nu_{23} \approx \nu_m \tag{3.6}$$

$$\frac{1}{G_{12}} = \frac{1}{G_{13}} = \frac{V_f}{G_f} + \frac{V_m}{G_m} \tag{3.7}$$

$$G_{23} \approx G_m \tag{3.8}$$

$$\rho_c = V_f \rho_f + V_m \rho_m \tag{3.9}$$

where ρ_c is the average density of the composite shell elements and Eq. (3.6) and Eq. (3.8) represent approximations made due to the matrix-dominated response in the transverse 2–3 plane of a unidirectional composite. These assumptions constitute first-order engineering approximations and neglect the additional constraint introduced by the fibres; consequently, more detailed micromechanical models should be used in the future to account for the constraint imposed by the fibres and their volume fraction [59]. Applying the individual material properties found in Table 3.1 to these expressions, the combined properties of the composite can be observed in Table 3.2.

Table 3.2: Combined composite shell element elastic properties and density

E_1	E_2	E_3	ν_{12}	ν_{13}	ν_{23}	G_{12}	G_{13}	G_{23}	ρ_c
44656 MPa	7149.68 MPa	7149.68 MPa	0.248	0.248	0.32	2722.88 MPa	2722.88 MPa	1152 MPa	2006 kg/m³

Damage criterion

For the composite laminate regions, it was necessary to define a damage criterion because the simulation was not intended to reproduce only the initial linear-elastic response of the material, but also the initiation and progression of failure under tensile loading [40]. In fibre-reinforced composites, damage does not occur through a single homogeneous yielding mechanism, but through different failure modes such as fibre tension, fibre compression, matrix tension and matrix compression [40]. Therefore, if no damage criterion is defined, the Abaqus model can calculate stresses and strains, but it cannot identify when the

composite plies start to lose load-carrying capacity or how stiffness degradation develops after damage initiation [40].

The Hashin damage criterion was selected for the composite shell elements because it is specifically formulated for fibre-reinforced composite laminates and separates the main failure mechanisms into fibre-dominated and matrix-dominated modes [40]. This is particularly suitable for the present model, where the laminate response depends strongly on the ply orientation and where tensile loading is mainly carried by the fibres aligned with the loading direction, while off-axis plies contribute more through matrix and shear-dominated behaviour [19]. By distinguishing between fibre and matrix damage, the Hashin criterion provides more physically meaningful information than a simple global failure criterion, since it allows the simulation to indicate whether failure is governed by fibre damage, matrix damage, or a combination of both mechanisms [40].

In this dissertation, the use of the Hashin damage criterion is therefore appropriate because the numerical model aims to reproduce progressive intralaminar damage in the composite adherends [40], while interlaminar separation is represented separately through cohesive elements governed by a traction-separation law [24, 31].

Since the necessary parameters to input into the material property menu in the Abaqus CAE numerical simulation software must be for the composite material already including the reinforcement fibres along with the matrix, once again, typical values for glass fibre-epoxy composites were assumed. It is important to mention that due to the lack of a single source where the all the Hashin material property values could be extracted from, and the scarcity of information regarding this subject, multiple sources had to be used, rendering the data collected not homogeneous it terms of fibre-matrix volume fraction; as material properties change according to this ratio, as seen previously in Section 3.2.2 of this dissertation.

Table 3.3: Hashin damage composite material property values

Longitudinal tensile strength	X_T	1060 MPa [60]
Longitudinal compressive strength	X_C	610 MPa [60]
Transverse tensile strength	Y_T	31 MPa [60]
Transverse compressive strength	Y_C	118 MPa [60]
Longitudinal shear strength	S_L	72 MPa [60]
Transverse shear strength	S_T	50 MPa [61]

Table 3.4: Hashin damage evolution settings selection and composite material property values

Type of evolution	Energy (default)	
Type of softening	Linear (default)	
Longitudinal tensile fracture energy	G_{XT}	45 N/mm [62]
Longitudinal compressive fracture energy	G_{XC}	40 N/mm [62]
Transverse tensile fracture energy	G_{YT}	0.165 N/mm [62]
Transverse compressive fracture energy	G_{YC}	0.8 N/mm [62]

It must be mentioned that in the Hashin damage evolution menu, for the type of evolution, energy was selected; and for the type of softening, the linear option was selected for all numerical simulations.

Cohesive elements

Since the cohesive elements inserted in between the composite shell elements are meant to represent the very thin matrix layer that sits between plies when producing a composite element via vacuum infusion, as this modelling approach is suitable for vacuum-infused laminates, since delamination propagation is commonly associated with the resin-rich region formed between neighbouring plies during manufacturing [63]; the density of the cohesive elements was assumed to be the same as the SR InfuGreen 810 / SD 882X epoxy resin [55]. As for the elastic material properties, they were obtained from Falaschetti [64] PhD dissertation, since no exact values were found for the SR InfuGreen 810 / SD 882X epoxy resin traction-separation behaviour specifically.

Table 3.5: Density and elastic behaviour settings selection and cohesive element material property values

Type of behaviour	Traction	
Moduli time scale (for viscoelasticity)	Long-term (default)	
Density	ρ_{coh}	1160 kg/m³ [55]
Normal/opening stiffness	E/E_{nn}	3000 MPa/mm [64]
First shear/sliding stiffness	$G1/E_{ss}$	1200 MPa/mm [64]
Second shear/tearing stiffness	$G2/E_{tt}$	1200 MPa/mm [64]

It must be mentioned that in the Falaschetti [64] PhD dissertation, the values for the opening, sliding and tearing stiffnesses are referred to with the following symbols, respectively: K_{nn}, K_{ss} and K_{tt}. These symbols are commonly used in the scientific community to describe their respective stiffnesses; however,

since Abaqus CAE uses E/E_{nn}, $G1/E_{ss}$ and $G2/E_{tt}$ to define those same opening, sliding and tearing stiffnesses, those are the ones that will be used in the entirety of this dissertation.

In Section 2.3.2 of this very dissertation, it was commented that a QUADS failure criterion would be used to define the failure behaviour of the cohesive elements. For inputting all the required values in Abaqus, the papers by G. Wei et. al. [65] and by Z. Jiang et. al. [66] were used to extract the necessary numerical values.

Table 3.6: QUADS damage settings and cohesive element material properties [65]

Direction relative to local 1-direction	Normal (default)	
Tolerance	0.05 (default)	
Position	Centroid (default)	
Nominal stress, normal-only mode	t_n^0	35 MPa [65]
Nominal stress, first direction	t_s^0	65 MPa [65]
Nominal stress, second direction	t_t^0	65 MPa [65]

Table 3.7: QUADS damage evolution settings and cohesive element material properties [66]

Type	Energy	
Softening	Linear (default)	
Degradation	Maximum (default)	
Mixed mode behaviour	Benzeggagh-Keane	
Mode mix ratio	Energy (default)	
Power coefficient	2	
Normal mode fracture energy	G_{IC}	0.3 N/mm [66]
Shear mode fracture energy, first direction	G_{IIC}	0.8 N/mm [66]
Shear mode fracture energy, second direction	G_{IIIC}	0.8 N/mm [66]

The choice of the Benzeggah-Keane mixed mode behaviour, or BK in short, is due to the fact that delamination in composite laminates is usually produced by a combination of opening and shear separation rather than by a single pure fracture mode [31, 38]. In the present cohesive model, the shear fracture energies were defined as equal, $G_{IIC} = G_{IIIC} = 0.8\ \mathrm{N/mm}$ which makes the BK formulation suitable for describing the variation of fracture energy under mixed-mode loading [31]. A BK power coefficient of 2 was used because values in this range are commonly adopted for FRP/composite

delamination simulations and provide a gradual transition between Mode I and shear-dominated fracture behaviour [38, 66].

3.2.3. Assembly and part interaction definition

In the Abaqus/CAE numerical model, a general contact interaction was defined because Abaqus/Explicit simulations involving progressive damage, delamination and local deformation may lead to surfaces coming into contact during the analysis [28, 30]. This interaction provides a robust way of detecting possible contact across the model without manually defining every individual contact pair [30]. Therefore, general contact helps prevent unrealistic surface penetration and improves the stability of the contact definition during the explicit simulation [28].

A default contact interaction property was also created because contact detection alone only identifies which surfaces may interact, while the contact property defines the mechanical behaviour once contact occurs [49]. This property is necessary to specify the normal response between surfaces, preventing numerical penetration, and to define the tangential response, such as frictionless or frictional sliding [49]; although, since the material property data has been compiled with glass fibre-epoxy composite common values, the tangential and normal behaviour has been left undefined, relying on the default settings that the Abaqus CAE software has to perform the numerical simulations. In this way, the model has a consistent default behaviour for any surfaces included in the general contact interaction.

Finally, the cohesive and composite elements were connected using tie constraints because the cohesive layer was intended to represent a thin resin-rich interface initially bonded to the adjacent composite plies [31, 32, 63]. This method was selected because the composite and cohesive surfaces should transfer load as a continuous bonded region before damage develops, while the progressive separation is controlled by the cohesive traction–separation law rather than by the tie constraint itself [31, 32]. Therefore, the tie constraints ensure the initial mechanical connection between the composite shell elements and the cohesive elements, while the cohesive damage law governs the later degradation of the interface [31, 63].

When defining tie constraints between composite shell element surfaces and cohesive element surfaces, the composite shell element surface must be defined as the main surface, while the cohesive element surface must be defined as the secondary surface [49]. This choice is appropriate because the composite laminate is the main structural and higher stiffness region, whereas the cohesive layer is a thinner interfacial region whose surface is constrained to follow the adjacent laminate surface [49].

After defining the interactions between elements, each element must be manually placed in its desired position by the use of the translate instance and rotate instance functions in the "assembly" menu of the Abaqus CAE software interface.

3.2.4. Step definition

The numerical analyses were performed using a dynamic, explicit step with a total step time of 0.5s. This value was selected after several trial simulations, since it provided a suitable compromise between maintaining a quasi-static response and avoiding unnecessarily long computational times. In Abaqus/explicit, the stable time increment is controlled mainly by the element size, density and stiffness, so increasing the total step time generally increases the number of increments that must be solved [28]. However, the loading time cannot be reduced excessively, because applying the displacement too quickly may introduce inertial effects and prevent the simulation from remaining quasi-static [29]. Therefore, the selected step time of 0.5s was kept because the energy response showed that the kinetic energy remained small compared with the internal energy, which is one of the main checks recommended for quasi-static analyses performed with Abaqus/explicit [29, 42].

The field output requests were modified to record the variables required for post-processing, including stresses, strains, reaction forces, displacement fields and damage/fracture parameters. A custom output frequency was used to reduce unnecessary data storage during the initial part of the simulation, where no damage has yet to occur to the simulated specimen, while increasing the resolution of the results near the expected damage and failure region. During the first 0.2s, results were recorded every 0.01s, allowing this initial region to be analysed with a lower output density. After 0.2s, the output frequency was increased to every 0.001s, so that the resulting stress–strain, force–displacement and damage-evolution curves could be obtained with higher accuracy. This was necessary because writing output to the results database increases storage demand and computational cost, especially in Abaqus/Explicit simulations with many increments and limited hardware resources [28, 43].

For the history output, three separate groups of results were requested. The first history output group recorded the energy quantities of the complete system, including variables such as internal energy, kinetic energy, work, viscous dissipation and total energy, which were used to evaluate whether the simulation remained quasi-static and numerically stable [42, 44]. The second history output group recorded the reaction force at the fixed end of the specimen, allowing the tensile load transferred through the model to be obtained. The third history output group recorded the displacement at the loaded end of the

specimen, where the prescribed tensile displacement was applied. These force and displacement histories were then used to generate the numerical force–displacement response of the specimen and to compare the mechanical behaviour of the different joint configurations.

3.2.5. Boundary conditions

The boundary conditions of the numerical simulations were defined during the dynamic step 1, corresponding to the tensile loading step of the model. One end of the specimen was defined as "encastred", meaning that the translational degrees of freedom of the composite laminate at that end were constrained to prevent rigid-body motion. This boundary condition represents the fixed grip of the tensile test machine and provides the reaction force used to evaluate the mechanical response of the specimen. At the opposite end of the specimen, a displacement boundary condition was applied in the longitudinal direction of the specimen. This displacement represents the imposed movement of the tensile testing machine grip and allows the model to be loaded in a controlled manner. Using a displacement-controlled boundary condition is appropriate for this type of quasi-static tensile simulation because it allows the progressive development of damage and stiffness degradation to be followed throughout the analysis [29].

The boundary conditions were applied only to the composite shell elements, and not to the exposed ends of the cohesive elements. This is because the cohesive elements were not intended to represent the external gripping region of the specimen, but rather the thin interlaminar resin-rich interface between adjacent composite plies [31, 32, 63]. Their mechanical role is to transfer tractions between the connected composite surfaces and to allow damage initiation and degradation through the cohesive traction–separation law [31]. Therefore, applying the boundary conditions directly to the cohesive element ends would introduce an artificial load path through the cohesive layer and could over-constrain the interface, leading to unrealistic stresses or numerical problems [49]. For this reason, the tensile loading and the fixed support were defined on the composite shell elements, while the cohesive elements were connected to them through tie constraints and allowed to respond according to their cohesive damage law.

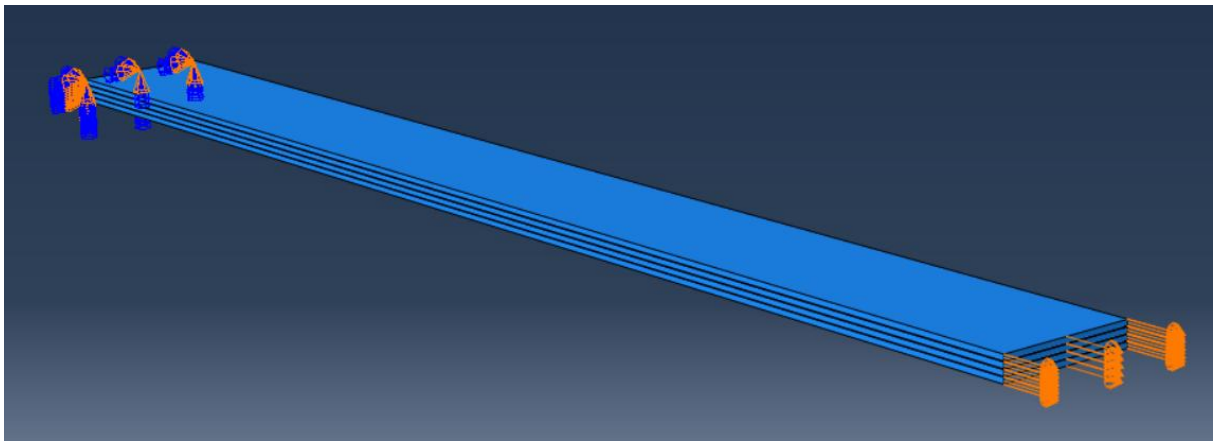


Figure 3.10: Boundary conditions defined

3.2.6. Mesh

Meshing strategy

The meshing strategy used in the numerical simulations was based on a structured hexahedral mesh for all the modelled parts. This strategy was suitable because the composite laminates and cohesive regions had a simple rectangular geometry, with straight edges and homogeneous thickness along their length and width. Abaqus documentation indicates that structured meshing is appropriate for simple three-dimensional regions and that structured three-dimensional meshes are formed by hexahedral elements [67]. The use of a structured mesh was also appropriate because the geometry did not contain complex curvature or irregular features that would require a free meshing approach. For long and thin rectangular regions, mapped/structured meshing can generate good-quality elements when the geometry is suitable [68]. This is relevant for the present specimen geometry, since the rectangular plan view and constant thickness allowed the mesh to follow the longitudinal, transverse and through-thickness directions regularly.

When assigning the element type in the "mesh" menu of the Abaqus CAE software interface, the explicit element library has to be selected for both composite and cohesive element types. The element type that should be assigned to the composite shell elements is the continuum shell option in the element type family list, where the cohesive option should be selected for the cohesive elements, resulting in the types of these elements being SC8R and COH3D8, respectively, exactly as it was done in Khalid et. al. [69] research. Abaqus also states that cohesive zones are normally discretised using a single layer of cohesive elements through the thickness, which supports the use of a regular cohesive layer between adjacent composite regions [49]. All other options were kept in the default position in this menu.

Because of the orthotropic nature of composites, it is also a good practice to define a material stacking direction in the "mesh" module for the continuum shell composite elements by using the assign stacking direction function. The side of the composite shell element that should be designated as top or bottom is always the larger face of the rectangular prism, as seen highlighted in blue in Figure 3.11.

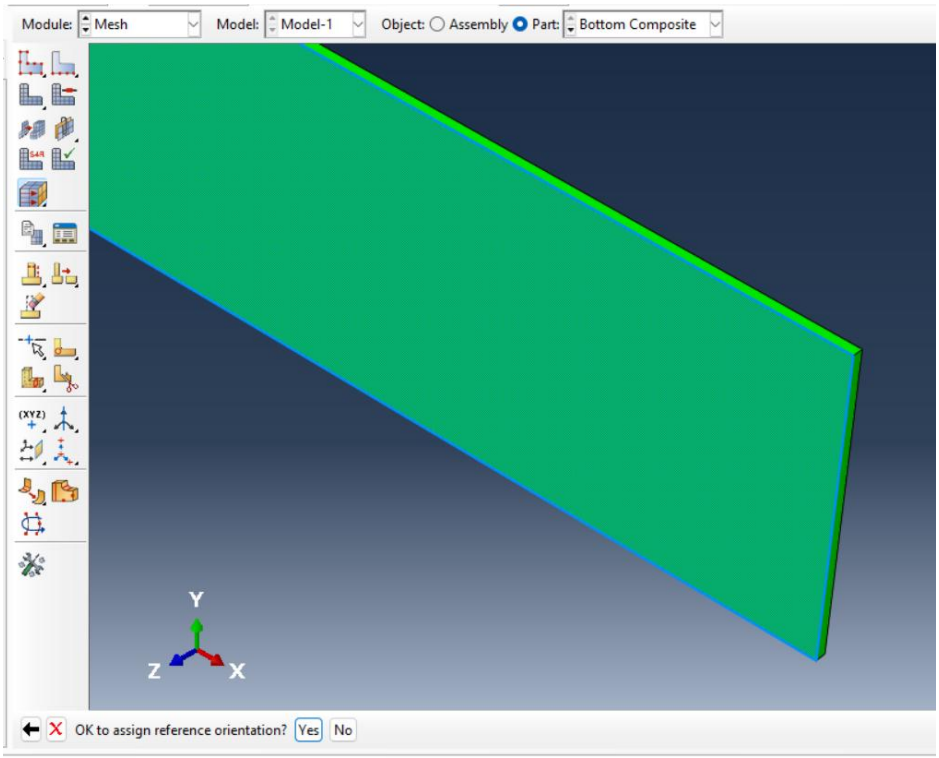


Figure 3.11: Composite continuum shell element rectangular prism face selection for assigning a correct staking direction in the “mesh” module of the Abaqus CAE numerical simulation software

Mesh sensitivity analysis

A mesh sensitivity analysis was performed to identify a suitable element size for the numerical simulations. This analysis was necessary because excessively coarse meshes can reduce the accuracy of the stress distribution, damage initiation and delamination prediction, while excessively fine meshes significantly increase the computational cost and simulation time. Therefore, different mesh sizes were compared to select the best compromise between numerical accuracy and computational efficiency. The final mesh size was chosen once further mesh refinement produced only limited changes in the results, while still maintaining reasonable analysis times for the Abaqus/Explicit simulations [27, 69]. For this task, a 4-layer composite glass fibre mat layered laminate was modelled in Abaqus CAE, as seen in Figure

3.12. The composite layers were kept continuous, as the results from the study were desired to be kept from being influenced by the minimum number of factors as possible.

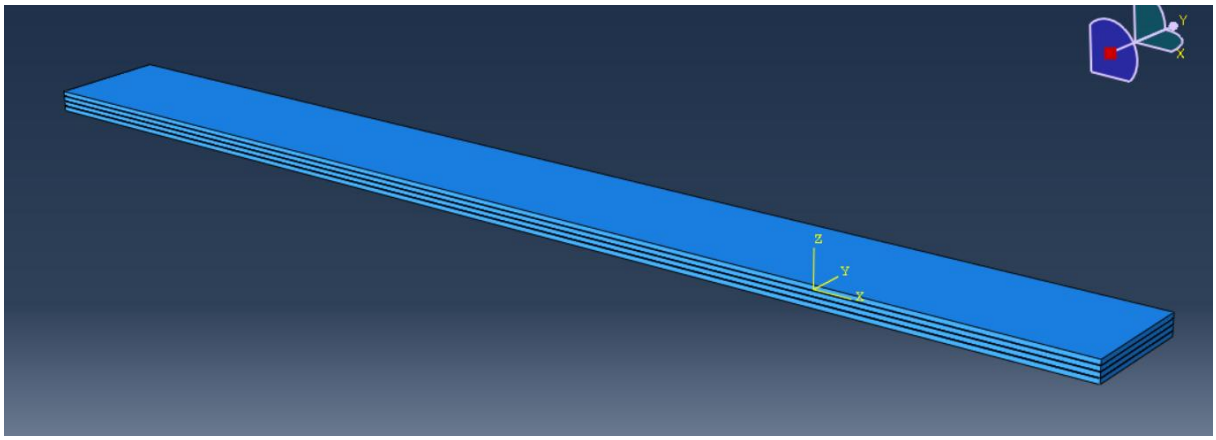


Figure 3.12: Laminate geometry for the numerical simulation of the mesh element size sensitivity analysis

Before carrying out the mesh sensitivity analysis in Abaqus/CAE, a manual calculation of the expected load–displacement response was performed. This calculation was used as a preliminary analytical reference to contrast the numerical results obtained from the simulations, particularly in the initial linear-elastic region of the tensile response. The composite material properties used in this calculation were estimated from the fibre and matrix contributions using rule-of-mixtures-based approaches [53, 57, 58]. By comparing the manually calculated stiffness with the numerical force–displacement curves, it was possible to verify whether the finite element model was producing a reasonable global mechanical response before analysing the influence of mesh size. However, the manual calculation was only used as a simplified reference, since it does not capture local stress concentrations, progressive damage, cohesive degradation or delamination, which are represented in the Abaqus model through the composite damage and cohesive zone formulations [24, 31, 40]. The calculation method was derived from the international standard test method for tensile properties of polymer matrix composite materials (ASTM D3039/D3039M-17(2025)) [70].

Since each mat glass fibre mat is composed of 0° and 90° fibre orientated regions in equal measure, with both elastic moduli E_1 and E_2 and both longitudinal and transverse tensile strengths, X_T and Y_T respectively, known, the first step in the manual calculation of the load-displacement curve is to work out the failure strains for each fibre orientation region, namely $\varepsilon_{f,0^\circ}$ and $\varepsilon_{f,90^\circ}$.

$$\varepsilon_{f,0^\circ} = \frac{X_T}{E_1} = \frac{1060\ MPa}{44656\ MPa} = 0.0237 \rightarrow \varepsilon_{f,0^\circ} = 2.37\%\ strain \tag{3.10}$$

$$\varepsilon_{f,90^\circ} = \frac{Y_T}{E_2} = \frac{31\ MPa}{7149.69\ MPa} = 0.00434 \rightarrow \varepsilon_{f,90^\circ} = 0.434\%\ strain \tag{3.11}$$

Translating this failure points into elongation of the laminate, $\Delta l_{f,0^\circ}$ and $\Delta l_{f,90^\circ}$; being achieved by multiplying this failure strain by the initial length of the laminate, $l_{0,laminate}$, the results obtained are:

$$\Delta l_{f,0^\circ} = \varepsilon_{f,0^\circ} \cdot l_{0,laminate} = 0.0237 \cdot 250\ \text{mm} \rightarrow \Delta l_{f,0^\circ} = 5.93\ \text{mm} \tag{3.12}$$

$$\Delta l_{f,90^\circ} = \varepsilon_{f,90^\circ} \cdot l_{0,laminate} = 0.00434 \cdot 250\ \text{mm} \rightarrow \Delta l_{f,90^\circ} = 1.08\ \text{mm} \tag{3.13}$$

As for the calculation of the load at each point of fibre orientation region failure, the calculation procedure varies whether the elongation is less or more than the failure elongation of the 90° fibre orientation region, $\Delta l_{f,90^\circ}$; as below this threshold, both regions contribute to the resistance of the laminate, whereas if the elongation is above this value, only the 0° fibre orientated region contributes towards the resistance of the laminate.

The calculation of the load that the laminate can withstand at the point of overall laminate failure, $F_{f,0^\circ}$, has been calculated in Eq. (3.14), with the procedure being the multiplication of the longitudinal tensile strength by the combination of the cross-sectional area of all the layers of 0° fibre-oriented regions of the laminate.

$$F_{f,0^\circ} = X_T \cdot \left(w_{1\ ply,0^\circ} \cdot t_{1\ ply,0^\circ}\right) \cdot n_{plies} = \\ = 1060\ \text{MPa} \cdot (25\ \text{mm} \cdot 0.5005\ \text{mm}) \cdot 4 \rightarrow F_{f,0^\circ} = 53053\ \text{N} \tag{3.14}$$

where $w_{1\ ply,0^\circ}$ is the width of a 0° glass fibre orientated region of a single layer of glass fibre mat, $t_{1\ ply,0^\circ}$ references the thickness of that same region, and n_{plies} the number of glass fibre mat layers in a given laminate.

As for the load calculation at the point of failure of the 90° fibre-oriented regions, the combined tensile strength of all the regions must be calculated at this point. For this, the tensile strength of the 0° fibre-oriented plies must be calculated at the point of failure of the 90° fibre orientated plies by multiplying the elastic modulus E_1 by the strain at this point of failure $\varepsilon_{f,90^\circ}$; and then adding the transverse strength of the composite material Y_T to the result of the previously described multiplication, to account for the contribution of the 90° fibre orientated regions.

$$XY_T = \left(\varepsilon_{f,90^\circ} \cdot E_1\right) + Y_T = (0.00434 \cdot 44656\ \text{MPa}) + 31\ \text{MPa} \rightarrow \\ \rightarrow XY_T = 224.6405\ \text{MPa} \tag{3.15}$$

Then, the load experienced by the laminate at the point of failure of the 90° fibre-oriented regions, $F_{f,90°}$, can be worked out by inserting the previously calculated combined tensile strength XY_T to an equation similar to Eq. (3.14).

$$F_{f,90°} = XY_T \cdot \left(w_{1\ ply,90°} \cdot t_{1\ ply,90°}\right) \cdot n_{plies} =$$
$$= 224.6405 \cdot (25\ \text{mm} \cdot 0.5005\ \text{mm}) \cdot 4 \rightarrow F_{f,90°} = 11243.25\ \text{N} \quad (3.16)$$

where $w_{1\ ply,90°}$ is the width of a 90° glass fibre orientated region of a single layer of glass fibre mat, $t_{1\ ply,90°}$ references the thickness of that same region, and n_{plies} the number of glass fibre mat layers in a given laminate.

The results of the previous calculation procedure can be observed in the load-displacement curve shown in Figure 3.13.

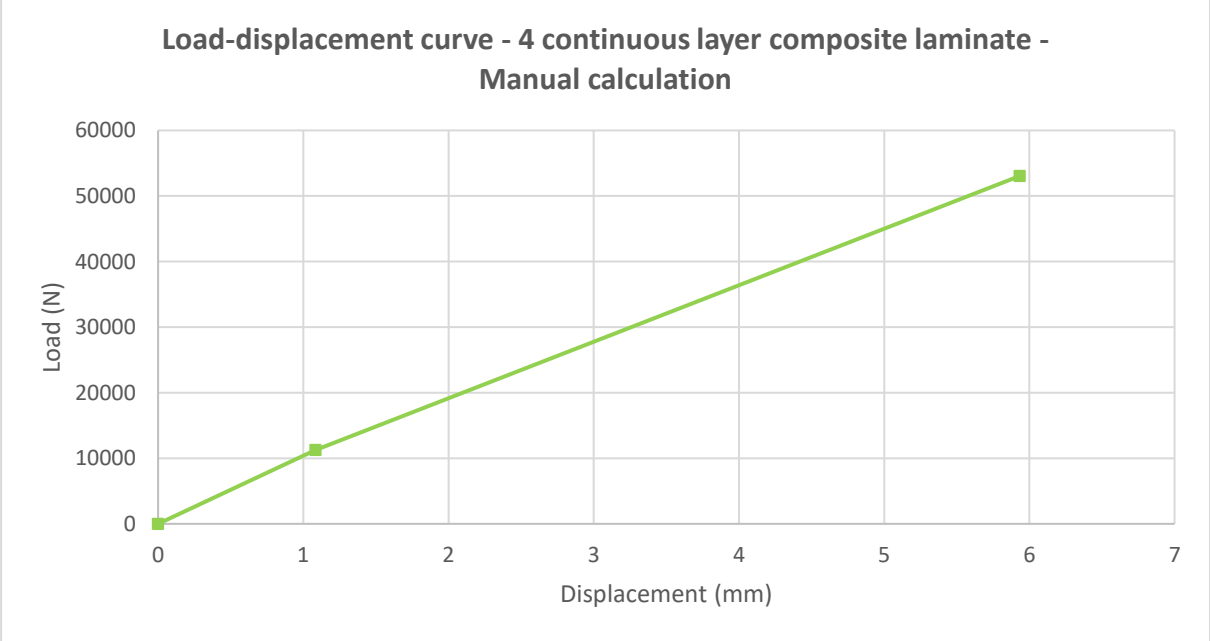


Figure 3.13: Manually calculated load-displacement curve for a continuous 4-layer composite laminate

As can be seen in the previous figure, the calculated evolution of the load versus the displacement in the elastic region up to the point of theoretical laminate failure of a 4-layer continuous composite laminate can be observed. Note that the slope of the curve changes after the point of failure of the 90° fibre-oriented regions, as those regions no longer have an influence on the overall strength of the region, thus making the slope less severe.

For performing the numerical mesh sensitivity study, simulations were run with descending mesh element size order, starting with a fairly large 7mm element size and finishing up with a 3mm element size; as this latter element size is the biggest one that followed the linear elastic behaviour without deviation, as seen in Figure 3.14.

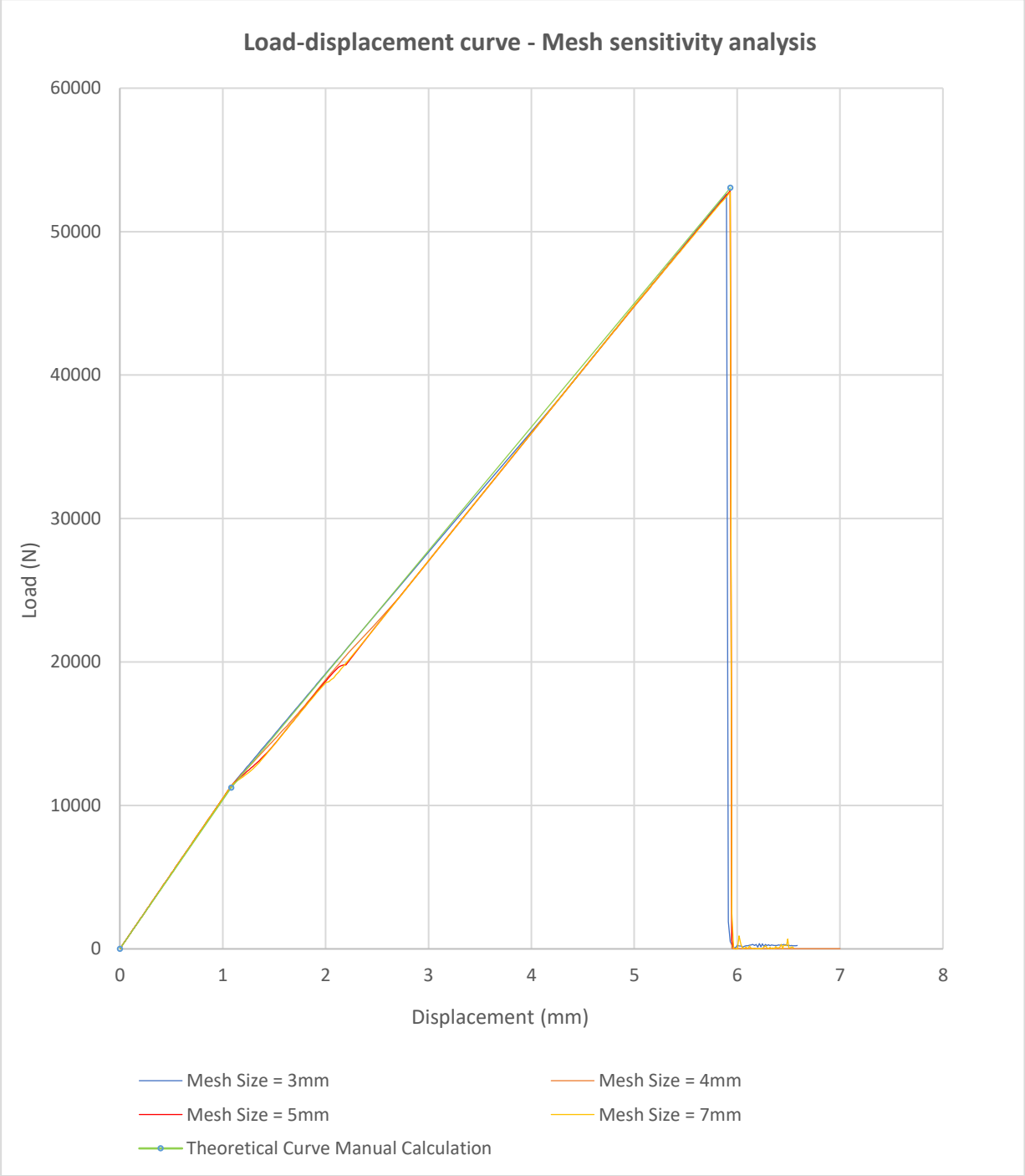


Figure 3.14: Load-displacement curve of the mesh sensitivity study

It can be observed that the curve follows the trajectory more closely to the calculated theoretical one in the blue line, without any instability, corresponding to the evolution experienced by the simulation employing mesh elements of 3mm in size; whereas all the other ones deviate between the 1 and 4mm displacement marks, later converging to the theoretical curve progression. It must be mentioned that all mesh size simulations achieve a composite failure point that is very close to the theoretical tensile failure point, further corroborating that the model is stable and can predict and simulate the behaviour of the composite material with an acceptable degree of fidelity.

The simulation times for each can be seen in Table 3.8. As can be seen, the simulations with smaller mesh elements require considerably more time to be computed. With the objective of reducing simulation times, a higher result recording frequency was requested in the critical moments of the simulation, namely around the point of failure of the 90° fibre-oriented regions and the overall failure of the laminate.

Table 3.8: Simulation times for each numerical simulation of the mesh sensitivity analysis

Mesh element size	**3mm**	**4mm**	**5mm**	**7mm**
Elapsed Time	5.45 hours	3.91 hours	2.75 hours	1.92 hours

Since the accuracy of the results is wanted to be as high as possible, but also maintaining the simulation runtimes in check, a compromise was worked out for the simulations that would study the performance of the ply joint configurations, this being on defining a fine 3mm element sized mesh on all the elements in the regions that are in proximity to the ply discontinuities, while defining a coarser mesh in the areas of the laminate that are far away from the ply joint; as seen in Figure 3.15. As a visual aid, two red lines have been added to indicate the frontier between meshing areas, where the ply joint is located between them.

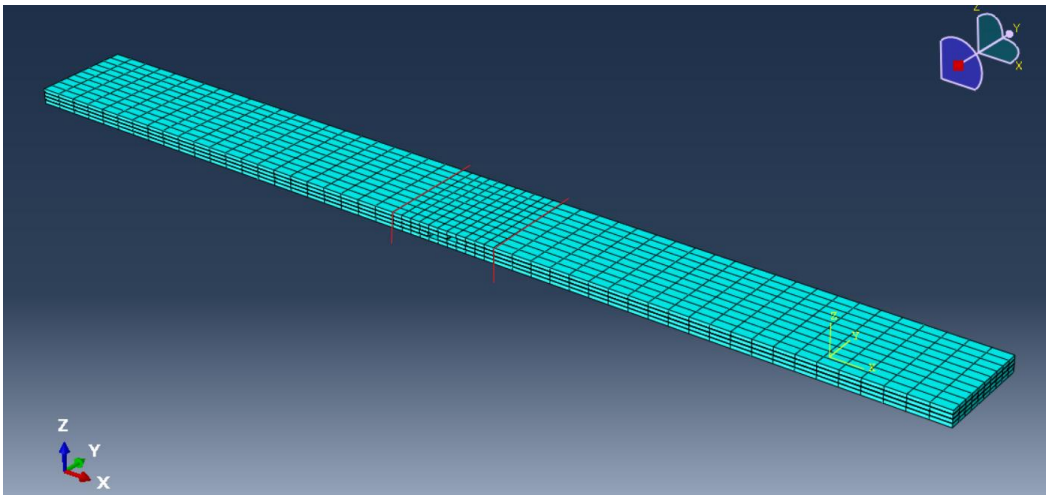


Figure 3.15: Example of meshing strategy for a simulated test ply-joint laminate

The mesh element sizes were defined as 2.5mm for the fine-meshed sections, and 5mm for the coarse-meshed sections. The difference in mesh size in the same element was achieved by creating a face partition followed by an extrusion operation of such partition when creating the geometry of each composite shell and cohesive element. For all numerical simulations, the frontier between the different meshed areas was placed at 10mm away from the end of the discontinuity that was furthest away from the midpoint of the laminate.

The meshes of the different parts were not forced to have coincident nodes at their interfaces because the connection between the composite shell elements and the cohesive elements was defined using surface-based tie constraints rather than shared nodes. Abaqus allows this approach when the neighbouring parts do not have matched meshes, since the cohesive layer surfaces can be tied to the surrounding composite surfaces to ensure load transfer across the interface [49]. Therefore, node-to-node alignment was not strictly necessary, provided that the tied surfaces were correctly defined, with the composite laminate surface acting as the main surface and the cohesive surface as the secondary surface. This approach also allowed each part to be meshed according to its own geometric and numerical requirements while maintaining the mechanical connection between layers. However, the absence of matching nodes still requires a mesh sensitivity analysis, since the mesh size and surface discretisation can influence stress transfer, damage initiation and delamination predictions [27, 69].

3.3. Design of ply end-to-end ply joint configurations

In this section of the dissertation, the ply joint configuration geometries will be explained; all in accordance with the ISO 527-4:2023 norm (see Annex A). Since the more favourable ply joint configurations will be tested in a tensile test bench, it was decided that, for aiding manufacturability, all ply joints were to be designed with two outer continuous glass fibre mat layers, one on each side of the laminate; with the discontinuous layers being placed between them. The purpose of having the continuous outer layers is to provide a stable platform on which the discontinuous layers can be encapsulated, which will be especially important during the completely manual vacuum infusion manufacturing process.

3.3.1. Critical parameter study of ply end-to-end joints

For the carrying out of this study, a simple ply joint configuration was preferred to better isolate the effects of varying the critical parameters that govern the behaviour of end-to-end ply joints. It is for this reason that the laminate geometry was limited to 4 layers of glass fibre composite mat, where the composite layer discontinuity disposition is shown in Figure 3.16. This laminate geometry allows for fast and easy modification for varying the discontinuity size and distance between them. Moreover, the mesh size region frontier can be seen, represented by the two vertical lines that traverse the laminate at either side of both composite layer discontinuities.



Figure 3.16: Ply joint discontinuity disposition utilised for performing the end-to-end ply joint critical parameter study

In addition to this, a ply joint configuration was also numerically tested where both discontinuity voids were placed on top of each other, creating a two-layer-thick discontinuity, as seen in Figure 3.17.

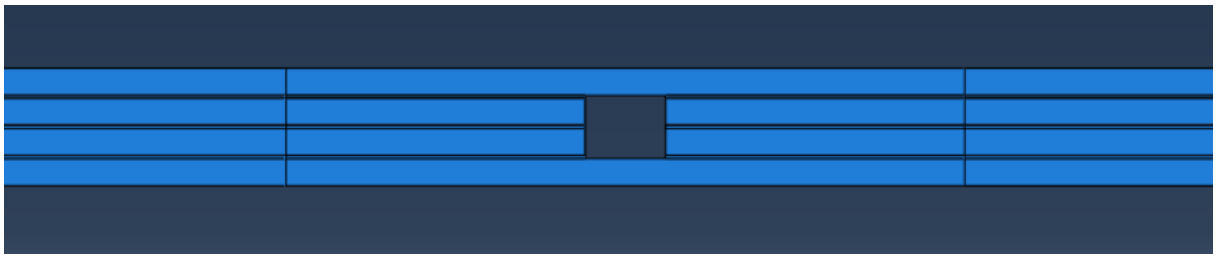


Figure 3.17: Ply joint discontinuity disposition where the voids have been placed aligned on top of each other

3.3.2. Possible complex configurations

To study the behaviour of more complex end-to-end ply joint configurations, inspiration was taken from Ahamed's research [19] in various discontinuity placement amongst the thickness of composite laminates, where it is concluded that the three interleaved ply joint configurations that offer the best results when tested in tensile conditions were the ones that will be presented in this section of this dissertation.

For determining the maximum number of glass fibre mat layers, the ISO 527-4:2023 norm (see Annex A) states that a maximum laminate thickness must be under 10mm. As the thickness of the glass fibre waste mats that have been utilised in this dissertation is equal to 1.01mm, that limits the maximum number of composite layers to 8. It must also be mentioned that the distances between the voids and the void sizes are always homogeneous.

Asymmetric interleafed misaligned scarf ply joint configuration

As can be seen in Figure 3.18, the asymmetric interleafed misaligned scarf ply configuration void disposition can be observed, where the red line represents the mid-point plane of the laminate and the yellow line represents the symmetry plane of the composite mat layup order.

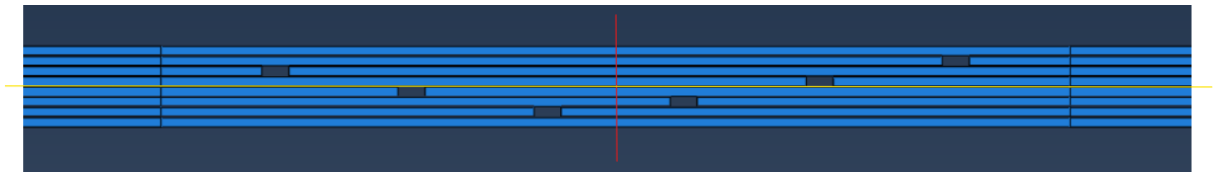


Figure 3.18: Asymmetric interleafed misaligned scarf ply configuration

The main distinctive feature of this ply joint configuration is that the composite material discontinuity voids form a V-shaped pattern along the thickness of the laminate, thus explaining the asymmetric nature of this void disposition in reference to the ply stacking symmetry plane.

Symmetric interleafed aligned scarf ply joint configuration

For this complex ply joint configuration, the material discontinuity voids should be placed forming a ◊-shaped pattern along the thickness of the laminate, which is why the symmetric label is used for describing this ply joint configuration, as it can be seen in Figure 3.19; even though strict symmetry was not followed to avoid the combination of two voids at the symmetry plane. The composite material discontinuity voids have been placed aligned through-laminate-thickness-wise.

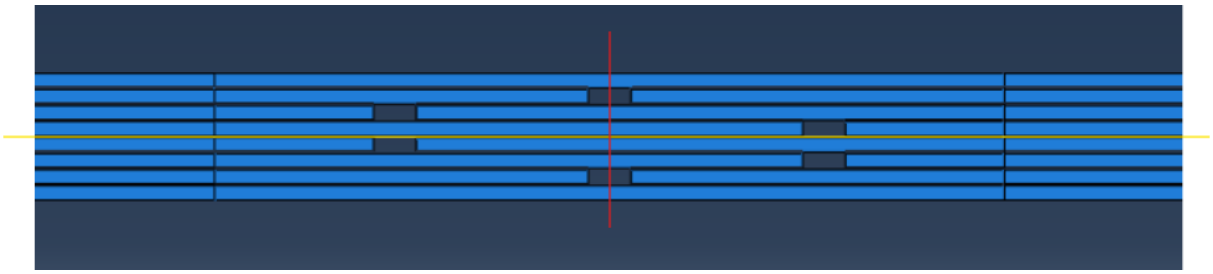


Figure 3.19: Symmetric interleafed aligned scarf ply joint configuration

Symmetric interleafed misaligned scarf ply joint configuration

This ply joint configuration is a variant of the previous one, where, in this one, the void placement makes sure that no through-laminate-thickness alignment of the voids happens.

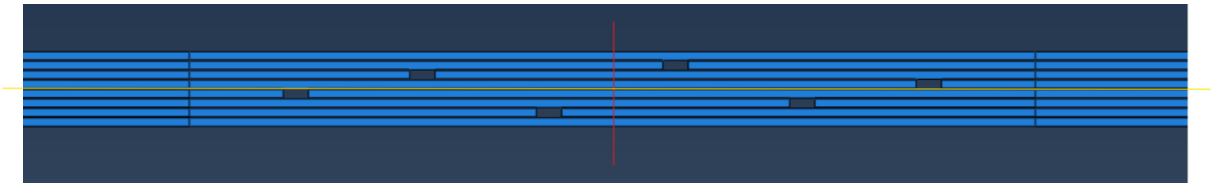


Figure 3.20: Symmetric interleafed misaligned scarf ply joint configuration

3.4. Numerical simulation results

All the numerical simulation result datapoints extracted from the Abaqus CAE software have been obtained by generating the load-displacement curves for each of the simulations. Then, to generate the engineering stress-strain curves of that same numerical simulation, the following calculation was performed.

First, the tensile load was obtained from the reaction force in the loading direction, which, in the cases analysed, the relevant tensile force corresponded to the RF_1 component, since the tensile displacement was applied in the longitudinal direction of the specimen. For obtaining it, all the absolute reaction force values from all the nodes located on the constrained or loaded edge were summed in order to obtain the total applied load. The engineering stress, σ_{eng}, was then calculated by dividing this force by the original total cross-sectional area of the specimen, referred to as $A_{0,coss-section,total}$; which also included the thickness added by the three cohesive element layers, which represent the resin rich areas in between the glass fibre mat layers that would be found in a composite laminate produced by vacuum infusion.

$$\sigma_{eng} = \frac{|RF_1|}{A_{0,coss-section,total}} \tag{3.17}$$

where:

$$A_{0,coss-section,total} = 4 \cdot \left(w_{1\,ply} \cdot t_{1\,ply}\right) + 3 \cdot \left(w_{1\,coh.\ layer} \cdot t_{1\,coh.\ layer}\right) =$$
$$= 4 * (25\ \text{mm} \cdot 1.01\ \text{mm}) + 3 \cdot (25\ \text{mm} \cdot 0.1\ \text{mm}) \rightarrow$$
$$\rightarrow A_{0,coss-section,total} = 108.5\ \text{mm}^2 \tag{3.18}$$

with $w_{1\,ply}$ referencing the total width of a single layer of glass fibre mat and $w_{1\,coh.\ layer}$ doing the same for a single cohesive element layer; and $t_{1\,ply}$ represents the thickness of a single layer of glass fibre mat, with $t_{1\,coh.\ layer}$ doing the same for a single cohesive element layer.

The engineering strain, ε_{eng}, was calculated by dividing the applied displacement, U_1 , by the original gauge length of the specimen, $l_{0,total}$. The applied displacement was obtained by extracting the average displacement of the nodes of the specimen where the displacement boundary condition was applied.

$$\varepsilon_{eng} = \frac{|U_1|}{l_{0,total}} \tag{3.19}$$

where:

$$l_{0,total} = 250\ \text{mm} \tag{3.20}$$

These definitions are consistent with the standard tensile testing methodology used for polymer matrix composite materials, where tensile properties are derived from force, specimen dimensions, and strain measurements [70], Since the conversion is based on the global reaction force and applied displacement, the resulting curve represents the apparent engineering stress–strain response of the simulated specimen or joint configuration, rather than the local stress–strain response of an individual ply. The linear elastic interpretation of the response before damage initiation is supported by the orthotropic lamina stress–strain relations commonly used in composite mechanics [71].

It is also pertinent to mention that for determining the values of both the sizes of the matrix voids in between the glass fibre layer terminations and the distances between these voids, multiples of the thickness of a single glass fibre mat layer were used. In the following figures in this section of this dissertation, the void size will be referred to as "pocket", where also the distance between these matrix voids will be referred to as "gap"; as seen in Figure 3.21.

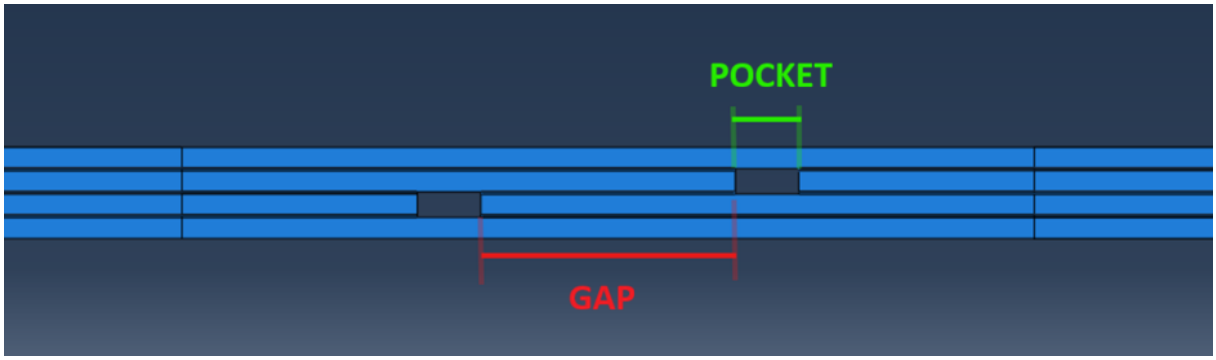


Figure 3.21: "Gap" and "Pocket" measurements on the ply joint discontinuity disposition utilised for performing the end-to-end ply joint critical parameter study

The nomenclature of these measurements that will be referenced from now on can be seen in Figure 3.22; where l_{gap} refers to the length of the gap between resin rich pockets, l_{pocket} refers to the length of the resin pocket itself, and lastly, $t_{1\ ply}$ signifies the total thickness of a glass fibre mat layer.

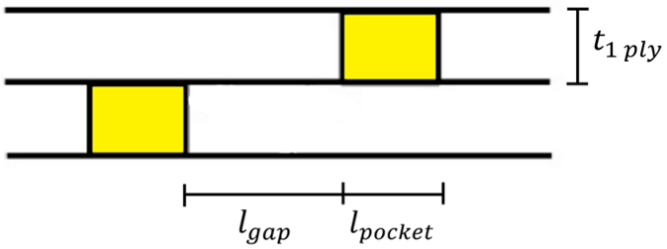


Figure 3.22: Nomenclature used for the gap and pocket lengths and thickness of a single layer of glass fibre mat

3.4.1. Study of end-to-end joint configuration critical parameters

Effect of resin pocket size study

Making use of the ply joint geometry shown previously in Figure 3.16, firstly, the effect of the size of the matrix void or gap between glass fibre mat layer terminations was studied. For this, a constant gap of 4

times the thickness of a layer of glass fibre mat or 4.04 mm, was defined as a benchmark value; varying the pocket size between 1 and 5 times the thickness of a glass fibre mat layer, or 1.01mm and 5.05mm. After performing three separate simulations, the load-displacement and engineering stress-strain curves seen in Figure 3.23 and Figure 3.24Figure 3.23: Load-displacement curve of the effect of pocket size variation study were obtained:

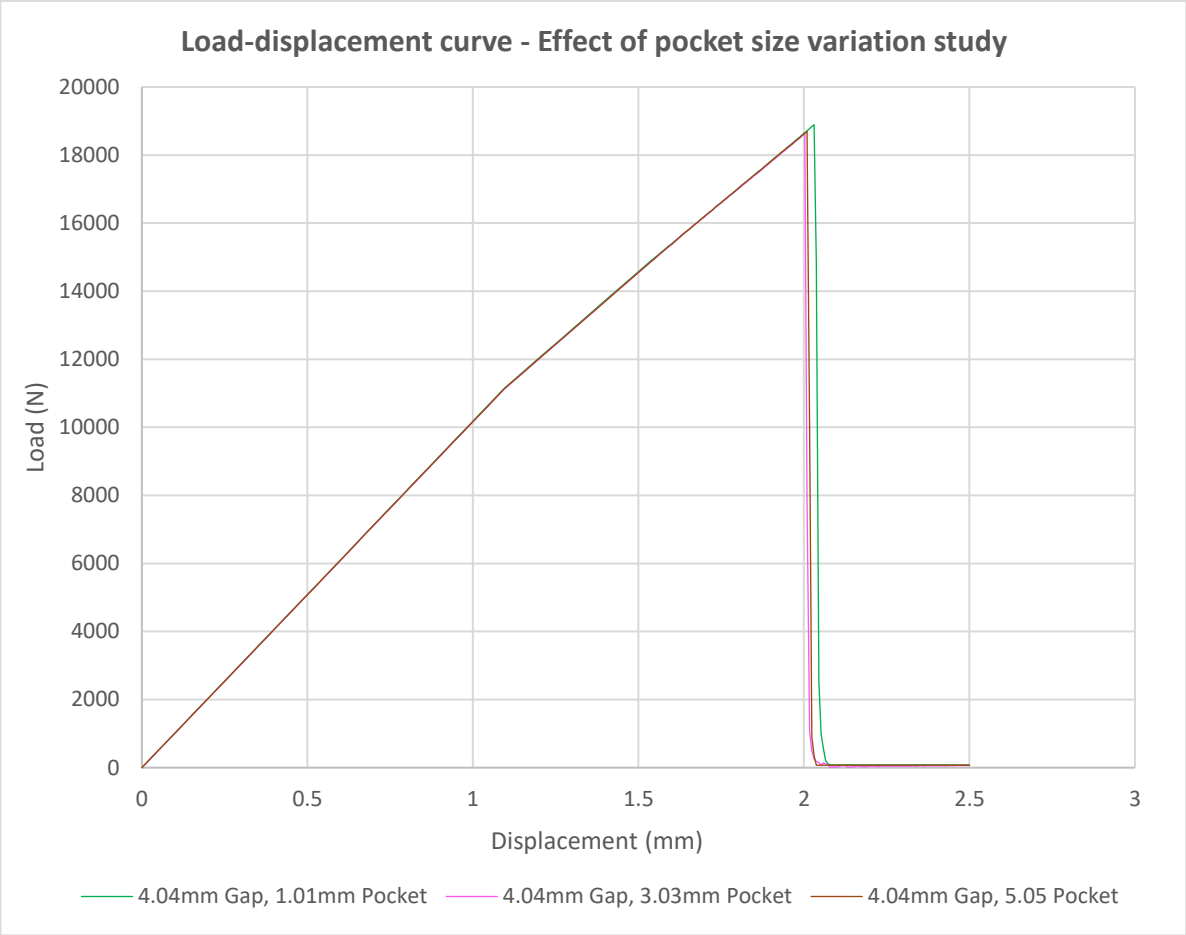


Figure 3.23: Load-displacement curve of the effect of pocket size variation study

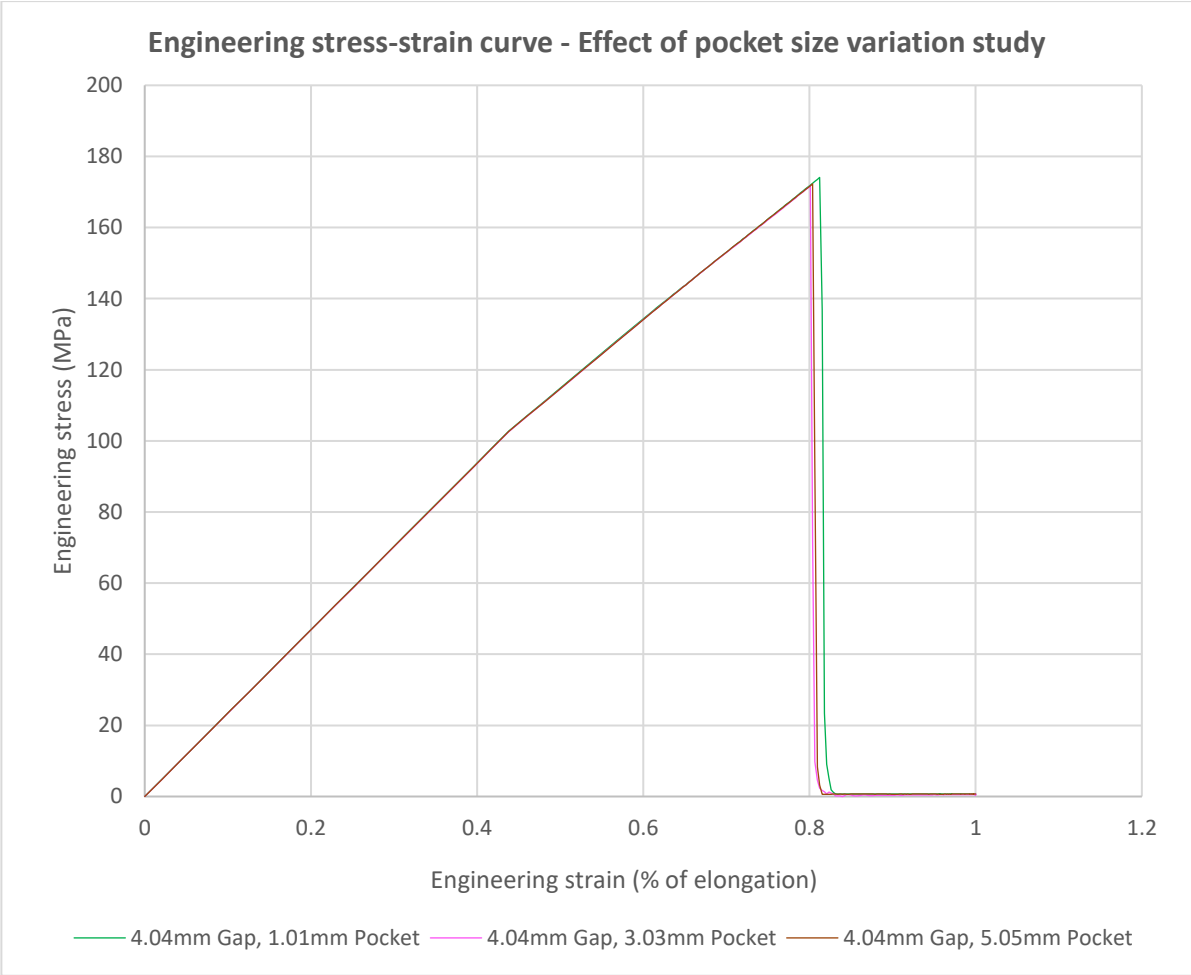


Figure 3.24: Engineering stress-strain curve of the effect of pocket size variation study

As can be observed in Figure 3.23 and Figure 3.24, all three numerical simulations indicate that the size of the resin-rich pocket found in the glass fibre layer discontinuities has a very small effect on the overall performance of the laminate, only presenting a very slight variation in the results obtained between the worst-performing and best-performing variant, as seen in Table 3.9.

Table 3.9: Performance analysis chart of the effect of pocket size study

Resin pocket aspect ratio $l_{pocket}/t_{1\,ply}$ (mm/mm)	l_{pocket}	**Maximum load**	**Displacement at maximum load**	**Maximum stress**	**Strain at maximum stress**
1	1.01 mm	18889 N	2.03 mm	174.096 MPa	0.812 %
3	3.03 mm	18627 N	2.00 mm	171.679 MPa	0.801 %
5	5.05 mm	18693 N	2.01 mm	172.291 MPa	0.804 %
Coefficient of variation		0.593 %	0.619 %	0.594 %	0.576 %

In addition to this data analysis, stress concentration ratios were used in this work to evaluate how the ply joint geometry affects the local stress state around the resin-rich regions and ply discontinuities. In particular, the ratios between the peak local stresses and the engineering laminate stress allow the severity of the stress concentration to be compared between different configurations independently of the absolute applied load. This is useful because the engineering stress represents the average tensile stress applied to the specimen [70], while the peak stresses indicate the local amplification produced by geometric discontinuities. Similar approaches are relevant in ply drop-off and discontinuous laminate studies, where ply terminations introduce local stress concentrations that can reduce the strength of the laminate [72, 73].

The ratio between the peak longitudinal stress and the engineering stress, $\sigma_{11}^{peak}/\sigma_{eng}$, was used as an indicator of how strongly the load-carrying plies are locally stressed near the discontinuity. A high value of this ratio shows that the axial load is not being transferred smoothly and that the fibres or matrix close to the resin-rich zone may experience a higher stress than the nominal laminate stress. This parameter is therefore useful for understanding the disturbance of the tensile load path caused by the ply discontinuity. This interpretation is supported by studies of laminates with ply drops, where resin pockets and ply terminations were shown to affect tensile behaviour, load transfer and local stress concentration zones [73, 74].

However, for the present models, the most relevant parameters for cohesive failure are the ratios involving the interlaminar stresses, such as $\tau_{13}^{peak}/\sigma_{eng}$, $\tau_{23}^{peak}/\sigma_{eng}$, and $\sigma_{33}^{peak}/\sigma_{eng}$; these being the ratio between the two components of interlaminar shear with the engineering stress and the normal opening/peel stress with the engineering stress respectively. These stresses are more directly related to the loading of the cohesive element, since cohesive elements transfer load through normal and shear tractions across the interface [31, 75]. Therefore, high interlaminar shear or peel stresses around the resin-rich regions indicate a greater tendency for cohesive damage initiation and delamination. This is especially important in the present study because the main failure mechanism occurs in the cohesive element located between resin-rich voids created by ply discontinuities. Previous studies on ply drop-off regions have also identified interlaminar stresses as a major cause of delamination and have shown that stress concentrations are highest near the drop-off region [76].

This approach is consistent with the work of Ahamed [19], where peak stresses around resin pockets and ply terminations were normalised by a far-field applied stress to evaluate the severity of local stress concentrations. In the present work, the engineering laminate stress was used in a similar way as a global

reference stress. Nevertheless, the cohesive failure assessment should not rely only on one stress component. Since the Abaqus cohesive damage initiation criterion is based on the combined effect of normal and shear tractions, the direct evaluation of cohesive parameters such as QUADSCRT and SDEG is also necessary [31, 37, 75]; with QUADSCRT measuring the value of the quadratic nominal stress damage initiation criterion for the cohesive element indicating when the combined normal and shear tractions become critical, and SDEG measures the scalar stiffness degradation of the cohesive element after damage has initiated. [31, 37]. The normalised stress ratios are therefore used as comparative indicators of stress concentration, while the cohesive damage variables are used to confirm whether the local stress state is sufficient to initiate or propagate cohesive failure.

For the longitudinal stress ratio, the maximum positive value of σ_{11} was used in order to evaluate tensile stress concentration in the load-carrying plies. This is appropriate because the specimen is loaded in tension, and ply discontinuities are known to generate local stress concentrations around the termination region [72, 73]. In contrast, the interlaminar shear stress ratios were calculated using the highest absolute values of τ_{13} and τ_{23}, since the sign of the shear stress only indicates the direction of sliding, while its magnitude controls the severity of cohesive shear loading. This is consistent with the quadratic nominal stress formulation used for cohesive damage initiation, where the two shear traction components contribute through squared stress ratios [31, 37, 75]. For the normal cohesive stress, only positive σ_{33} values were considered relevant to opening or peel loading, since negative values correspond to compressive closing of the interface. In the Abaqus cohesive damage formulation, the normal traction is treated using Macaulay brackets ($\langle\ \rangle$), meaning that compressive normal stress does not contribute to cohesive damage initiation [31, 37, 75].

Table 3.10: Peak stress values recorded in all three numerical simulations performed for the effect of pocket size study

Resin pocket aspect ratio $l_{pocket}/t_{1\,ply}$ (mm/mm)	l_{pocket}	σ_{11}^{peak}	τ_{13}^{peak}	τ_{23}^{peak}	σ_{33}^{peak}
1	1.01 mm	613.909 MPa	44.852 MPa	17.279 MPa	11.237 MPa
3	3.03 mm	588.218 MPa	44.679 MPa	16.232 MPa	10.588 MPa
5	5.05 mm	559.218 MPa	44.034 MPa	15.264 MPa	10.406 MPa

Table 3.11: Stress ratios of all three numerical simulations performed for the effect of pocket size study

Resin pocket aspect ratio $l_{pocket}/t_{1\,ply}$ (mm/mm)		$\sigma_{11}^{peak}/\sigma_{eng}$	$\tau_{13}^{peak}/\sigma_{eng}$	$\tau_{23}^{peak}/\sigma_{eng}$	$\sigma_{33}^{peak}/\sigma_{eng}$
1	1.01 mm	3.526	0.257	0.099	0.064
3	3.03 mm	3.426	0.26	0.094	0.061
5	5.05 mm	3.245	0.255	0.088	0.06
Coefficient of variation		3.421 %	0.798 %	4.801 %	2.756 %

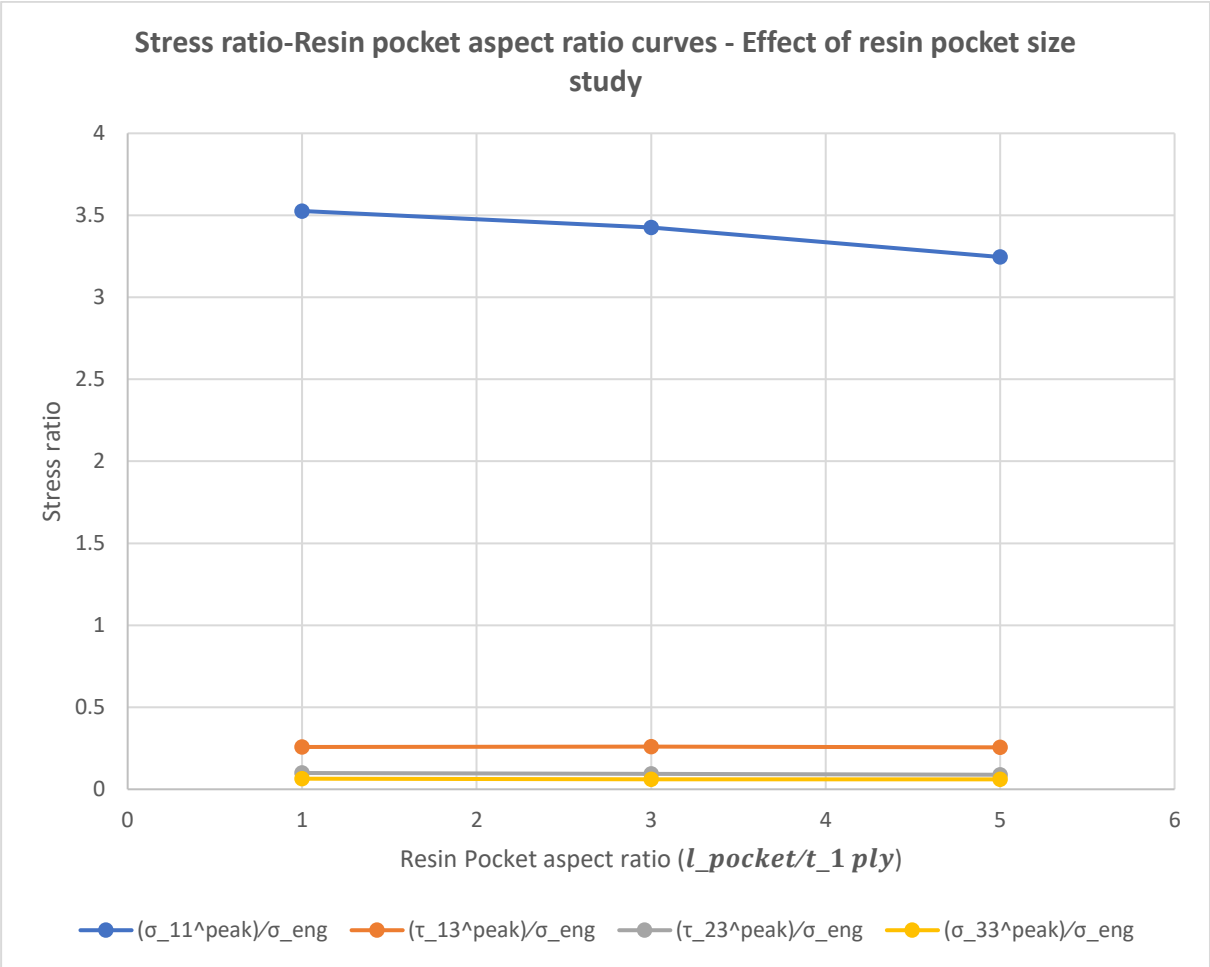


Figure 3.25: Evolution of the stress ratios vs. the resin pocket aspect ratio in all three numerical simulations performed for the effect of pocket size study

After analysing all the results found in Table 3.10, Table 3.11 and Figure 3.25, it can be concluded that increasing the resin pocket aspect ratio produces a reduction in the longitudinal stress concentration ratio $\sigma_{11}^{peak}/\sigma_{eng}$, second interlaminar shear stress concentration ratio $\tau_{23}^{peak}/\sigma_{eng}$ and normal opening/peel stress concentration ratio $\sigma_{33}^{peak}/\sigma_{eng}$; while the first interlaminar shear stress concentration ratio $\tau_{13}^{peak}/\sigma_{eng}$ stays almost constant among all three cases. Since the magnitude of the values indicates that this latter interlaminar stress ratio is the dominant one, it can be concluded that increasing the pocket length reduces some local stress concentrations, but it does not significantly modify the main shear loading component acting on the cohesive element.

As for the cause of failure of the laminate, in all three numerical simulations, the middle cohesive element that sits in the symmetry plane of the laminate between both resin pockets is always the first cohesive region to fail. This phenomenon makes perfect sense, as this region is situated between the stress concentration regions generated by the resin; and if the distance between the resin-rich pockets is not sufficiently large, the otherwise individual pocket stress concentration regions may interact, increasing the overall stresses experienced between the resin-rich pockets [19].

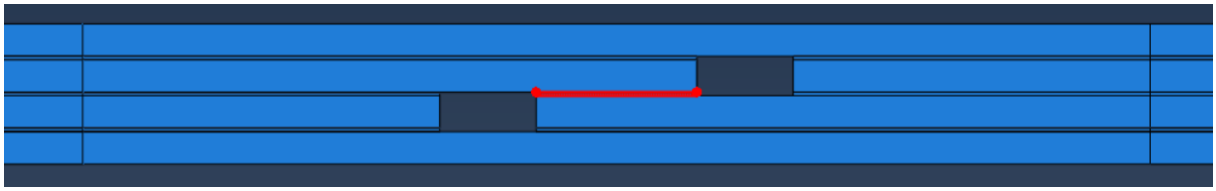


Figure 3.26: Location of the middle cohesive element

In Figure 3.27 and Figure 3.28, the progression of the cohesive failure analysis parameters can be analysed for the average state among the geometries of the middle cohesive element.

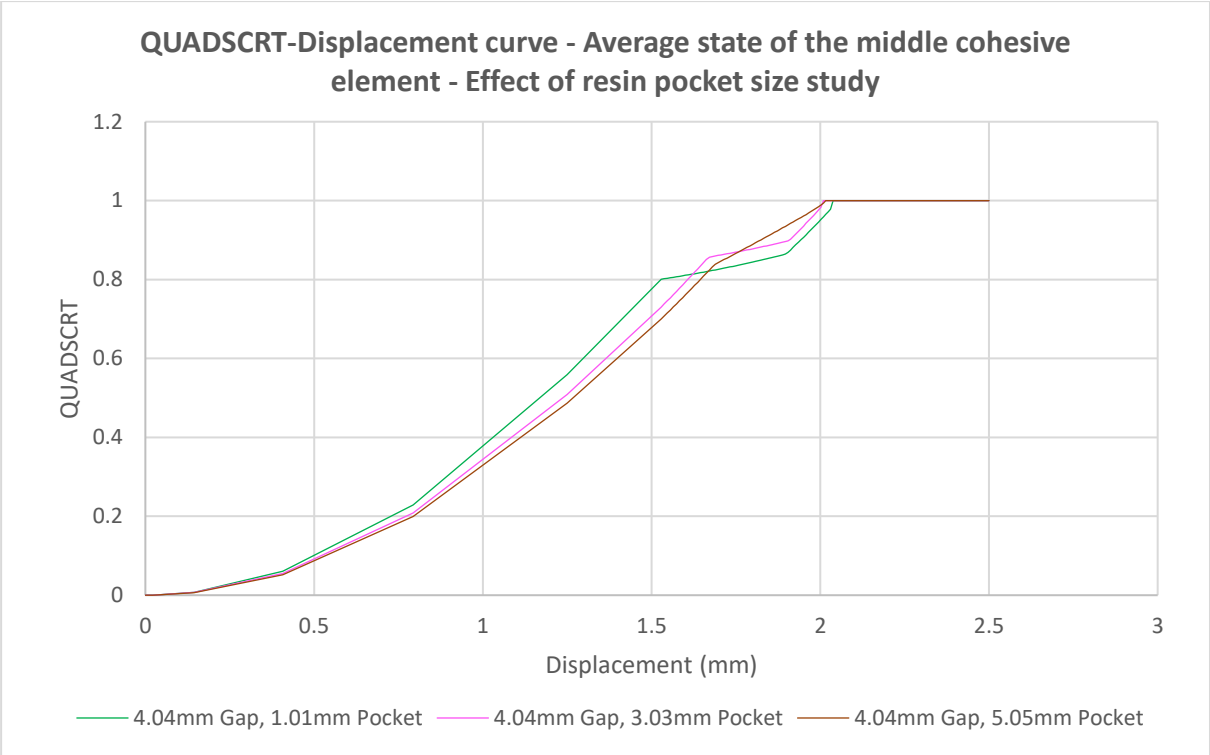


Figure 3.27: QUADSCRT-Displacement curves for the three numerical simulations performed for the effect of pocket size study

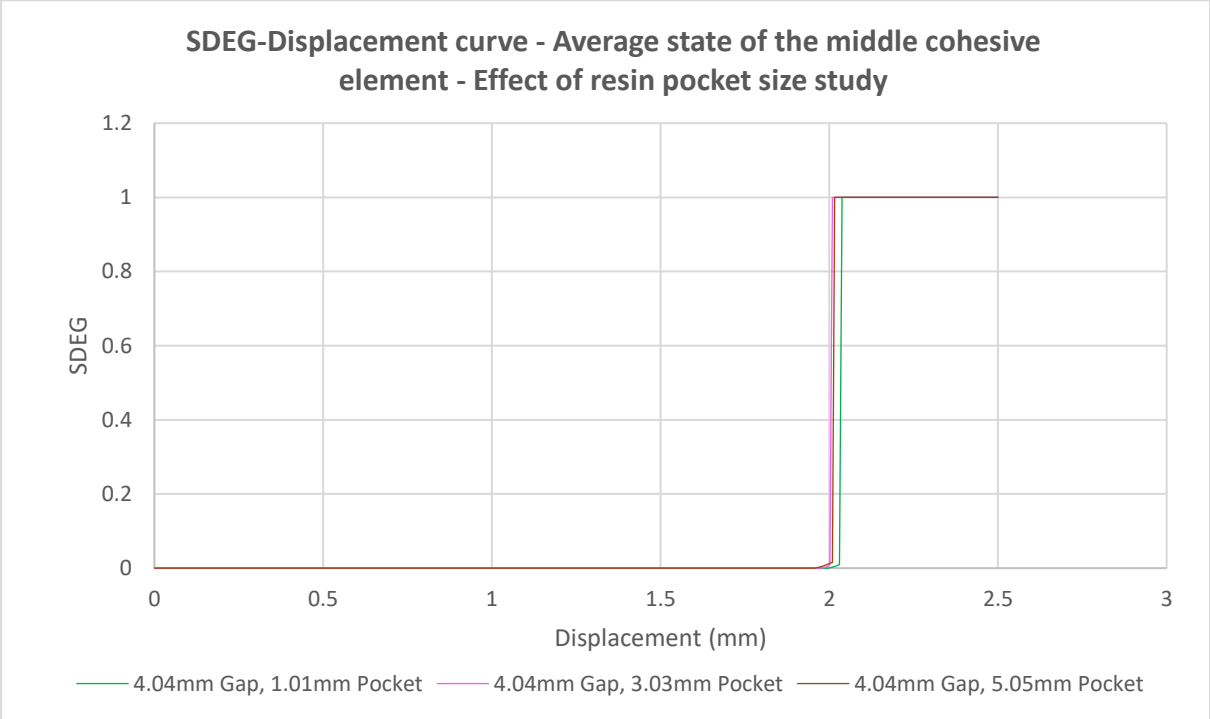


Figure 3.28: SDEG-Displacement curves for the three numerical simulations performed for the effect of pocket size study

As can be seen, the QUADSCRT curves show a progressive increase in the cohesive damage initiation criterion with applied displacement, reaching the critical value of 1 at approximately 2mm for all resin pocket lengths. This indicates that cohesive damage initiation occurs at a very similar displacement for the three configurations. The SDEG curves remain close to zero until this point and then increase abruptly to 1, showing that complete cohesive degradation occurs almost immediately after damage initiation, exactly at the point of displacement where the overall failure of the laminate is experienced. Therefore, the failure process is mainly characterised by a gradual accumulation of cohesive stress before initiation, followed by a sudden and brittle degradation of the cohesive element.

This sudden release of energy as the middle cohesive element degrades causes the glass fibre composite layers to become overstressed, thus failing; even achieving fibre tensile failure in localised areas of the 0° glass fibre orientated regions, as seen in Figure 3.29. It must be mentioned that the HSNFTCRT parameter is the Hashin fibre tensile damage initiation criterion, which, when equal to 1, indicates that tensile failure of the fibres has been achieved.

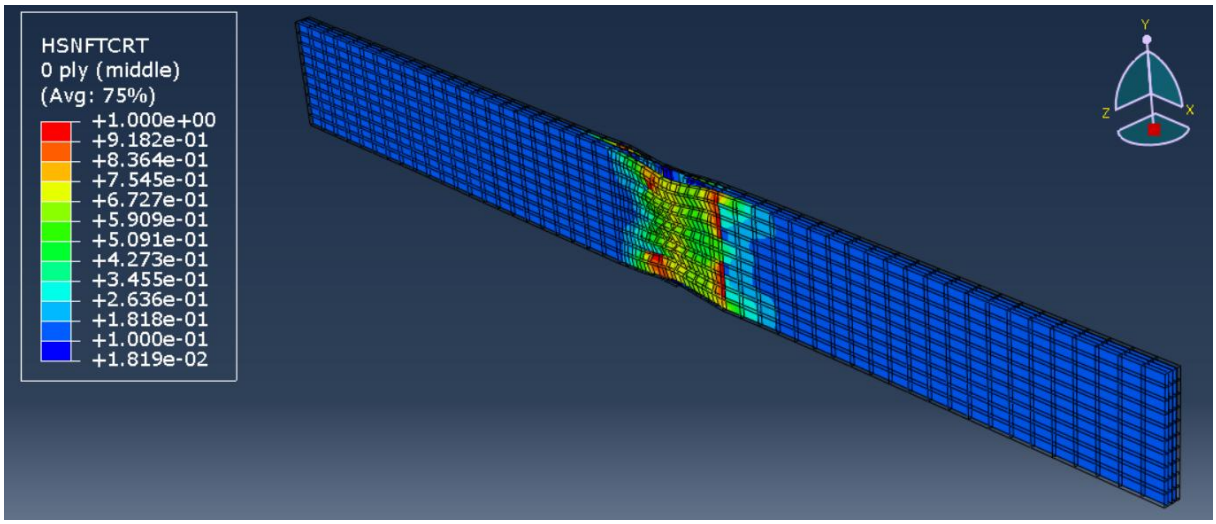


Figure 3.29: Post-failure Hashin fibre tensile damage initiation criterion (HSNFTCRT) analysis of the 0° fibre orientated regions of a numerically simulated laminate for the effect of pocket size study

This phenomenon gives reason to believe that, with the material properties that have been exposed in Section 3.2.2 of this dissertation, the overall failure point of a numerically simulated composite laminate is dictated solely by the failure point of the cohesive elements that sit between the composite continuum shell elements.

For subsequent study of the effect of the length between resin pockets, the value of the resin pocket aspect ratio $l_{pocket}/t_{1\ ply}$ has been chosen to be equal to 3, with l_{pocket} being equal to 3.03mm. This has been the case as this value offers the best compromise between reducing the experienced stress concentrations and manufacturability, since bigger voids in the material may cause excessive resin accumulation, local ply sagging, loss of fibre continuity and greater difficulty in controlling the geometry of the resin-rich pocket during manufacturing.

Effect of the length between resin pockets study

Having learned that, for the numerical simulation conditions, what dictates the failure point of the laminate is the cohesive material that is close to the region where the glass fibre mat layer discontinuities are located, the objective to improve the tensile performance of the simulated laminate is to delay stress concentrations around the resin pockets as much as possible in terms of the amount of displacement achieved. Based on Ahamed's [19] findings, this objective should be achieved by increasing the length between the resin pockets. In Figure 3.30 and Figure 3.31, the obtained load-displacement and engineering stress-strain curves can be observed for the performed simulations for the study of the effect of the length between the resin pockets l_{gap}.

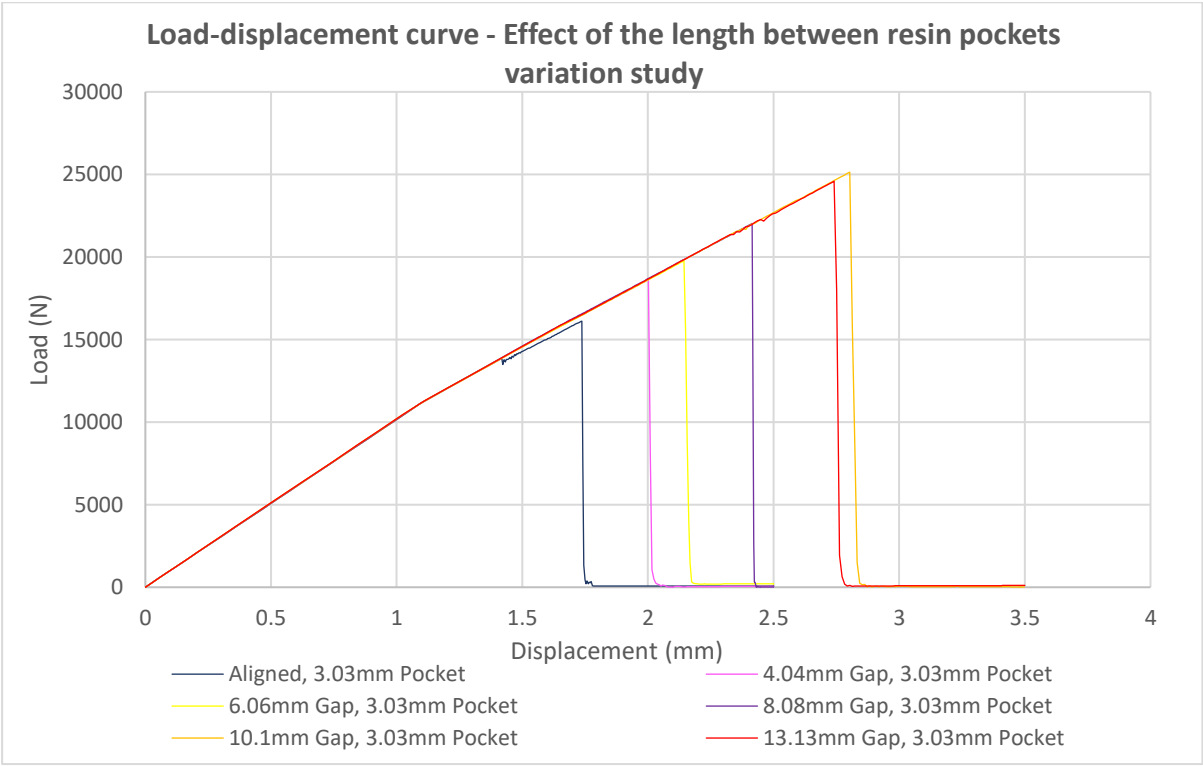


Figure 3.30: Load-displacement curve of the effect of the length between resin pockets variation study

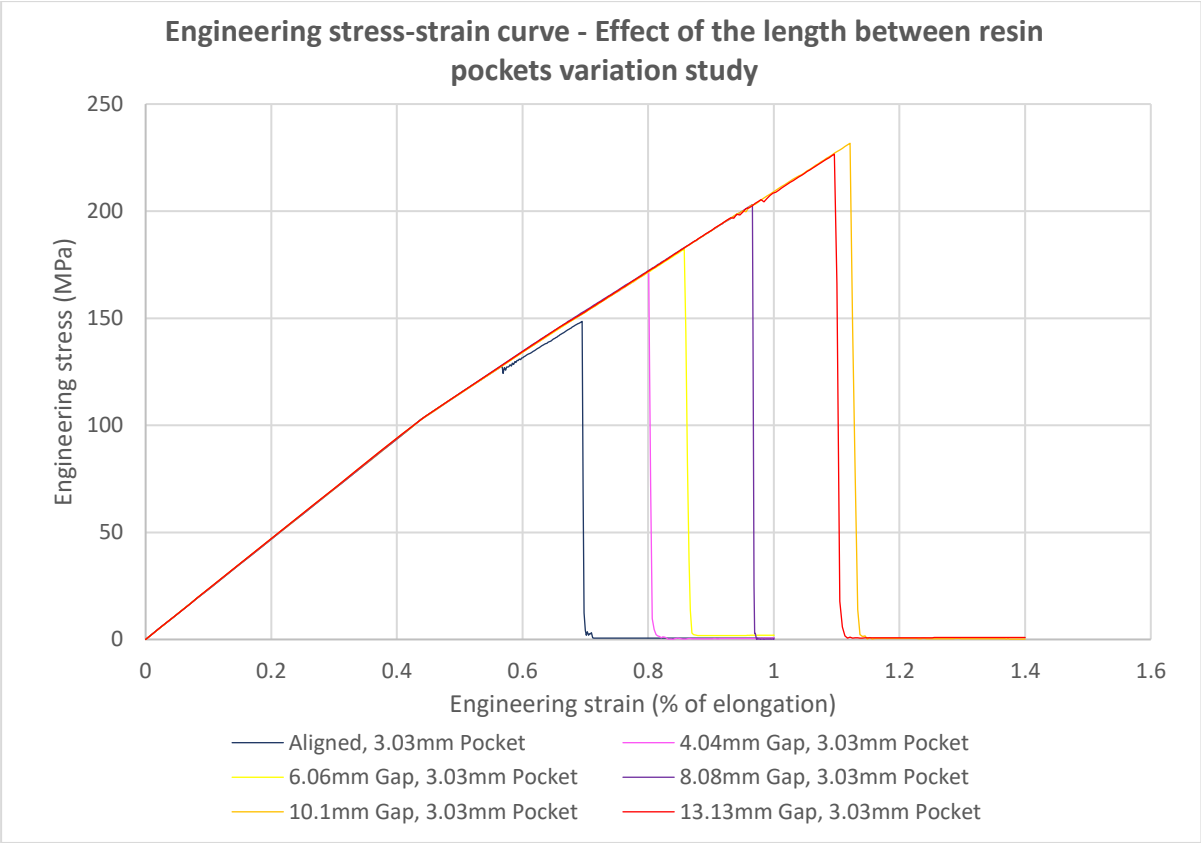


Figure 3.31: Engineering stress-strain curve of the effect of the length between resin pockets variation study

As can be seen, numerical simulations were run with values of the normalised step length $l_{gap}/t_{1\,ply}$ ranging from 4 to 13. The numerical simulation that was run with a value $l_{gap}/t_{1\,ply}$ equal to 10, or l_{gap} equal to 10.1mm offered the best results in terms of tensile performance before complete laminate failure. It is also pertinent to mention that a numerical simulation was also run where both of the resin voids have been placed one on top of the other, creating a pocket double the normal size that has been experienced so far. This case has been denominated as "aligned", and will be treated as a special case, different from the other numerical simulations of this study. For clarification on this ply joint configuration variant, see Figure 3.17.

Analysing the curve generated by the aligned variant numerical simulation, since this ply joint configuration does not have a middle cohesive element between the two voids, which typically is the most critical cohesive region; the most critically loaded cohesive regions are those that are near the corners of the resin pocket, as seen in Figure 3.32. The discontinuity in the aligned variant at a displacement equal to 0.55mm in Figure 3.30 and Figure 3.31 is due to the initiation of the process of degradation of these cohesive regions. This will be explained later on in this section.

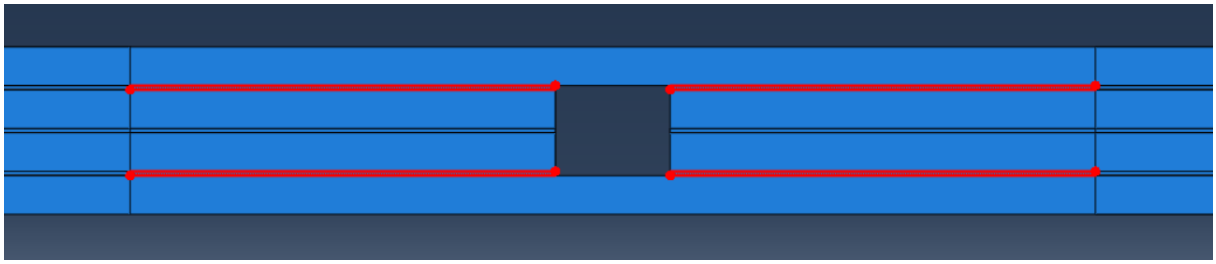


Figure 3.32: Location of the critical cohesive regions in the aligned ply joint variant (longitudinal direction)

In Table 3.12, the progression of the tensile performance of the numerical simulations according to the effect of the variation of the length between resin pockets can be analysed. It can be concluded that the simulated ultimate tensile performance of the laminate improves as the length between resin pockets increases, until this l_{gap} value is equal to 10.1mm, where it plateaus, as the variation in performance when increasing this value further is very small. It is for this reason that it can be concluded that, for the given material properties, the minimum optimum length between resin pockets is equal to 10.1mm. As for the aligned variant, its tensile performance is quite poor when compared to the other numerical simulations.

Table 3.12: Performance analysis chart of the effect of the length between resin pockets variation study

Normalised step length $l_{gap}/t_{1\,ply}$ (mm/mm)	l_{gap}	**Maximum load**	**Displacement at maximum load**	**Maximum stress**	**Strain at maximum stress**
4	4.04 mm	18627 N	2 mm	171.679 MPa	0.801 %
6	6.06 mm	19768 N	2.14 mm	182.199 MPa	0.857 %
8	8.08 mm	22033 N	2.42 mm	203.074 MPa	0.966 %
10	10.1 mm	25138 N	2.8 mm	231.69 MPa	1.121 %
13	13.13 mm	24587 N	2.74 mm	226.616 MPa	1.096 %
Aligned		16113 N	1.73 mm	148.512 MPa	0.694 %
Coefficient of variation		15.284 %	16.787 %	15.284 %	16.715 %

Continuing with the performance analysis, the maximum stress components σ_{11}^{peak}, τ_{13}^{peak}, τ_{23}^{peak} and σ_{33}^{peak}; as well as the stress ratios $\sigma_{11}^{peak}/\sigma_{eng}$, $\tau_{13}^{peak}/\sigma_{eng}$, $\tau_{23}^{peak}/\sigma_{eng}$, and $\sigma_{33}^{peak}/\sigma_{eng}$ can be seen in Table 3.13 and Table 3.14.

Table 3.13: Peak stress values recorded in all three numerical simulations performed for the effect of the length between resin pockets variation study

Normalised step length $l_{gap}/t_{1\,ply}$ (mm/mm)	l_{gap}	σ_{11}^{peak}	τ_{13}^{peak}	τ_{23}^{peak}	σ_{33}^{peak}
4	4.04 mm	659.980 MPa	50.129 MPa	18.212 MPa	11.879 MPa
6	6.06 mm	663.613 MPa	39.708 MPa	17.035 MPa	9.775 MPa
8	8.08 mm	724.663 MPa	41.047 MPa	21.025 MPa	9.568 MPa
10	10.1 mm	821.139 MPa	44.345 MPa	24.631 MPa	8.167 MPa
13	13.13 mm	802.362 MPa	42.940 MPa	26.521 MPa	8.373 MPa
Aligned		718.934 MPa	42.417 MPa	15.535 MPa	7.056 MPa
Coefficient of variation		8.458 %	7.666 %	19.466 %	16.699 %

Table 3.14: Stress ratios of all three numerical simulations performed for the effect of the length between resin pockets variation study

Normalised step length $l_{gap}/t_{1\,ply}$ (mm/mm)	l_{gap}	$\sigma_{11}^{peak}/\sigma_{eng}$	$\tau_{13}^{peak}/\sigma_{eng}$	$\tau_{23}^{peak}/\sigma_{eng}$	$\sigma_{33}^{peak}/\sigma_{eng}$
4	4.04 mm	3.844	0.291	0.106	0.069
6	6.06 mm	3.639	0.217	0.093	0.053
8	8.08 mm	3.567	0.202	0.103	0.047
10	10.1 mm	3.544	0.191	0.106	0.035
13	13.13 mm	3.541	0.189	0.117	0.036
Aligned		4.840	0.285	0.104	0.047
Coefficient of variation		12.115 %	15.916 %	6.687 %	23.849 %

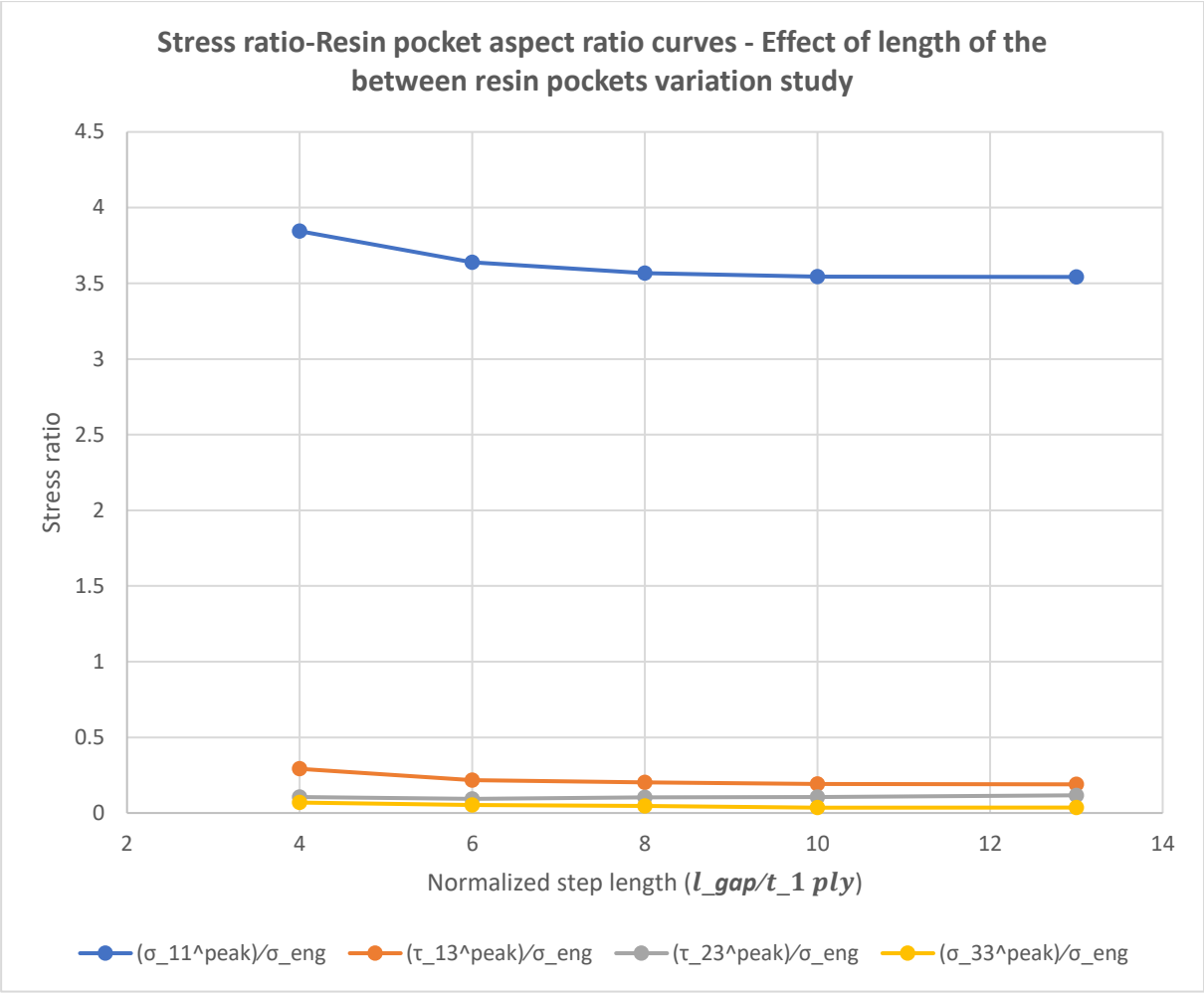


Figure 3.33: Evolution of the stress ratios vs. the normalised step length in all five numerical simulations for the effect of the length between resin pockets variation study

After analysing all the results found in Table 3.13, Table 3.14 and Figure 3.33, it can be concluded that increasing the normalised gap length reduces the severity of the stress concentrations around the resin-rich regions. The most relevant reductions were observed for $\sigma_{11}^{peak}/\sigma_{eng}$, $\tau_{13}^{peak}/\sigma_{eng}$ and $\sigma_{33}^{peak}/\sigma_{eng}$, indicating that larger spacing improves axial load transfer and reduces cohesive shear and peel loading, with the little caveat of the slight variations that $\tau_{23}^{peak}/\sigma_{eng}$ suffers among the different numerical simulations. However, the difference between $l_{gap}/t_{1\,ply} = 10$ and $l_{gap}/t_{1\,ply} = 13$ was very small for most stress ratios, showing that the response had practically stabilised at $l_{gap}/t_{1\,ply} = 10$. Therefore, a normalized gap length of approximately 10 times the ply thickness can be considered a suitable compromise, since it provides nearly the same stress reduction as the larger gap while avoiding an unnecessary increase in joint length. In contrast, the aligned configuration produced the highest

longitudinal stress concentration and a high interlaminar shear ratio, confirming that through-thickness alignment of ply discontinuities should be avoided.

Starting with the cohesive failure analysis of the numerical simulations aimed at studying the Influence of the length between the resin voids, the critical cohesive region is still the middle cohesive element (see Figure 3.26). In Figure 3.34 and Figure 3.35, the progression of the cohesive failure analysis parameters can be analysed for the average state among the geometries of the middle cohesive element.

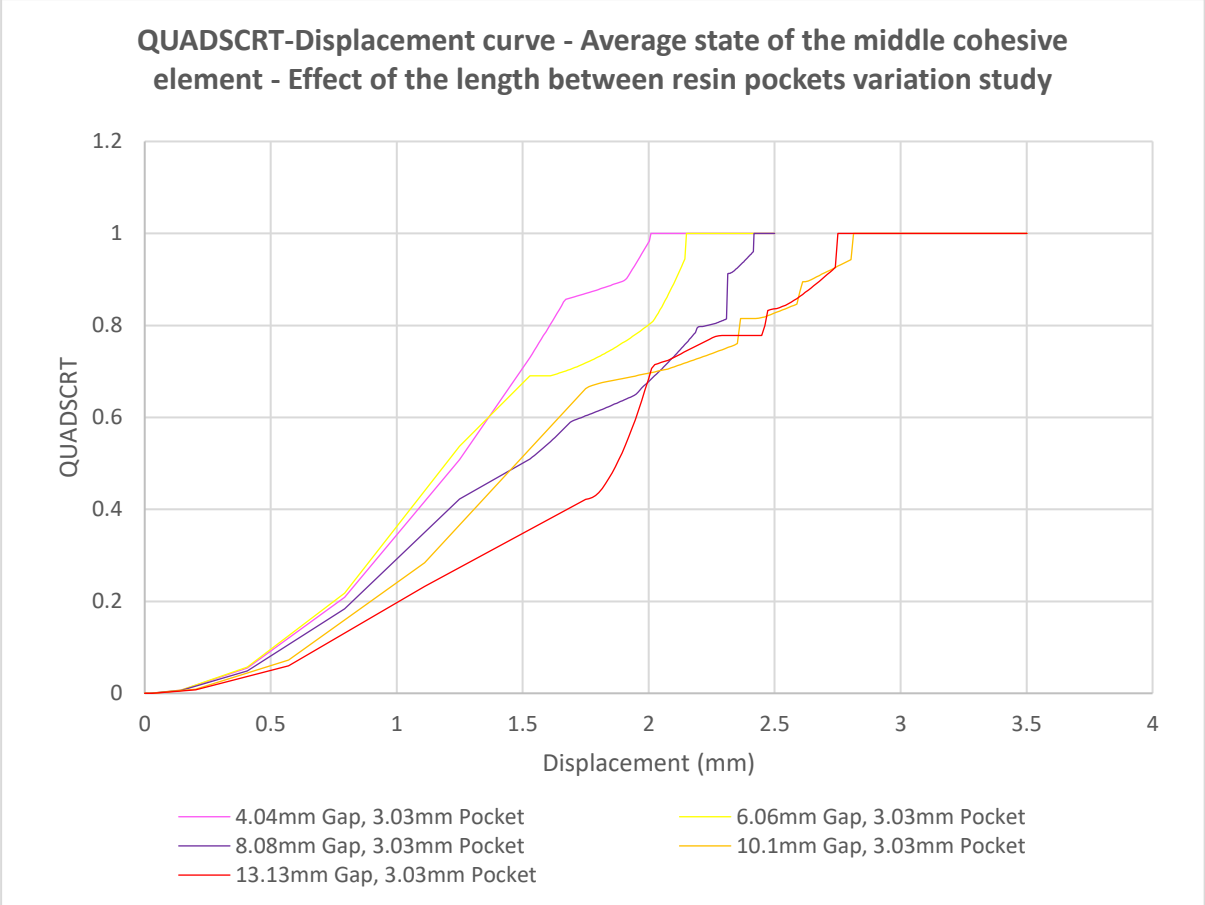


Figure 3.34: QUADSCRT-Displacement curves for the three numerical simulations performed for the effect of the length between resin pockets variation study

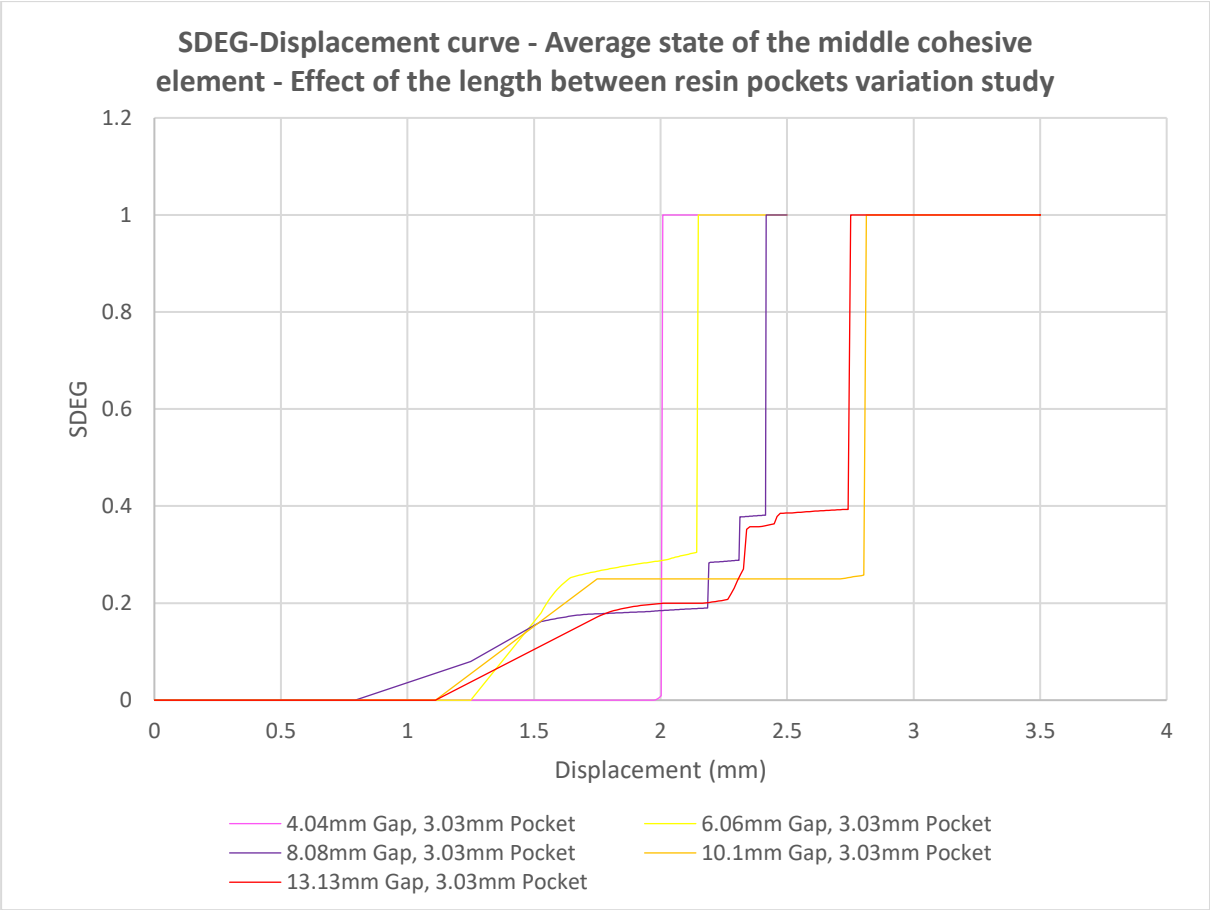


Figure 3.35: SDEG-Displacement curves for the three numerical simulations performed for the effect of the length between resin pockets variation study

The QUADSCRT–Displacement curves show that increasing the distance between resin pockets delays the initiation of cohesive damage. The shortest gap, 4.04mm, reached the damage initiation criterion earliest, indicating a stronger interaction between the stress fields generated by neighbouring resin-rich regions. Larger gaps produced a more delayed response, although the difference between the 10.1mm and 13.13mm gaps was limited, suggesting that the effect of increasing the spacing had almost stabilised. The SDEG–Displacement curves show that, after damage initiation, the cohesive element degradation occurs rapidly, particularly for the smallest gap. This phenomenon where this curve increases in value progressively until reaching a point where the SDEG value increases to its maximum almost immediately for larger gap length variants, is because the more progressive loading of the middle cohesive element, allows the extremities close to the resin voids of other cohesive element to absorb the load and reach to the point where they start to degrade as well, due to them needing more time to reach that point than the middle cohesive element, as It can be observed in Figure 3.36.

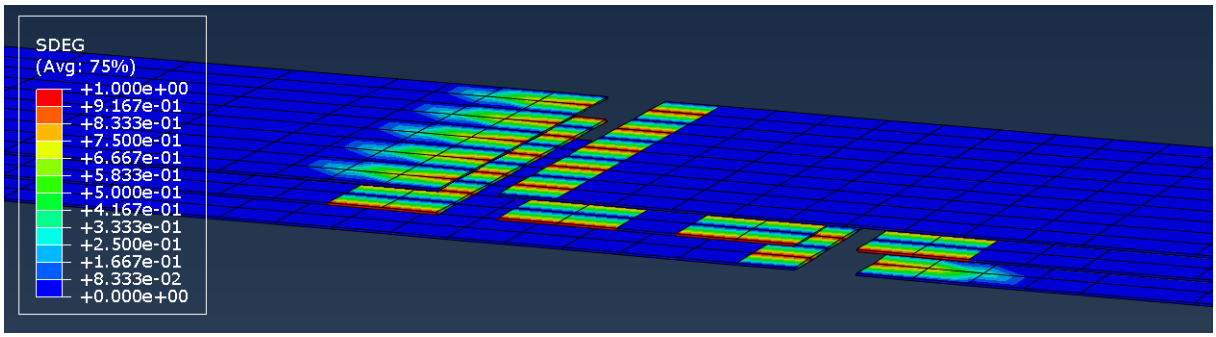


Figure 3.36: SDEG values for all cohesive element edges close to the resin pockets right before complete laminate failure for the numerically simulated normalised step length equal to 10 variant (composite shell elements removed)

Larger gaps allow a more progressive accumulation of damage before final degradation, but all configurations eventually reach complete cohesive failure. Therefore, increasing the gap length improves the damage tolerance of the cohesive region mainly by delaying damage initiation and reducing the abruptness of degradation, with limited additional benefit beyond 10.1mm for the conditions specified for this study.

Even though the tensile performance of the simulated laminate has been considerably improved by this study, its ultimate performance is very small compared to the theoretical maximum load resistance capability for a 4-layered laminate, shown in Eq. (3.14). This is due to the limitations that the cohesive elements material imposes on the behaviour of the rest of the laminate, as it is always the failure point of the laminate.

As for the aligned variant of the numerical simulations performed, in Figure 3.37 and Figure 3.38, the progression of the cohesive failure analysis parameters can be analysed for the average state among the geometries of the middle cohesive element.

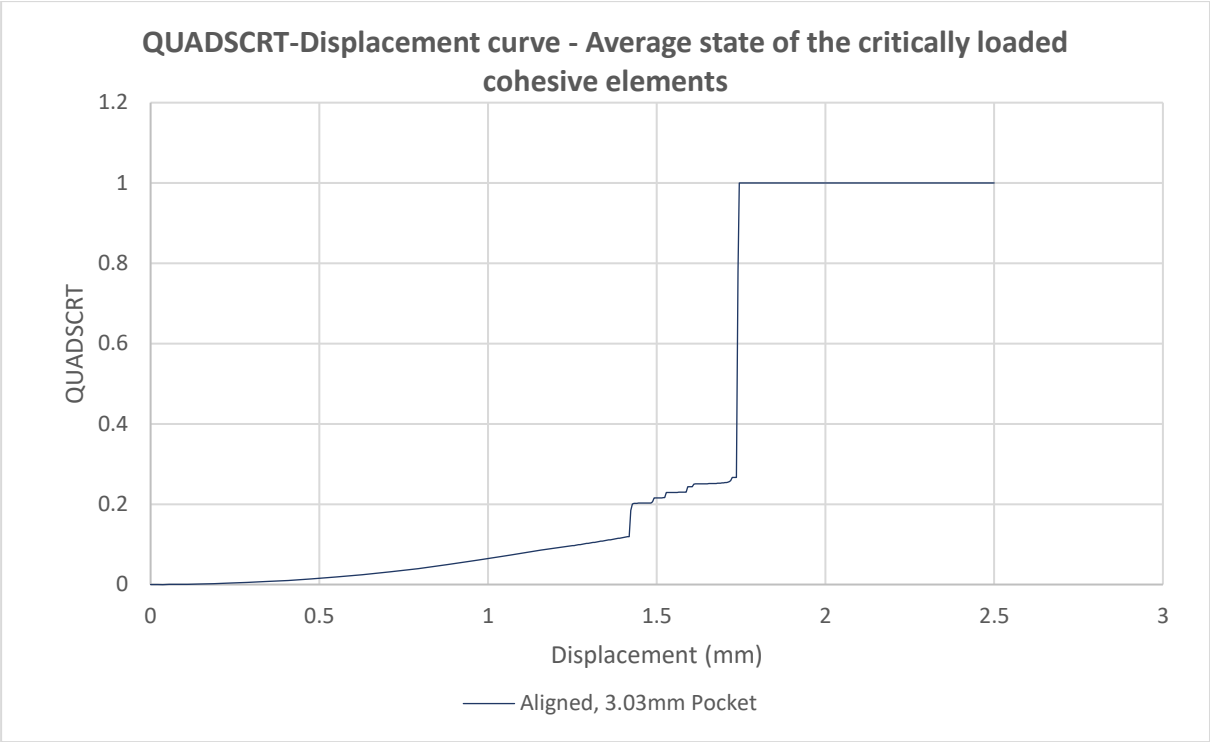


Figure 3.37: QUADSCRT-Displacement curve obtained from the numerical simulation of the aligned ply joint variant

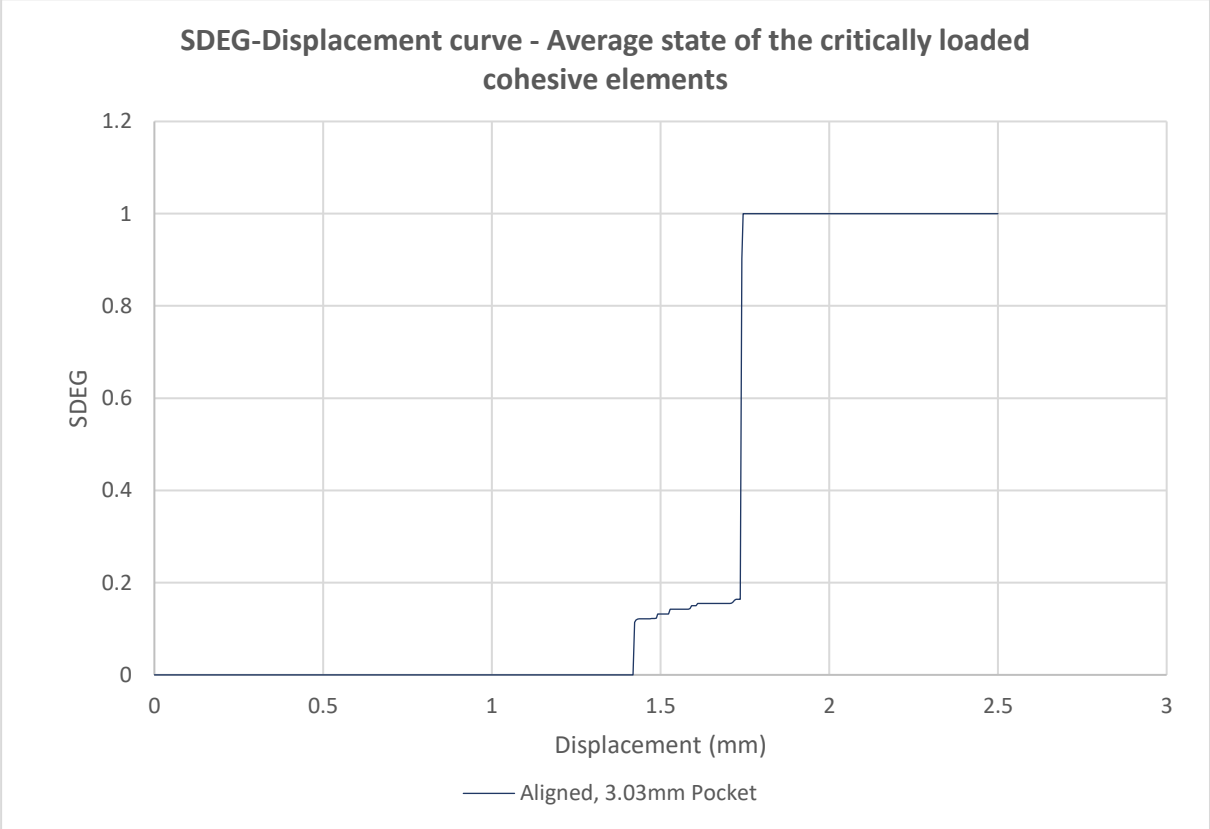


Figure 3.38: SDEG-Displacement curve obtained from the numerical simulation of the aligned ply joint variant

The aligned configuration exhibited an almost linear elastic response until approximately 1.4mm displacement, where small disturbances appeared in the global curves, coinciding with the first increase in the cohesive damage variable SDEG and a jump in value of the QUADSCRT parameter. This indicates that partial and unstable stiffness degradation had started in all four critical cohesive elements, not completely failing but having been weakened, thus explaining the subsequent increase in tensile load that the laminate was able to withstand after this event, albeit at a slower pace compared to the normal elastic behaviour load progression. The load-displacement curve that has been described can be found in Figure 3.30.

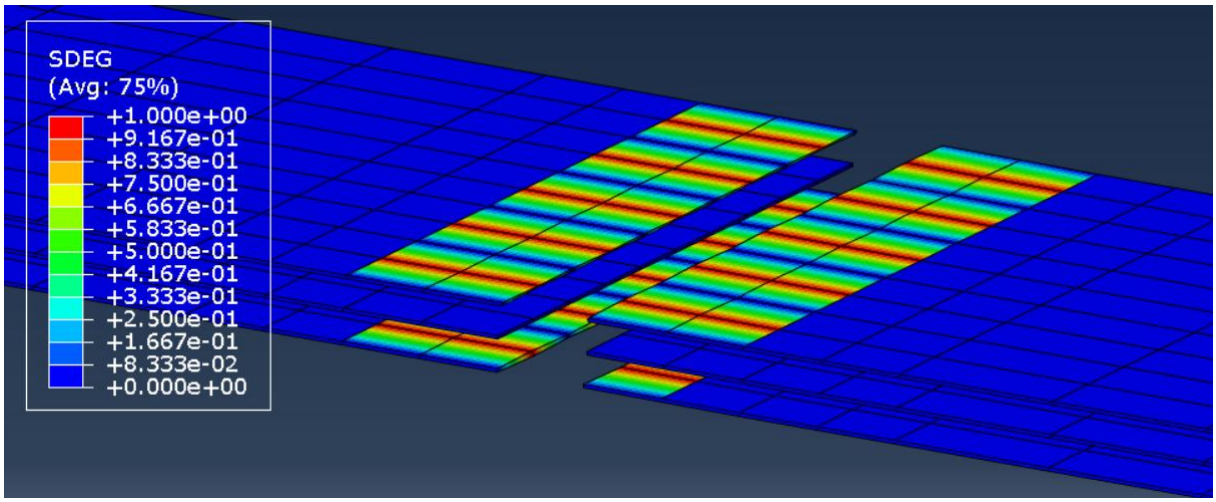


Figure 3.39: SDEG values for all cohesive element edges close to the resin pocket right before complete laminate failure for the numerically simulated "aligned" variant (composite shell elements removed)

3.4.2. Complex end-to-end ply joints numerical results

Mentioned previously in this dissertation, the tensile performance of three complex end-to-end ply joint configurations will be compared; with these configurations being both symmetric interleafed misaligned and aligned scarf ply joints, as well as the asymmetric interleaved misaligned scarf ply joint; with all being able to be seen in Figure 3.20, Figure 3.19 and Figure 3.18, respectively. In Figure 3.40 and Figure 3.41, both the load-displacement and engineering stress-strain curves can be seen. It must be mentioned that, through both studies of the effects of the length between resin pockets and the length of the resin pockets themselves, it was determined that the optimum lengths for both resin pocket length and length between resin pockets were equal to 3.03mm and 10.1mm respectively, to study the complex end-to-end ply joint configurations.

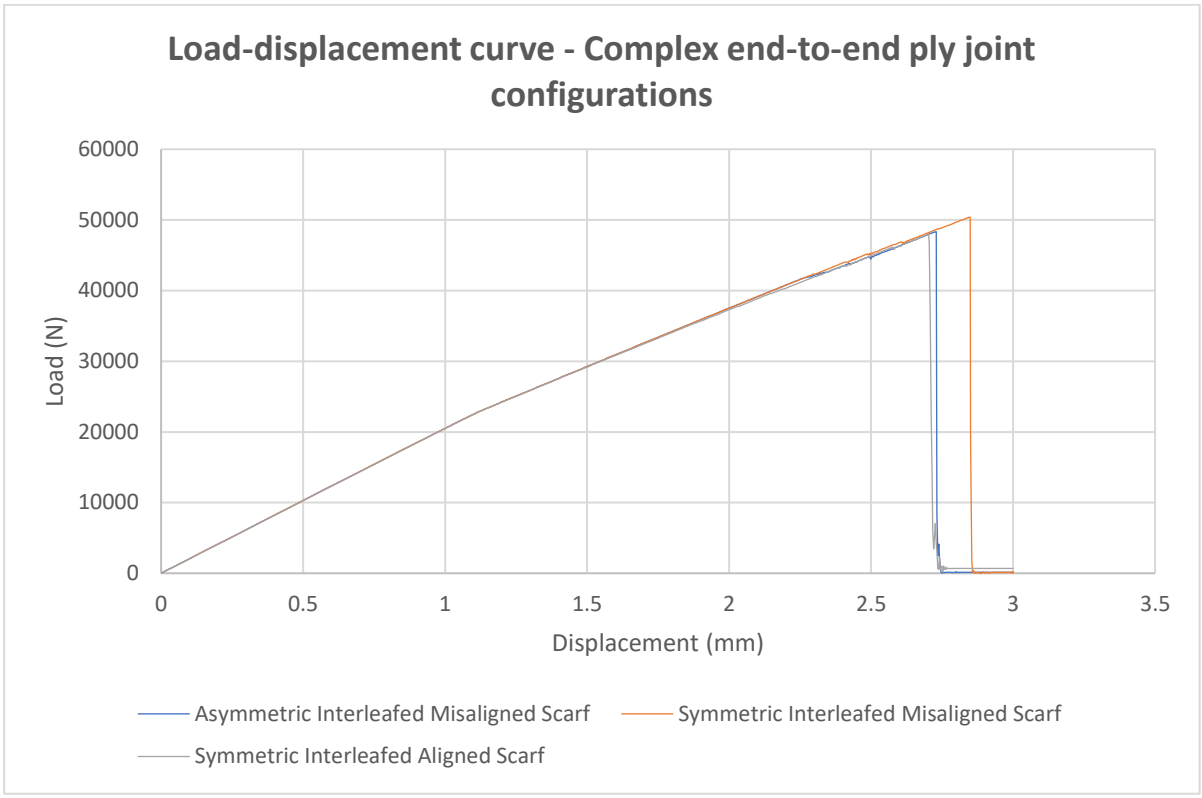


Figure 3.40: Load-displacement curves of all three numerically simulated complex end-to-end ply joint configurations

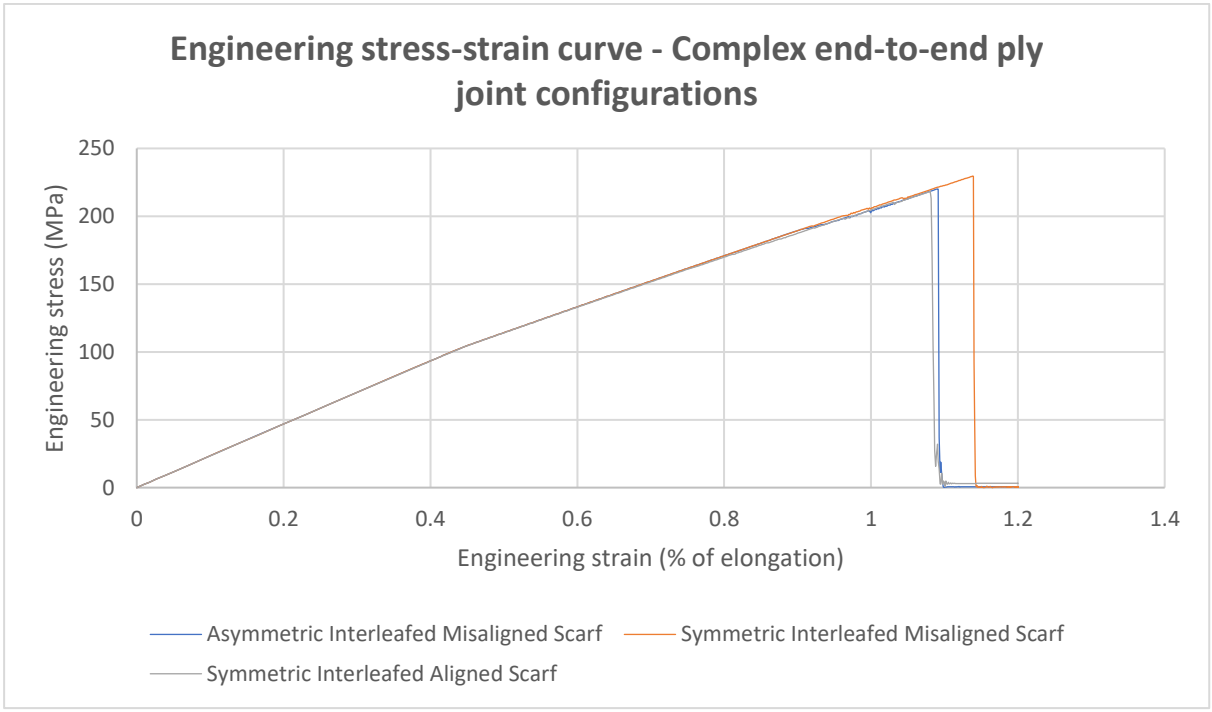


Figure 3.41: Engineering stress-strain curves of all three numerically simulated complex end-to-end ply join configurations

As can be analysed from both the previous figures, the ply joint configuration that offers the best performance is the symmetric interleaved misaligned scarf ply joint configuration, with the asymmetric interleaved misaligned scarf ply joint configuration having slightly better performance than the symmetric interleaved aligned scarf ply joint configuration. Moreover, in all curves in the region near their respective peaks, some instability can be perceived. This phenomenon is due to the numerous cohesive elements entering a state of partial stiffness degradation and instability, experienced right before failing completely. The exact maximum values can be seen in Table 3.15.

Table 3.15: Performance analysis chart of the three different complex end-to-end ply joint configurations

Complex end-to-end ply joint configuration	**Maximum load**	**Displacement at maximum load**	**Maximum stress**	**Strain at maximum stress**
Asym. interleaved misaligned scarf	48314 N	2.73 mm	220.11 MPa	1.092 %
Sym. interleaved misaligned scarf	50377 N	2.84 mm	229.511 MPa	1.139 %
Sym. interleaved aligned scarf	47929 N	2.7 mm	218.357 MPa	1.081 %
Coefficient of variation	2.199 %	2.183 %	2.199 %	2.278 %

By analysing these results, it can be concluded that the symmetric interleaved misaligned scarf ply joint configuration is the best performing out of all three numerically simulated complex joint configurations. However, if the theoretical maximum force for an 8-glass fibre mat layered laminate is, by using the calculus method described in Eq. (3.14), the maximum theoretical load that the laminate could withstand is $F_{max,theoretical} = 107.06\ \mathrm{kN}$; roughly double the value of the ultimate load achieved by the best-performing complex ply joint configuration.

Table 3.16: Percentage of the theoretical maximum load achieved by each of the complex end-to-end ply joint configurations

Complex end-to-end ply joint configuration	$F_{max,config.,sim} / F_{max,theoretical}$
Asym. interleaved misaligned scarf	45.128 %
Sym. interleaved misaligned scarf	47.055 %
Sym. interleaved aligned scarf	44.768 %

It is for this reason, after having performed the various studies to understand the behaviour of the simulated laminates under tensile conditions, that it is safe to conclude that the cohesive material properties used for these numerical simulations need to be a lot stiffer to extract more performance out of the composite material laminates fabricated by applying ply joining techniques. This will also need to be corroborated by real-world tensile testing of laminate coupons fabricated by vacuum infusion.

THIS PAGE WAS INTENTIONALLY LEFT BLANK

4. EXPERIMENTAL CHARACTERISATION OF GLASS FIBRE/EPOXY COMPOSITE LAMINATES

An experimental programme was carried out to obtain real mechanical data from manufactured glass fibre/epoxy composite laminates and compare it with the results obtained from the Abaqus/CAE numerical simulations. The specimens were tested under tensile loading in order to evaluate their load–displacement response, stress–strain behaviour, maximum load and failure mechanisms. This experimental validation was necessary to assess whether the numerical models could reproduce the real behaviour of the composite joint configurations, especially considering the influence of ply discontinuities, resin-rich regions, damage initiation and delamination.

4.1. Specimen manufacturing process

4.1.1. Materials used for the production of the composite material laminates

Composite material fibre reinforcement

Previously described in Section 3.2.1 of this dissertation, the material used for the fibre reinforcement of the composite material has been G-0/1/0/1-1264 waste bi-axial glass fibre mats, of total thickness equal to 1.01mm, being composed of two stitched unidirectionally orientated layers of E-glass fibres [48].

Colour code	Designation	Type	Grammage per orientation g/m²				Total (without thread)	Thick-ness (calc.)	Chamfer 4*)	
			0°	+45°	90°	-45°	g/m²	mm	Long.	Trans.
Pink Blue	(G-0/1/0/1-1264)	biax	-	594	-	594	1188 1*)	1.01	60 mm	60 mm

Figure 4.1: Composition data of G-0/1/0/1-1264 waste bi-axial glass fibre mats [48]

It is important to mention that, due to the nature of the glass fibre mats used in this work, the material could not be considered perfectly controlled or identical to commercial reinforcement supplied directly for laminate manufacturing. The mats corresponded to waste cut-outs generated during wind turbine

blade production, meaning that they had already undergone handling, cutting, storage and transport before being reused. As a result, several imperfections were present, including local twisting, waviness, fibre misalignment, surface dirt, dust contamination, frayed edges, small folds and variations in flatness caused by poor storage and manipulation, as seen in Figure 4.2. These defects are relevant because they can influence resin impregnation, fibre alignment and local stress distribution during tensile loading. Therefore, the experimental results must be interpreted considering that the reused material presents a higher level of variability than new, fully controlled reinforcement material.



Figure 4.2: G-0/1/0/1-1264 waste bi-axial glass fibre mat used in the test laminate manufacturing process

Composite material matrix

The Gurit PRIME™ 37 resin system was used as the matrix material for the glass fibre/epoxy laminates manufactured in the experimental programme. This resin was selected because it is specifically intended for liquid infusion processes such as RIFT, VARTM and RTM, making it suitable for the manufacturing method used in this work [77]. The datasheet describes PRIME™ 37 as a bio epoxy infusion system compatible with glass, carbon and aramid fibre reinforcements, and highlights its ability to provide good fibre wetting and improved laminate quality [77].

From a material perspective, PRIME™ 37 was appropriate because it acts as the continuous polymer matrix that binds the glass fibres together, transfers stresses between them and contributes to the final stiffness and strength of the laminate. The resin system also contains bio-sourced material as standard, which is consistent with the sustainability objectives of this work and the reuse of glass fibre waste materials [77]. Therefore, the use of Gurit PRIME™ 37 allowed the recycled glass fibre mats to be

transformed into solid composite laminates suitable for tensile testing and comparison with the numerical simulations.

4.1.2. Manufacturing process

Vacuum infusion manufacturing process

Vacuum infusion was used to manufacture the composite laminates tested in the experimental programme. In this process, the dry glass fibre mats were first placed on a flat working surface, together with the required auxiliary materials, such as peel ply, flow media and vacuum bagging film. The assembly was then sealed using vacuum tape, and a vacuum pump was used to remove the air from inside the bag. Once the vacuum was established, the resin was introduced through the inlet line and drawn through the fibre reinforcement by the pressure difference created between the resin inlet and the vacuum outlet [8, 9].

This manufacturing method allows the fibres to be impregnated in a controlled way while reducing the presence of trapped air and improving laminate consolidation [9] . In the present work, no shaped cast or mould cavity was used for the laminate production. Instead, the specimens were produced on a flat surface, meaning that the final laminates were manufactured as flat composite plates that were later prepared for tensile testing. This approach was suitable because the objective was to produce simple flat coupons rather than complex curved components, following the general specimen requirements for tensile testing of polymer matrix composites [70].

Preparation of the glass fibre mats

The glass fibre reinforcement used in the experimental programme was supplied as waste cut-outs from wind turbine blade manufacturing. These sections were approximately 1 m wide and 2m long, so they had to be reduced to smaller pieces before laminate manufacturing. Since the stitched biaxial mat was composed of two fibre layers oriented at +45° and −45°, square pieces of 300×300mm were cut with the edges being either parallel or perpendicular to the fibres. This cutting orientation was selected so that, after cutting, the two fibre families would be aligned approximately with the desired 0° and 90° laminate directions.



Figure 4.3: Alignment and measurement of the glass fibre mat sections desired for cutting

The size of 300mm×300mm was selected to manufacture a laminate plate large enough to later extract 6 specimens of dimensions in accordance with the ISO 527-4:2023 norm, which can be seen in more detail in Annex A, by using a CNC cutting machine. The dimensions were marked manually using a measuring tape and a marker, and the pieces were then cut by hand using scissors.



Figure 4.4: Manual cutting of the waste glass fibre mats

Before cutting, the large glass fibre mat sections were placed on a plastic film to avoid further contamination from the working surface. The mats were then flattened and straightened as much as possible in order to reduce the twisting, waviness and fibre misalignment caused by previous storage, handling and manipulation. Nevertheless, a certain degree of imperfections should be expected, which must be considered when interpreting the experimental results, because fibre misalignment, waviness, voids and local defects can influence the mechanical response of composite laminates and increase the scatter of tensile test results [26].

Preparation of the matrix

Before preparing the matrix system, the required resin quantity was calculated from the target fibre volume fraction of the laminate. In this work, a fibre-matrix volume fraction of 0.6 was used as the initial objective, meaning that the remaining laminate volume corresponded to the matrix phase. Since the approximate volume of each 300mm×300mm glass fibre mat was known, the necessary matrix volume could be estimated before infusion. This was important because the final mechanical properties of a composite laminate depend strongly on the relative proportions of fibre and matrix [53].

The matrix system was prepared using Gurit PRIME™ 37 resin and Ampreg™ 3X Fast hardener. According to the product datasheet, this resin system is intended for liquid infusion processes and is mixed with the Ampreg™ 3X hardeners using a ratio of 100:29 by weight [77]. The two components have different densities, so the required quantities were measured by mass rather than by volume. For this purpose, a precision scale was used, and each component was poured into a clean container until the calculated mass was reached.



Figure 4.5: Weight measurement for the mixing of the matrix

After measuring the resin and hardener, both fluids were combined gently in the same container and slowly stirred until the mixture was considered homogeneous. Care was taken to avoid aggressive mixing, since this could introduce air bubbles into the matrix system. Entrapped air or gas bubbles are undesirable because they can remain as voids after curing, reducing laminate quality and potentially affecting the mechanical response of the composite [26]. For this reason, after mixing, the matrix was left to rest for approximately 10 minutes before being introduced into the vacuum infusion setup, allowing part of the entrapped air to escape before impregnation.



Figure 4.6: Careful stirring of the mixed matrix

Preparation of the vacuum infusion process

The vacuum infusion setup was prepared on a flat glass plate, which was used as the working surface for the laminate lay-up. Before placing the reinforcement, the glass surface was cleaned to remove dust, grease or particles that could contaminate the laminate. A closed loop of sealant tape was then applied around the working area to define the vacuum bagging perimeter, and a release agent was applied with a brush to facilitate the later removal of the cured laminate from the glass surface.



Figure 4.7: Preparation of the flat working surface

The first stage of the lay-up consisted of positioning the two bottom layers of glass fibre mat. The upper layer of these two bottom plies was partially cut to create a controlled fibre discontinuity, which would later form the resin-rich pocket of the joint. The entire mat was not cut completely, so that a certain level of alignment and dimensional control could be maintained during lay-up. The uncut region was positioned outside the area where the tensile specimens would later be extracted. During this process, the fibres were aligned as closely as possible with the desired laminate orientations, although small deviations were expected due to the reused and flexible nature of the glass fibre mats.

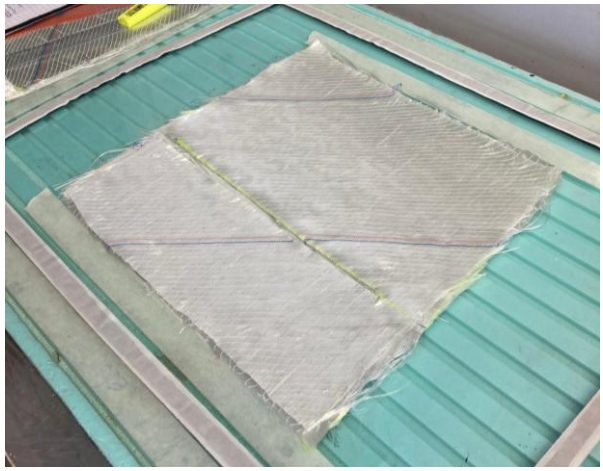


Figure 4.8: First two layers of glass fibre mat, with a fibre discontinuity having been applied to one of them

After the discontinuous ply had been positioned, the LUNA™ fibre optic sensors were placed along the laminate symmetry plane. These sensors were included to measure strain during the tensile tests, providing local strain information that could later be compared with the numerical predictions.

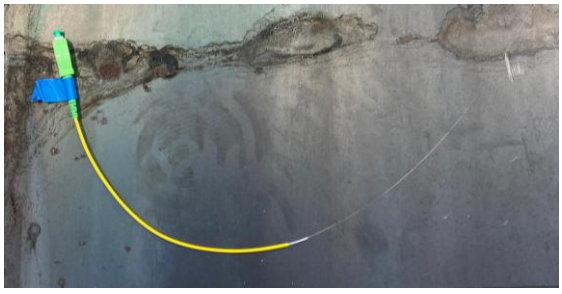


Figure 4.9: LUNA™ optic fibre used to measure strain

Distributed fibre optic sensing systems, such as LUNA™ ODiSI, are particularly useful for composite testing because they can obtain high-resolution strain measurements along the length of a single optical fibre, rather than only at isolated points as with conventional strain gauges [78]. The sensors were secured using small glass fibre mat cut-outs placed over the ends of the optical fibre and fixed with an aerosol adhesive, positioned always in the areas where the end taps would be positioned in each of the 6 specimens; as the black marker lines imply in Figure 4.10.

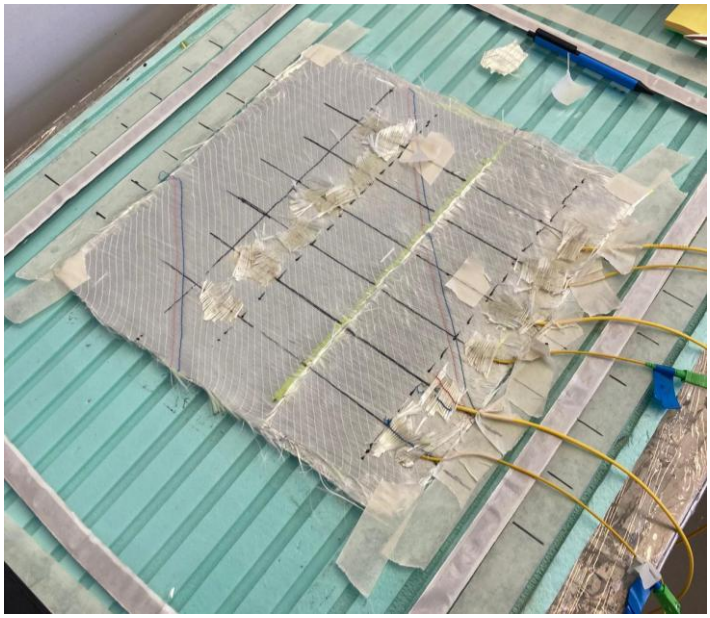


Figure 4.10: Position securing method used for the optic fibre LUNA™ strain sensors

After the sensors had been positioned, the two upper glass fibre mat layers were applied, maintaining the symmetry of the fibre orientation lay-up. The results of these sensors will not be used for the present study of this dissertation, ultimately being collected for another purpose of the CirWind project.

The auxiliary infusion materials were then positioned. A peel ply layer was placed on top of the reinforcement to create a removable surface layer after curing and to help separate the laminate from the infusion consumables. Above this, the infusion mesh was positioned to improve the in-plane flow of the resin during infusion. The mesh was arranged so that the resin flow front could be distributed as evenly as possible across the laminate. In particular, the mesh was placed over the continuous regions of the glass fibre mats and not directly over the discontinuity region. This was done because the fibre discontinuity already created a lower-resistance resin path, while the continuous fibre regions offered greater resistance to resin flow [8, 9].

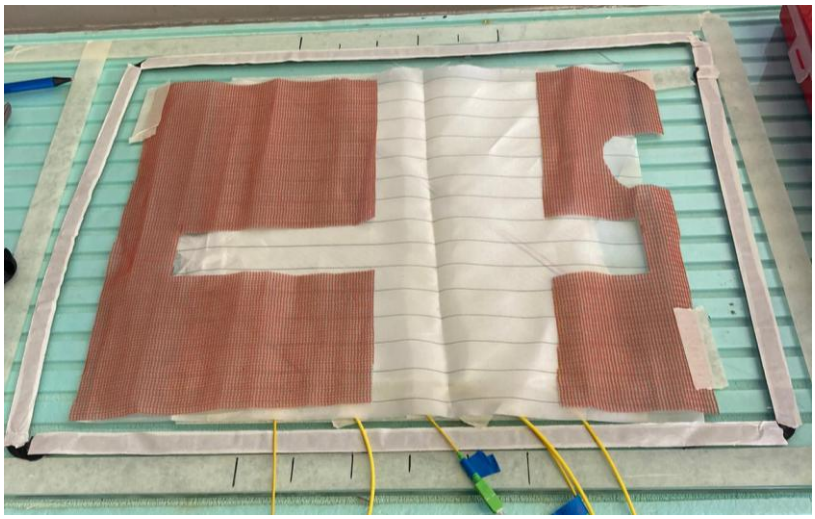


Figure 4.11: Peel ply and infusion mesh positioning

A spiral feed tube was then positioned at one end of the laminate, together with 3D-printed supports for the inlet and outlet tubes, which were sanded to get rid of any sharp printing imperfections and avoid vacuum bag ruptures once the vacuum is applied. The function of the spiral tube was to create a low-resistance channel through which the resin could flow freely along the width of the laminate before progressing through the reinforcement. This helped the resin enter the laminate more uniformly and reduced the risk of an uneven flow front during infusion.

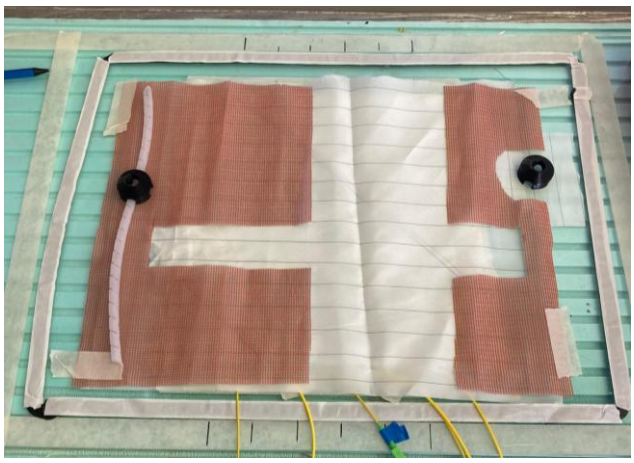


Figure 4.12: Positioning of tube supports and spiral feed tube positioning

As can be observed in Figure 4.13, this disposition of the infusion mesh was effective, as the resin flow front is homogeneous during the impregnation process; with the darker area being the laminate's half that has already been infused with resin.

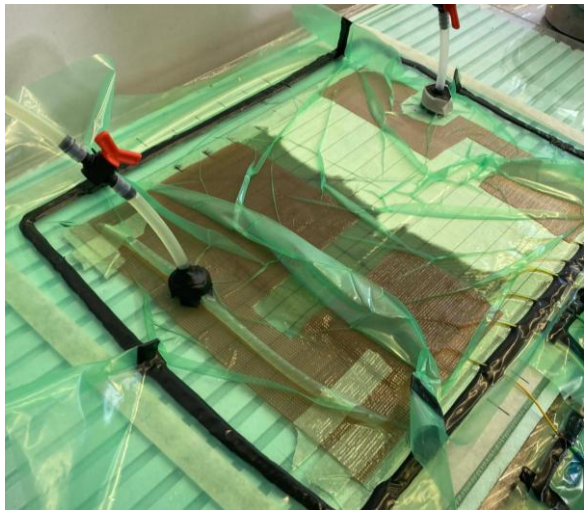


Figure 4.13: Resin flow front during the infusion process

The vacuum bagging film was then placed over the complete lay-up. Sufficient slack was left in the bag so that, when vacuum was applied, the film could conform properly to all areas of the laminate and to the inlet and outlet tube supports. This was important because an excessively tight bag can bridge over corners or raised regions, leaving air pockets that may later become resin-rich defects. Poor bag placement can also increase the risk of tearing or leakage when vacuum is applied. Holes were created in the vacuum bag for the inlet and outlet tubes, and additional sealant tape was applied around these regions to maintain air-tightness. The ends of the fibre optic sensor cables were also carefully vacuum bagged, because air can infiltrate through the gap between the external plastic cable coating and the optical fibre, as seen in Figure 4.15.

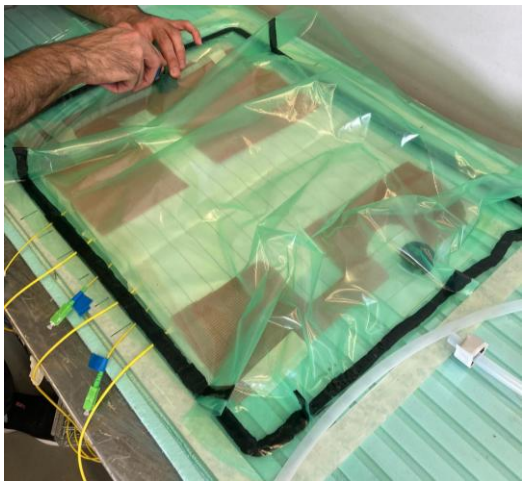


Figure 4.14: Vacuum bag application and sealing process

Finally, the vacuum pump and collection bucket were connected to the system. Before resin infusion, vacuum was applied to check the sealing quality of the setup. Any leaks detected during this stage were repaired until a stable vacuum level was achieved. Once the vacuum was stable, the inlet tube was placed into the container with the mixed matrix resin, allowing the pressure difference to draw the resin into the laminate. When the resin had travelled across the full laminate length and began to reach the outlet tube, the valves on both the inlet and outlet lines were closed to maintain vacuum during the curing period. The collection bucket was included as a safety component to prevent resin from reaching the vacuum pump and to allow the vacuum level to be monitored using the pressure gauge. This was essential because resin entering the vacuum equipment could cure inside the system and render the components unusable for future occasions.

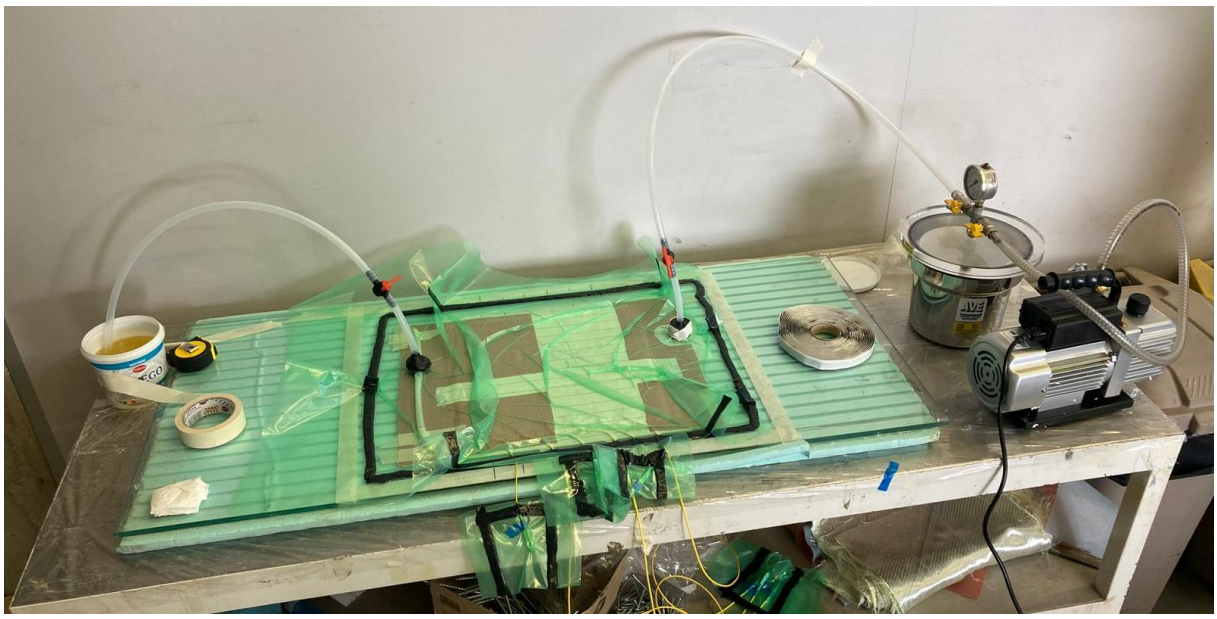


Figure 4.15: Full vacuum infusion system

After the curing process, all auxiliary material layers were carefully removed, and the composite laminate was carefully separated from the glass pane by the use of a spatula.

Ply joint configurations manufactured

The first ply joint configuration that was produced was a 4-glass fibre mat layered, aligned resin pocket ply joint, as seen in Figure 4.16.

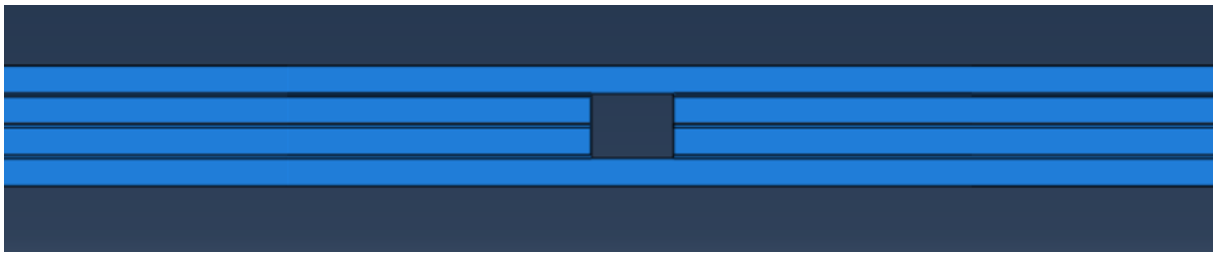


Figure 4.16: Aligned 3mm length resin pocket ply joint configuration

The size of the resin pocket was kept at approximately 3mm to better resemble the aligned ply joint configuration that was numerically simulated with the Abaqus CAE software.



Figure 4.17: Measurement of resin-rich pocket length

After the production process of this ply joint configuration, the resulting composite laminate had experienced a local depression resulting from the sagging and out-of-plane waviness of the continuous outer plies into the 3 mm internal reinforcement discontinuity under vacuum compaction.



Figure 4.18: Fibre sagging experienced in the aligned 3mm resin pocket length ply joint configuration laminate

Ply sagging over an internal discontinuity can reduce the tensile performance of a laminate because it introduces local fibre waviness, thickness variation and a larger resin-rich region. These imperfections disturb the axial load path and can increase local stress concentrations around the discontinuity, especially in the load-carrying plies [72, 73]. Under tensile loading, the sagged region may also promote interlaminar peel and shear stresses, increasing the risk of matrix cracking, cohesive damage and delamination initiation [73, 76]. In addition, fibre waviness, misalignment and void-like defects are known to reduce composite laminate strength, meaning that sagging can increase result scatter and lower the effective load-carrying capacity of the specimen [26].

To mitigate this phenomenon, the other two laminates produced would have both ends of the discontinuous layers placed right next to each other, having a 0mm resin pocket length. The ply joint laminate production process was repeated for the aligned ply joint configuration and for the ply joint configuration that had the resin pockets separated by approximately 10mm, the best performing out of all the numerically simulated simple 4-layered ply joint configurations.



Figure 4.19: Aligned 0mm length resin pocket ply joint configuration



Figure 4.20: Stepped 10mm gap 0mm length resin pocket ply joint configuration

CNC specimen cutting

After the manufacture of the 300mm×300mm composite laminate plates, the specimens required for tensile testing were extracted using a CNC cutting machine. Each laminate was cut into 6 rectangular specimens with final dimensions of 250mm×25mm, following the geometry selected for the experimental tensile programme. The use of CNC cutting allowed the specimens to be produced with more consistent dimensions, straighter edges and better repeatability than manual cutting methods.

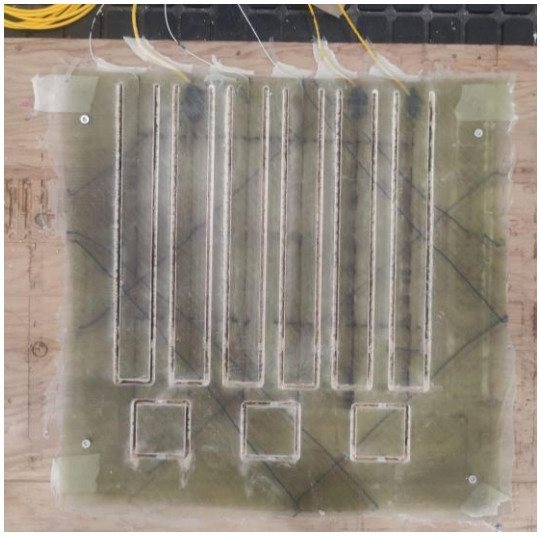


Figure 4.21: Composite laminate after the CNC cutting process

Due to the fragility of the LUNA™ optic fibre sensors, the remaining uncut section of each specimen was cut manually by the use of a rotary cutting tool, as seen in Figure 4.22.

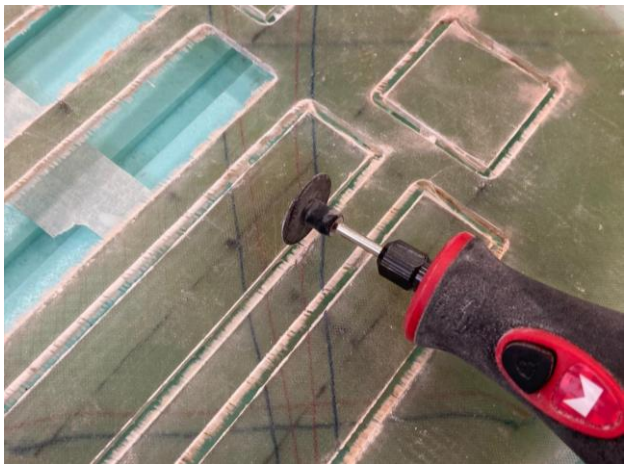


Figure 4.22: Hand-cut final separation of the various specimens from the parent ply joint configuration laminate

Before cutting the final specimens, preliminary cutting tests were carried out to define an appropriate tool rotation speed and feed rate. This was necessary because excessive cutting speed or an overly aggressive tool movement can generate significant heat at the contact region between the rotating bit and the composite laminate. If this heat is too high, the epoxy matrix may soften, melt locally or burn, damaging the specimen edges and potentially affecting the mechanical response during tensile testing. Therefore, the cutting parameters were adjusted to obtain clean edges while avoiding thermal damage to the resin-rich regions and surrounding glass fibre/epoxy material.



Figure 4.23: Example of excessive cutting speed leading to the burning of the matrix resin

End tabs application to the specimens

Due to the increase in laminate thickness generated by the application of the small glass fibre mat sections to secure the optic fibre LUNA™ strain sensors, the final surface of the laminate on the side of the vacuum bag was not entirely flat, thus requiring a sanding operation on those ends of the specimens to glue the aluminium end tabs. As little composite material as possible was removed in order not to damage the physical properties of the laminate specimens. The glue used to glue the composite specimens to the end tabs was CEYS Araldite™ fast-acting epoxy bi-component adhesive [79].

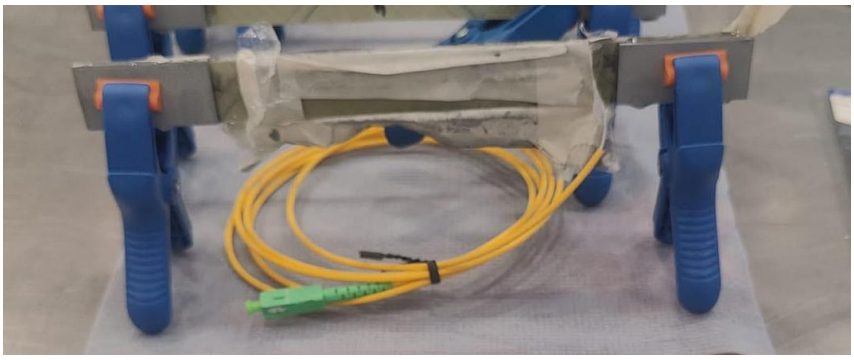


Figure 4.24: Specimen during end tab adhesive curing process

4.1.3. Tensile testing data acquisition

Firstly, a naming convention must be defined for cataloguing all the test specimens. For this, the following naming nomenclature was devised.

Table 4.1: Test specimen type naming nomenclature

End-to-end ply joint configuration	Naming nomenclature code
Aligned 3mm length resin pocket	BD4-P3-o0-TX
Aligned 0mm length resin pocket	BD4-P0-o0-TX
Stepped 10mm gap 0mm length resin pocket	BD4-P0-o10-TX

where BD4 stands for bi-directional 4-layer, P stands for the length of the resin pocket in millimetres and the o for the gap distance between resin pockets, with 0 signifying that the resin pockets are aligned. After these nomenclatures, a T followed by a number (marked with an X) was added to signify the specimen number of each type of ply joint laminate.

Additionally, one side of each specimen was painted with a contrasting paint along with 4 spots so that the high-definition slow-motion video extensometer could better capture and track the strain that each specimen was enduring. The four spots were reference points for fixing the tracking software focus points and measuring the relative displacement between two marked points on the specimen surface.



Figure 4.25: Example of contrasting paint applied to a specimen

Four painted tracking points were used instead of only two in order to obtain a more reliable strain measurement and to provide additional information about the deformation of the specimen. Video extensometer methods can use four calculation points to determine longitudinal and transverse strain, improving the ability to monitor the deformation field within the gauge region [80]. This was especially relevant for the present composite coupons, since small imperfections, bending, fibre misalignment or local discontinuities can produce non-uniform deformation during tensile testing [70, 72, 73, 76].

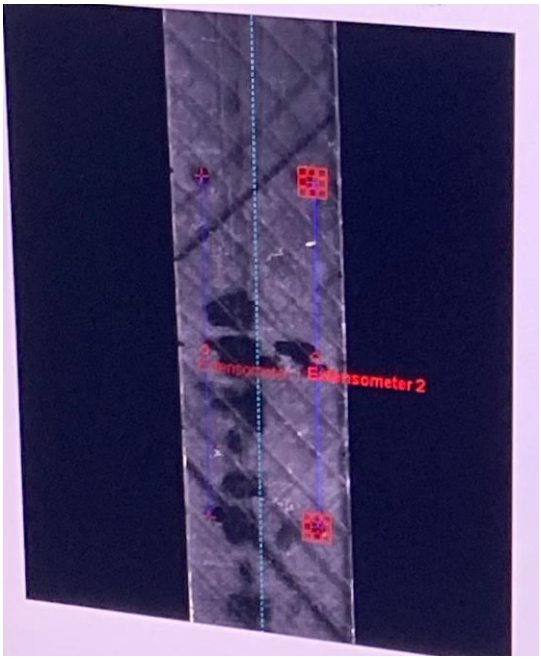


Figure 4.26: Virtual extensometer ends placement on top of painted spots before the tensile testing

Prior to the use of the video extensometer, it must be properly calibrated in order for the software to generate accurate results. This is achieved by the use of a specially marked element, which is positioned parallel to the specimen. Since the software recognises the marking and the length between them is known, the software of the video extensometer can work out the distance between it and the composite specimen tested.

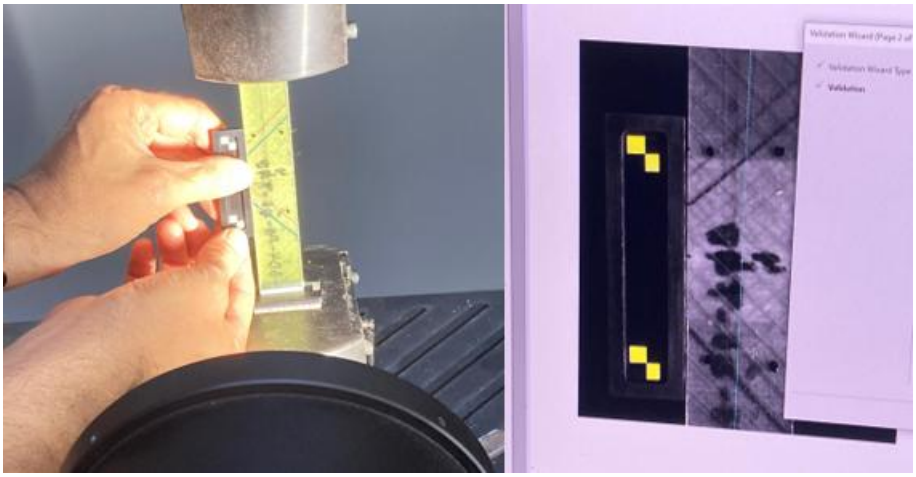


Figure 4.27: Video extensometer calibration process

Before testing each of the composite coupons, the average cross-sectional area must be calculated for each one by measuring the width and thickness at 5 different points along the length of each specimen. According to the ISO-527-4-2023 norm, as seen in Annex A, 3 measurements must be done, one at the middle of the coupon and two more either side of that middle point, 12.5mm apart. Since for the aligned ply joint configurations that were produced, the main layer discontinuity was located in the middle of the coupon, 2 more measuring points were added either side of the lateral ones, separated by the same 12.5mm distance. This was necessary because the middle measurement of the thickness on the aligned coupons was not representative due to the internal layer discontinuities; therefore, for all coupons of that type, this middle measurement was not included in the average cross-section area calculations. In Figure 4.28, the measurement points and their numbering can be seen in all the ply joint configurations produced, which were measured manually by the use of a digital measuring calliper.

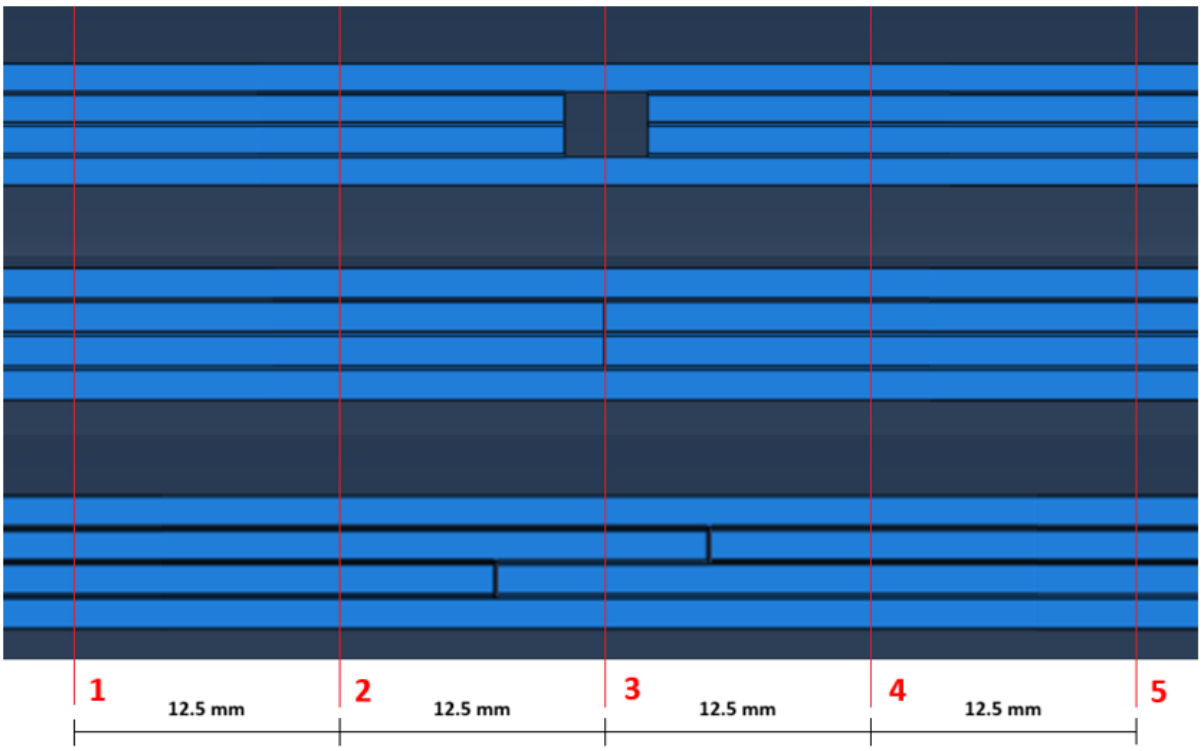


Figure 4.28: Width and thickness numbered measurement points of the laminate coupons for all ply join configurations produced, marked with red lines

The results of these measurements can be seen from Table 4.2 to Table 4.4. As previously mentioned, the central measurement for both aligned laminate specimens has been omitted from the average cross-section area calculations, with those values being shown in grey in Table 4.2 and Table 4.3.

Table 4.2: Aligned 3mm length resin pocket laminate average specimen cross-section calculations

BD4-P3-o0 (Aligned 3mm length resin pocket)													
Specimen	Width (mm)						Thickness (mm)						Avg.
Measure point	1	2	3	4	5	Avg.	1	2	3	4	5	Avg.	Area [mm²]
T1	24.92	24.87	24.92	24.91	24.88	24.90	3.05	2.94	2.92	3.21	3.29	3.12	77.74
T2	24.91	25.00	24.92	24.90	24.97	24.95	3.21	3.23	3.02	3.20	3.52	3.29	82.07
T3	24.90	24.86	24.97	24.98	24.92	24.92	3.11	3.11	2.74	3.25	3.40	3.22	80.16
T4	24.87	24.90	24.94	25.01	24.90	24.92	3.45	3.34	3.01	3.36	3.47	3.41	84.85
T5	24.91	24.98	24.91	25.03	25.02	24.99	3.20	3.20	2.90	3.29	3.21	3.23	80.58

Table 4.3: Aligned 0mm length resin pocket laminate average specimen cross-section calculations

BD4-P0-o0 (Aligned 0mm length resin pocket)													
Specimen	Width (mm)						Thickness (mm)						Avg.
Measure point	1	2	3	4	5	Avg.	1	2	3	4	5	Avg.	Area [mm²]
T1	24.97	24.97	24.95	24.93	24.99	24.96	3.08	3.18	3.11	3.08	3.18	3.13	78.14
T2	24.96	24.98	25	25.06	24.94	24.98	3.24	3.28	3.1	3.35	3.36	3.31	82.64
T3	24.9	24.91	24.94	24.97	24.93	24.93	2.9	3.02	2.95	3.24	3.14	3.07	76.65
T4	24.88	24.97	24.94	24.94	24.92	24.93	2.89	3	2.94	3.03	3.01	2.98	74.35
T5	24.91	24.9	24.88	24.89	24.91	24.90	3.02	3.14	3.15	3.18	3.1	3.11	77.45
T6	24.92	24.86	24.99	24.96	24.92	24.91	3.33	3.37	3.08	3.38	3.42	3.37	84.09

Table 4.4: Stepped 10mm gap 0mm length resin pocket laminate average specimen cross-section calculations

BD4-P0-o10 (Stepped 10mm gap 0mm length resin pocket)													
Specimen	Width (mm)						Thickness (mm)						Avg.
Measure point	1	2	3	4	5	Avg.	1	2	3	4	5	Avg.	Area [mm²]
T1	25.2	25.26	25.2	25.2	25.21	25.21	3.30	3.39	3.77	3.59	3.35	3.48	87.75
T2	25.14	25.21	25.21	25.17	25.16	25.18	3.30	3.33	3.34	3.37	3.26	3.32	83.59
T3	25.23	25.21	25.24	25.17	25.07	25.18	3.23	3.21	3.31	3.33	3.19	3.25	81.95
T4	25.21	25.23	25.27	25.22	25.15	25.22	3.44	3.46	3.67	3.55	3.37	3.50	88.21
T5	25.21	25.26	25.35	25.25	25.25	25.26	3.46	3.36	3.36	3.37	3.33	3.38	85.29
T6	25.2	25.29	25.18	25.36	25.3	25.27	3.23	3.49	3.31	3.54	3.45	3.40	86.01

During the tensile tests, the mechanical response of the ply-joint laminate specimens was recorded using the MTS Exceed Electromechanical Test System, Model E43. The testing machine measured the tensile force applied to each specimen, while the strain was measured using two video extensometers positioned on the specimen surface [81]. The use of a video extensometer was appropriate because it provides non-contact strain measurement and avoids mechanically interfering with the composite coupon during loading [80].

The strain used for the experimental stress–strain curves was calculated as the average of the two video extensometer readings whenever both signals were stable and reliable (see Figure 4.29). This approach was selected because averaging measurements taken from two equivalent gauge regions can reduce the influence of small specimen misalignment, bending, or local measurement noise [70, 82].

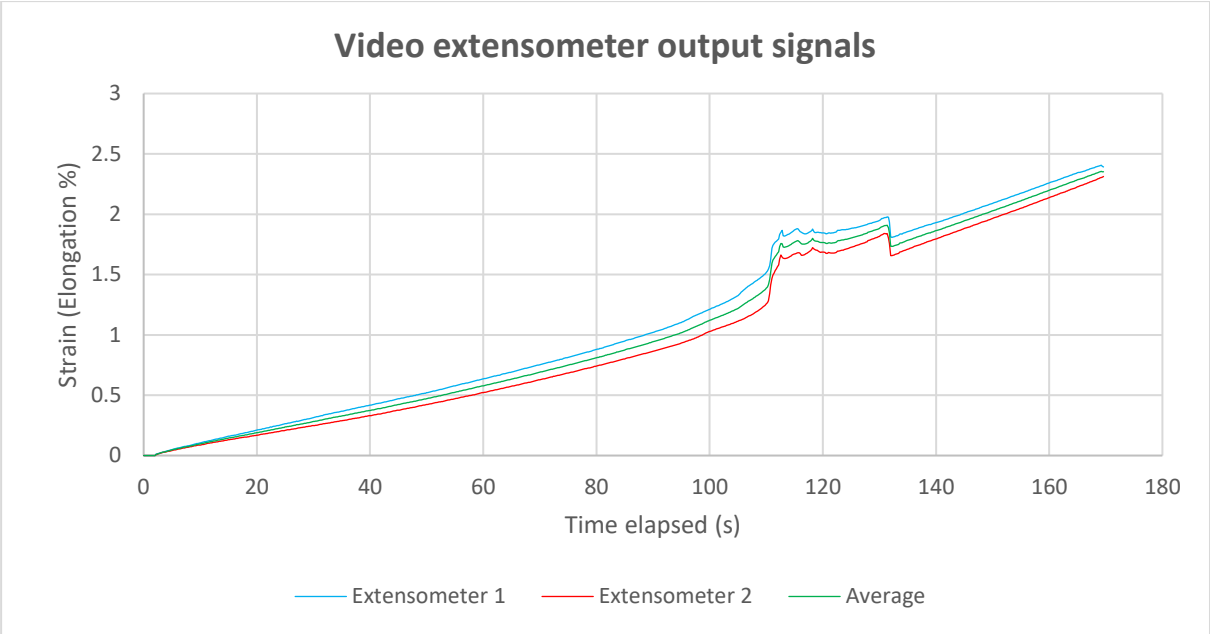


Figure 4.29: Video extensometer output signals average calculation

The displacement used for the load–displacement curve was calculated from the measured strain rather than from the crosshead displacement of the testing machine. For this purpose, the strain was converted into elongation using:

$$\Delta L = \varepsilon_{videoextensometer,avg} \cdot L_0 \tag{4.1}$$

where $\varepsilon_{videoextensometer,avg}$ is the average video extensometer-measured strain, and L_0 is the original length of the specimen. This method was used because crosshead displacement includes not only the real elongation of the coupon, but also possible machine compliance, grip deformation, specimen seating, and small slippage effects. Therefore, it is less reliable for determining the true elongation of the specimen than a direct strain measurement taken from the coupon surface [70, 83].

The engineering stress values used for the stress–strain curves were calculated from the tensile force and the average cross-sectional area of each specimen. Therefore, the stress was obtained as:

$$\sigma_{eng} = \frac{F_{measured}}{A_{cross-section,avg}} \tag{4.2}$$

where $F_{measured}$ is the force measured by the testing machine and $A_{cross-section,avg}$ is the original average cross-sectional area of the specimen. This area was determined from the width and thickness measurements performed before testing, following the general approach used in tensile testing of polymer matrix composite coupons [70].

As the last postprocessing activity, the post-failure region of the load–displacement and stress–strain curves was removed from the processed experimental results because, after laminate failure, the recorded data no longer represented the stable tensile response of the specimen. Once the specimen fractured, the load path was lost, and the remaining readings were strongly affected by sudden unloading, specimen recoil, local sliding, possible grip movement and loss of reliable video-extensometer tracking. This produced erratic curves with rapid forward and backward strain variations, which are not representative of the actual pre-failure mechanical behaviour of the laminate [70, 83]. This allowed the comparison between specimens to focus on the relevant parameters for this work, including stiffness, maximum stress, failure strain and overall tensile response. The post-failure data were therefore excluded because they did not provide useful information for evaluating the load-carrying performance of the ply-joint laminates and could distort the interpretation of the experimental curves.

4.2. Experimental results and discussion

Prior to the analysis of the obtained results, it must be mentioned that the data for both BD4-P3-o0-T6 and BD4-P0-o10-T6 were lost due to human error, so they will not be featured in the study.

4.2.1. Aligned ply joint configurations

Since the only both aligned ply joint configurations are differentiated only by the length of the resin pocket itself, they will be compared to each other and to their analogous numerically simulated configuration, the aligned ply joint configuration with a resin pocket length of 3.03mm. In Figure 4.30 and Figure 4.31, the load-displacement curves can be seen for both laminate configurations.

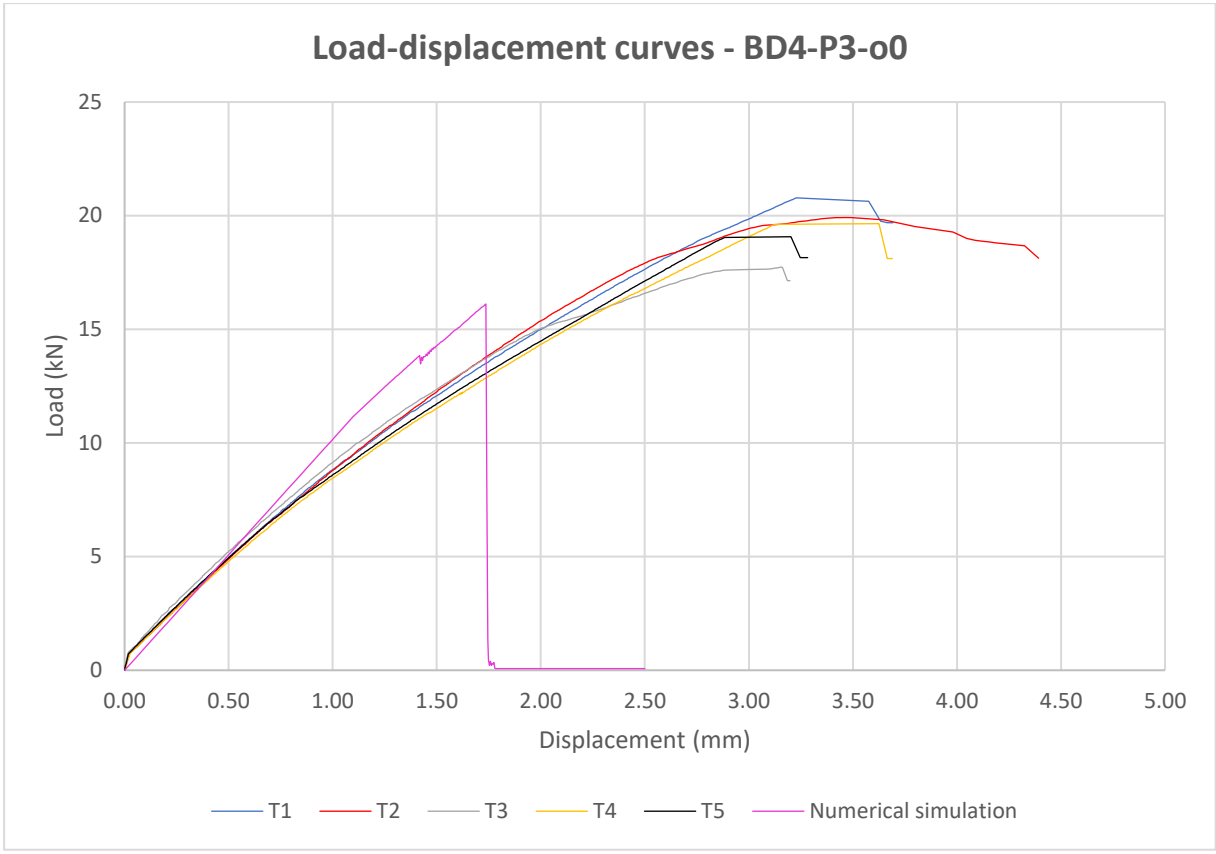


Figure 4.30: Experimental and simulated load-displacement curves for the aligned 3mm resin pocket length laminate

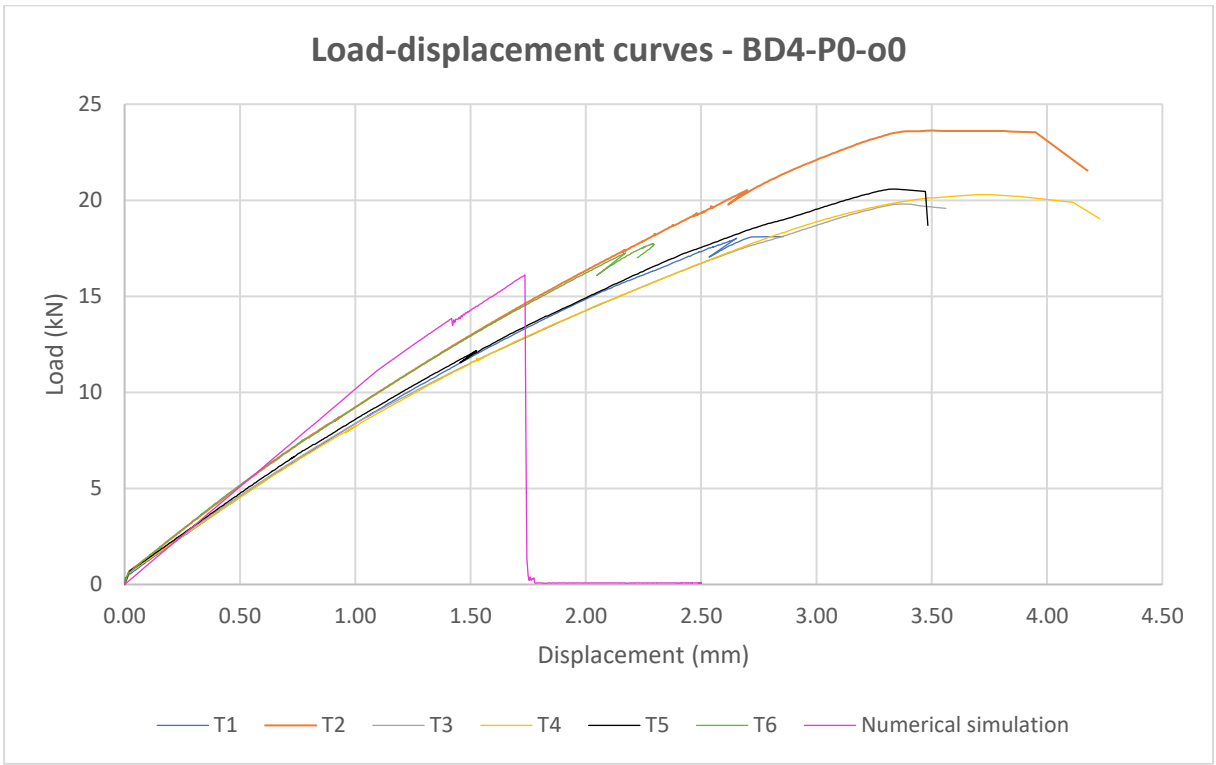


Figure 4.31: Experimental and simulated load-displacement curves for the aligned 0mm resin pocket length laminate

The load–displacement curves show that the numerical simulation reproduces the general stiffness trend of the experimental specimens, but predicts failure at a significantly lower displacement. This indicates that the Abaqus model provides a conservative and more brittle prediction of the aligned 3 mm resin pocket configuration, while the curved nature of the experimental curves indicates a gradual reduction in the tangent stiffness of the specimens before final failure, suggesting that damage in the real laminates developed progressively, rather than occurring as a single sudden event. Local delamination and matrix cracking events also would justify the downward spikes that can be seen in the load-displacement curves of specimens 1, 2 and 6, as seen in Figure 4.31; with slight end tap slippage also being a possibility that would justify this behaviour.

The difference can be explained by the idealised nature of the numerical model, where the resin pocket geometry, cohesive interface and material damage properties are defined in a simplified and deterministic way. In contrast, the experimental specimens include manufacturing variability, such as fibre waviness, local misalignment, resin distribution differences and small deviations in the real discontinuity geometry, which can affect the damage evolution and allow a more progressive failure process. In addition, the experimental displacement was derived from video-extensometer strain measurements, whereas the numerical displacement corresponds to the prescribed boundary displacement, meaning that both quantities may not be fully equivalent when the strain field is non-uniform. Therefore, the numerical model captures the general mechanical tendency of the configuration, but further calibration of the material damage parameters and a more detailed representation of the manufactured geometry would be required to improve the prediction of failure displacement and ultimate load.

Although the discrepancy between the numerical and experimental curves may be partly attributed to the use of material properties obtained from literature and online datasheets rather than from direct characterisation of the manufactured laminates, it cannot be assigned exclusively to this factor. The numerical model also idealised the resin pocket geometry, fibre alignment and cohesive interface, while the experimental specimens presented manufacturing variability associated with reused glass fibre cut-outs. Therefore, the difference between the curves is likely the result of both uncertain damage parameters and simplifications in the numerical representation of the real laminate.

Continuing with the stress-strain curves obtained for these configurations, these can be observed in Figure 4.32 and Figure 4.33.

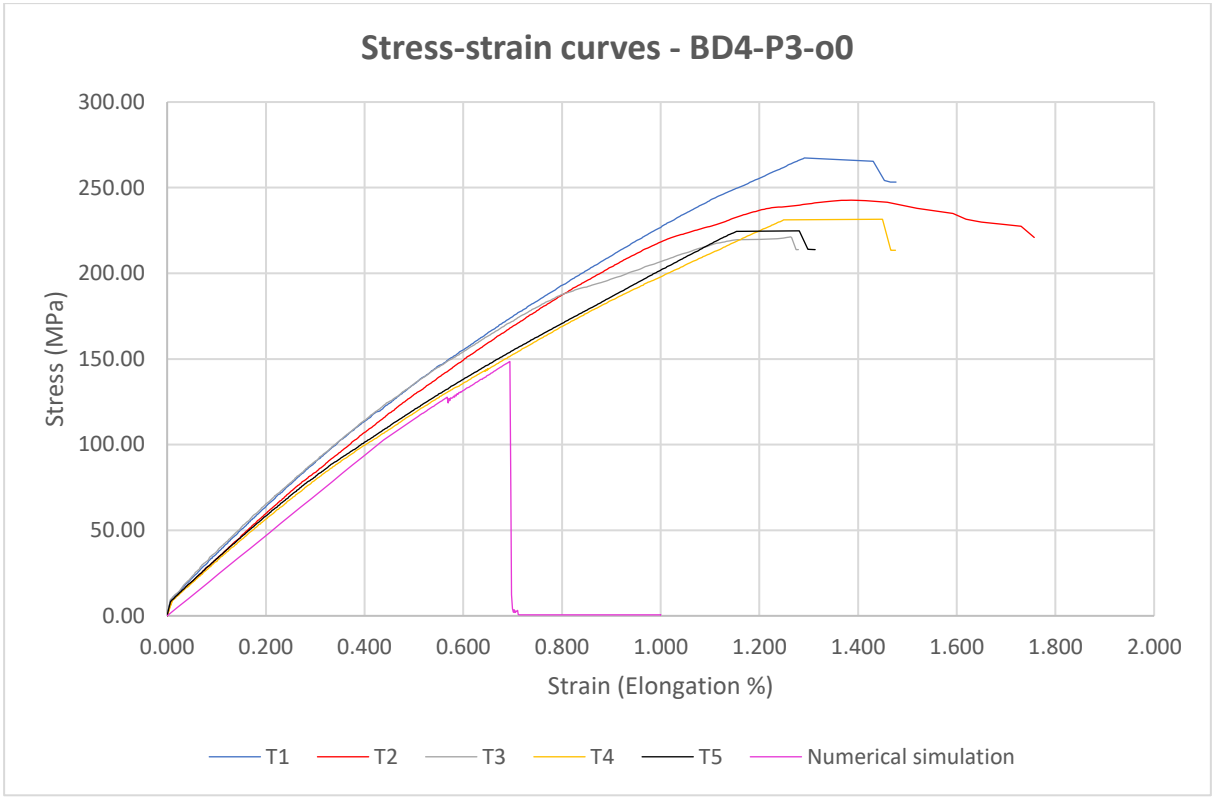


Figure 4.32: Experimental and simulated stress-strain curves for the aligned 3mm resin pocket length laminate

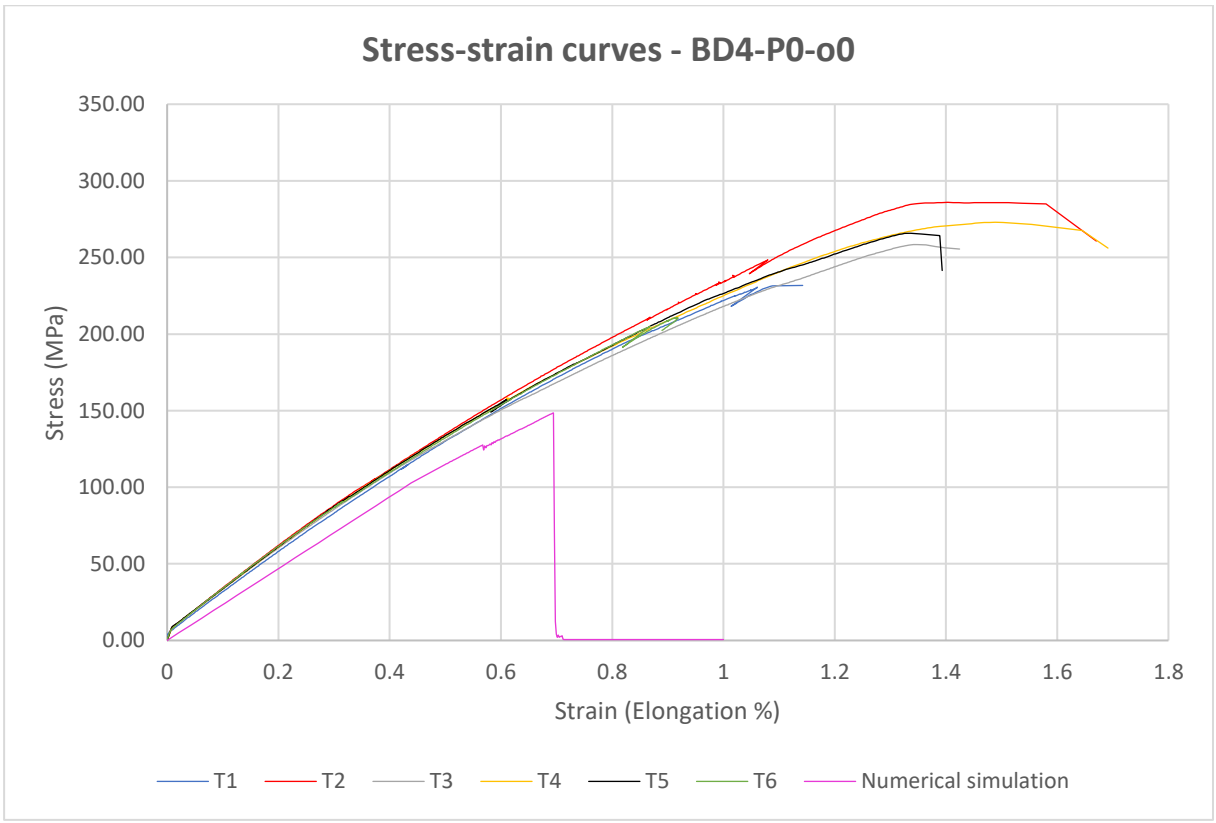


Figure 4.33: Experimental and simulated stress-strain curves for the aligned 0mm resin pocket length laminate

For the BD4-P3-o0 configuration, the experimental and numerical curves showed a similar initial tensile response, indicating that the elastic stiffness defined in the Abaqus model was reasonably representative of the real laminate behaviour, with the curvature of the curves being similar, and differing only in the engineering stresses for a given strain. However, the numerical simulation predicted failure at a significantly lower stress and strain than the experimental specimens, similarly to the load-displacement curves.

This discrepancy in simulated and experimental results can also be attributed to all the reasons mentioned previously, with the addition of the values of the cross-section areas that were used for the calculation of the engineering stress. For the numerical simulations, a cross-section area value of 108.5mm^2 was used for this calculation, due to the theoretical laminate thickness being equal to 4.34mm (see Eq. (3.18)). However, if Table 4.2 and Table 4.3 are analysed, the values of the cross-section area range from 77.735mm^2 to 84.853mm^2 in the case of the BD4-P3-o0 specimens and 74.346mm^2 to 84.088mm^2 in the case of the BD4-P0-o0 specimens. These smaller values are all due to the smaller thicknesses of the produced laminated specimens compared to the theoretical one, as the width of the cut laminate specimens was carefully controlled.

It is important to mention the spread of the results obtained experimentally between different specimens, most likely due to manufacturing variability associated with the reused glass fibre mats, including fibre waviness, local misalignment, thickness variation, contamination and manual cutting imperfections, which can affect the experimental response and explain the scatter observed between specimens.

Moreover, the overall performance of the BD4-P0-o0 ply joint configuration seems to be marginally better than the BD4-P3-o0 ply joint configuration, following the load-displacement numerically simulated theoretical elastic response more closely. This can be attributed to the mitigation of manufacturing defects that were directly caused by the resin pocket length, such as the external continuous glass fibre layer sagging that was experienced during the manufacturing of the BD4-P3-o0 laminate, as seen in Figure 4.18.

Analysing the failure mechanisms that were experienced in the test coupons, all of them behaved similarly. Firstly, mode II interlaminar delamination caused by shear sliding between adjacent plies was experienced between both central discontinuous layers and the outer continuous layers, always developing from the location of the resin pocket and progressing towards the extremities of the specimen where the end tabs were located. This progression of delamination happened until the tensile failure point

of the outer continuous layers was reached, at which point these ruptured, achieving overall laminate failure. Note that the inner layers have not experienced any form of delamination between them.



Figure 4.34: Delamination failure between inner discontinuous layers and outer continuous layers



Figure 4.35: Tensile failure of an outer continuous layer

This delamination mechanism is also observed in the numerical simulations, although not as progressive as the evolution experienced with the laminate specimens, as seen in Figure 4.36. Analysing the cohesive element degradation states shown in Figure 3.39, it can be assumed that the delamination propagation between the discontinuous inner layers and continuous outer layers starts at the resin pocket, as the areas at the corners of it are the ones that degrade the fastest. Similarly to the experimental results, no delamination was predicted between the inner composite plies in the numerical model.

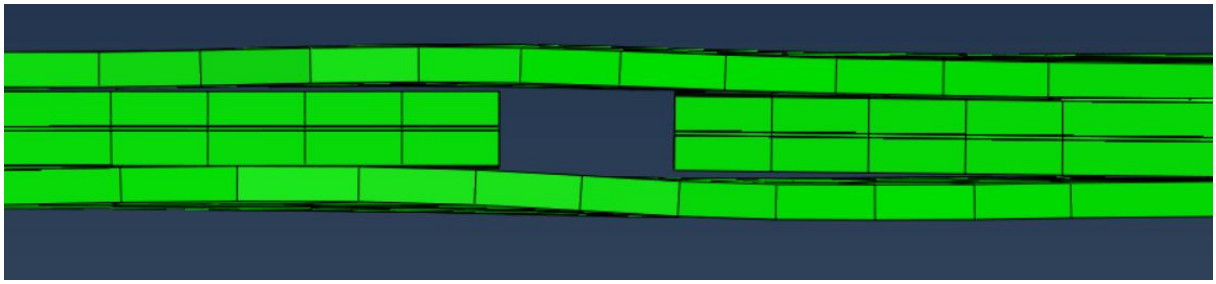


Figure 4.36: Delamination areas experienced in the numerically simulated aligned 3mm pocket length ply joint configuration

4.2.2. Stepped ply joint configuration

Before analysing the results obtained for the specimens of the stepped, 0mm resin pocket length, 10mm resin pocket gapped ply joint configuration laminate or BD4-P0-o10; it must be mentioned that specimens 1, 2 and 5 suffered end tab debondings during the first time they were tested.

An effort was made to rebond the detached end tabs and test the specimens once more, however, in the cases of test coupons 1 and 5, enough damage had been done to both specimen the first time they were testes before the debonding of the end tabs that the results obtained the second time they were tested were not valid, as they differed greatly from the expected behaviour of a pristine test coupon. As for specimen number 2, the initial behaviour seemed to follow the expected trend; however, composite material failure was experienced in the end tab area, likely caused by excessive sanding to flatten the local increases in thickness created by the attachment of the LUNA™ optic fibre strain sensors, which may have weakened the fibre reinforcement in that area. In Figure 4.37, the composite failure at the end tab area can be seen. For this reason, the results of this specimen were also deemed invalid for this study [70].



Figure 4.37: Composite material failure at the end tab gripping area

In Figure 4.38, the load-displacement curves of all the valid experiments can be seen and compared to the numerical simulation result curve.

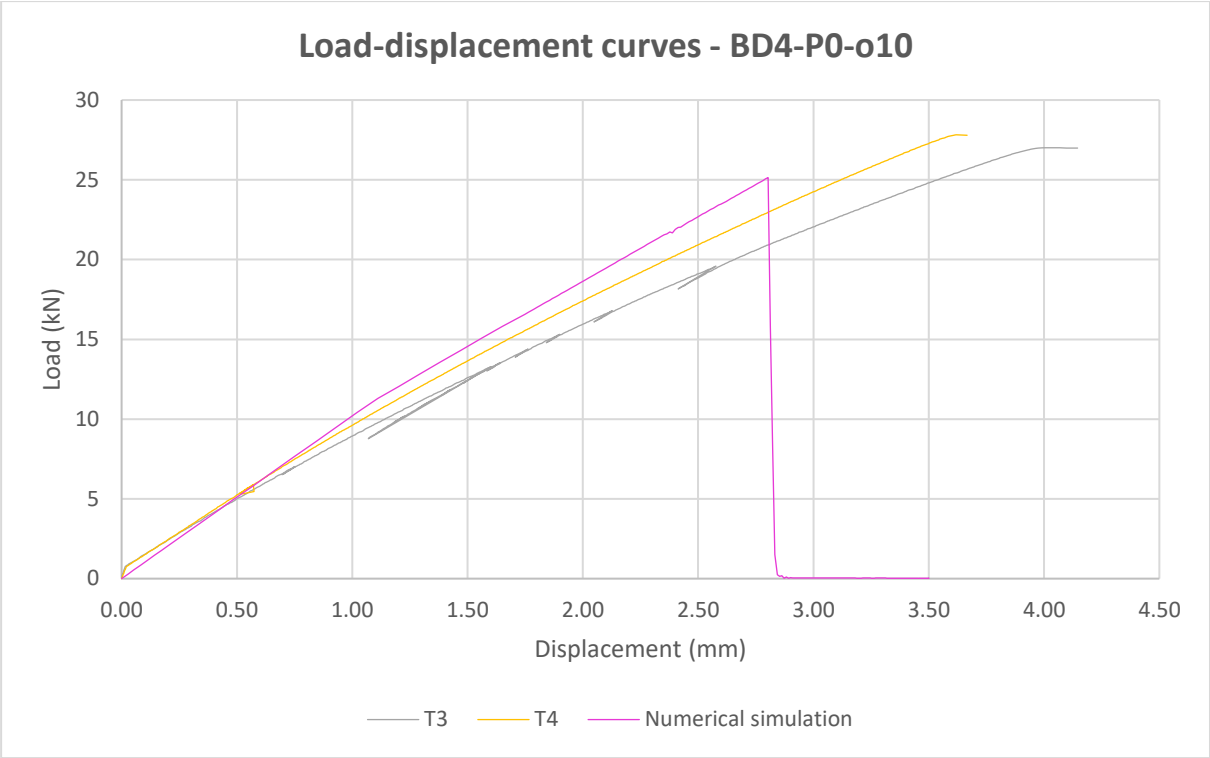


Figure 4.38: Experimental and simulated load-displacement curves for the stepped 0mm resin pocket length, 10mm gap between resin pockets laminate

The predicted behaviour of the numerical simulation follows the same trend as it did with the aligned ply joint configurations, showing a comparable initial tensile response, with a slightly conservative prediction of the point of failure compared to the experimental results obtained; with these deviating due to the suspected difference in progressiveness of damage initiation and softening of the materials.

However, with this ply joint configuration, the numerically simulated theoretical results seem to follow the theoretical response of the laminate more closely than its aligned configuration counterparts. This is suspected to be the case due to the failure of the cohesive elements being delayed by reducing the severity of the stress concentrations in critical areas compared to the engineering stress experienced by the simulated laminate in the critical ply joint parameter study, as seen in Table 3.14; where it is shown that the dominant stress ratios peak values are significantly reduced in the 10mm gap stepped ply joint configuration compared to the aligned one. Since the cohesive elements were the critical components that dictated the failure behaviour and point of the simulated laminate, this suggests that the prematurely predicted failure of the aligned configurations is mainly due to the incorrect strength property definition of the cohesive elements.

Analysing the load-displacement curve of the BD4-P0-o10-T3 specimen, the spiked deviations from the curve may have been caused by local delamination events, matrix cracking and possible end tab grip slippage; with this last one being the more probable cause due to the problems experienced with end tab bonding in other specimens of this kind.

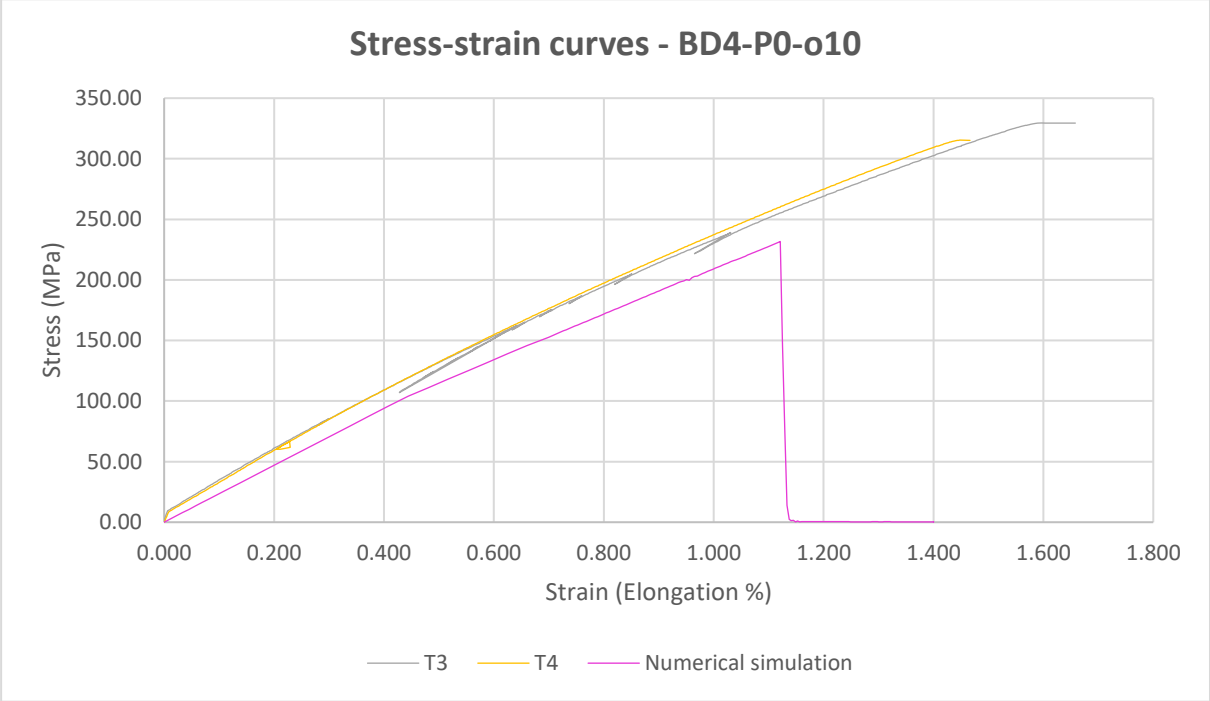


Figure 4.39: Experimental and simulated stress-strain curves for the stepped 0mm resin pocket length, 10mm gap between resin pockets laminate

Similarly to the aligned ply joint configurations, the curvature of the stress-strain curves is very similar, with the values of the stresses for any given strain varying due to both the discrepancy of the values of the cross-sectional areas used for the calculation of the engineering stress as well as the variation of the exerted load values for any given displacement.

Analysing the delamination mechanisms seen in Figure 4.40 of the stepped ply joint configurations experienced during the tensile tests of the specimens, the area between the two resin pockets delaminated fully, along with the usual delamination experienced between the inner discontinuous plies and outer continuous ones, originating from the area where the resin pockets are located and propagating towards the ends of the specimen. Mode II delamination is the main delamination type that is experienced in all areas where it occurs. In addition to these delaminations, complete laminate failure was achieved at the point of traction failure of the outer composite layers, similarly to the aligned ply joint configurations.



Figure 4.40: Delamination mechanisms experienced in all valid specimens of the BD4-P0-o10 ply joint configuration laminate coupons

Observing the behaviour predicted by the numerical model in Figure 4.41, the same delamination areas can be observed as in the experimental specimens; right between the resin pockets and between the inner and outer composite plies.

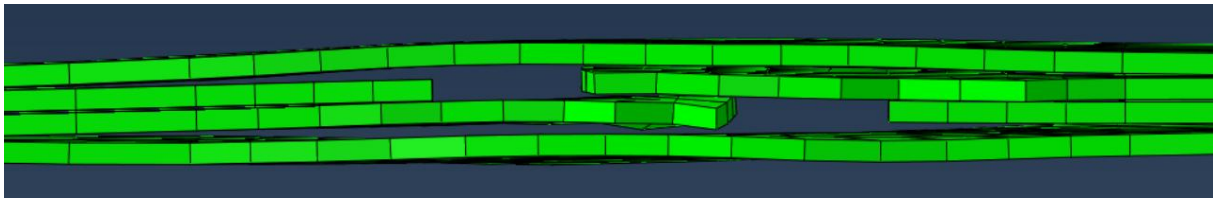


Figure 4.41: Delamination areas experienced in the numerically simulated stepped 10mm pocket gap length, 3mm pocket length ply joint configuration

Since it was determined in Section 3.4.1 that in stepped ply joint configurations, the most critical cohesive element was always the one positioned between the resin pocket, it can be deduced that delamination events all started from this point, matching the point of delamination origin of the specimens.

THIS PAGE WAS INTENTIONALLY LEFT BLANK

5. CONCLUSION AND FUTURE WORK

5.1. Overall conclusions

This MSc Dissertation investigated the mechanical feasibility of reusing discarded virgin glass fibre mat cut-outs generated during wind turbine blade manufacturing by joining them into larger composite laminate elements. The work was developed within the context of the CirWind project, where the reuse of composite waste for secondary and non-critical urban applications represents an opportunity to reduce material waste while preserving part of the original value of the reinforcement. The study combined Abaqus/CAE numerical simulations and experimental tensile tests in order to evaluate the influence of ply discontinuities, resin-rich pockets and interlaminar damage on the mechanical behaviour of end-to-end ply-joint configurations.

The numerical simulations showed that cohesive zone modelling is a useful strategy for analysing these joints. By combining composite continuum shell elements, Hashin damage criteria and cohesive elements, it was possible to identify the regions where stress concentrations, cohesive damage initiation and interlaminar degradation were most likely to occur. The results showed that failure was mainly governed by the cohesive regions located near the resin-rich pockets, confirming that the design of the ply terminations strongly affects the tensile performance of the laminate.

The resin pocket size study showed that, for the numerical conditions considered, changing the pocket length had only a limited effect on the global tensile response. The maximum load, failure displacement and maximum stress varied only slightly between the analysed cases. However, the stress-ratio analysis showed that the resin pocket geometry still influenced the local stress state around the discontinuity. Therefore, pocket size should be controlled during manufacturing, even though it was not the most influential parameter in the numerical study.

The distance between resin-rich pockets had a stronger influence on the mechanical response. Increasing the gap between discontinuities reduced the main stress concentrations and delayed cohesive damage initiation. The improvement became less significant beyond a normalised gap length of approximately ten times the ply thickness, indicating that this value represented a practical compromise between mechanical performance and joint length for the studied geometry and material properties. In contrast, the aligned configuration produced the weakest response, showing that placing resin-rich pockets directly above one another creates a critical through-thickness weakness and should generally be avoided.

The comparison between the complex end-to-end configurations showed that the symmetric interleaved misaligned scarf configuration provided the best numerical performance. This configuration achieved the highest maximum load and engineering stress, although the difference with the other complex configurations was relatively small. The results suggest that distributing the resin pockets through the laminate length and thickness improves load transfer and reduces the risk of forming a single dominant delamination path.

The experimental programme confirmed that laminates can be manufactured from reused glass fibre waste mats but also showed the practical limitations of this material stream. The mats presented imperfections such as waviness, twisting, fibre misalignment, frayed edges, contamination and thickness variations. These factors, together with manual preparation of the discontinuities and vacuum infusion variability, contributed to the scatter observed between nominally identical specimens. The comparison between experimental and numerical results showed that the Abaqus models reproduced the general initial stiffness trend of the tensile tests but predicted a more brittle and conservative failure response. The simulations generally failed at lower displacement and, in some cases, lower load than the experimental specimens. This discrepancy was mainly attributed to the use of material and damage properties obtained from literature and online datasheets rather than from direct characterisation of the manufactured laminates, as well as to the idealised representation of the resin pocket geometry and cohesive interface.

Overall, the results show that end-to-end ply joints made from reused glass fibre mats can be engineered to improve their mechanical response. The most important design conclusions are that resin-rich pockets should be controlled, sufficient spacing should be provided between discontinuities, and through-thickness alignment should be avoided.

5.2. Future works

Future work should focus first on improving the experimental characterisation of the reused glass fibre/epoxy material. In the present work, several numerical material properties were obtained from literature and online datasheets because the simulations were developed before the complete experimental campaign. Although this allowed a functional Abaqus/CAE model to be created, the accuracy of the numerical predictions could be improved by directly measuring the elastic properties, tensile and compressive strengths, shear strengths, fracture energies, density and fibre volume fraction of the manufactured laminates.

A second important future task is the calibration of the numerical damage models. The comparison between the experimental and numerical curves showed that the simulations reproduced the general stiffness trend, but predicted a more brittle and conservative failure response. Therefore, the Hashin damage parameters and cohesive zone properties should be adjusted using experimental results from the actual material system. This calibration should not be based only on maximum load, but also on failure displacement, damage sequence, delamination location and the shape of the load–displacement and stress–strain curves.

The real geometry of the resin-rich pockets should also be studied in more detail. In the numerical models, the resin pockets and ply discontinuities were represented using idealised geometries, while the manufactured specimens may have contained rounded edges, fibre bridging, local waviness, imperfect alignment and variations in resin distribution. Future work should include microscopic inspection or cross-section analysis of the tested specimens to measure the real pocket size, shape and through-thickness alignment. This information would allow the numerical models to represent the manufactured laminates more accurately.

A larger experimental campaign should also be carried out to increase the statistical reliability of the results. Since the glass fibre mats were obtained from wind turbine blade manufacturing waste, the material presented higher variability than new commercial reinforcement, including waviness, twisting, contamination, frayed edges and fibre misalignment. Testing a larger number of specimens for each configuration would make it possible to better quantify this variability and determine whether the observed trends remain consistent.

Finally, future studies should investigate additional joint configurations and manufacturing improvements. More complex staggered, scarf and interleaved arrangements could be tested experimentally, especially those that avoid through-thickness alignment of resin-rich pockets. The influence of manufacturing parameters, such as cutting precision, fibre positioning, vacuum infusion quality and resin pocket control, should also be analysed. These improvements would help transform the numerical model from a preliminary comparison tool into a more reliable design method for composite components manufactured from reused wind turbine blade glass fibre waste.

THIS PAGE WAS INTENTIONALLY LEFT BLANK

6. REFERENCES

[1] L. M. Jr., «Sustainable End-of-Life Management of Wind Turbine Blades: Overview of Current and Coming Solutions,» *MDPI,* vol. 14, n° 5, p. 25, February 2021.

[2] J. Qureshi, "A Review of Recycling Methods for Fibre Reinforced Polymer Composites," *MDPI,* vol. 14, no. 24, p. 22, December 2022.

[3] J. Y. F. M. L. Z. e. a. Jonathan M Cullen, «Solutions for recycling emerging wind turbine blade waste in China are not yet effective,» *Communications Earth & Environment,* vol. 4, n° 1, p. 15, December 2023.

[4] C. Y. B. Pu Liu, «Wind turbine blade waste in 2050,» *Waste Management - Elsevier,* vol. 62, p. 12, April 2017.

[5] M. F. D. M. R. Gisela Mello, «Wind farms life cycle assessment review: CO_2 emissions and climate change,» *Energy Reports - Elsevier,* Vols. %1 de %26 - 8, p. 6, December 2020.

[6] K. B. H. N. P. J. B. M. M. a. B. F. S. L. Mishnaevsky Jr., «Materials for wind turbine blades: An overview,» *Materials - MDPI,* vol. 10, n° 11, p. 24, November 2017.

[7] S. R. B. Wieland, «Process modelling of composite materials for wind-turbine rotor blades: Experiments and numerical modelling,» *Materials - MDPI,* vol. 10, n° 10, p. 12, October 2017.

[8] A. Hindersmann, «Experimental investigation of a method to avoid channel marks during vacuum infusion,» *Journal of Composite Materials,* vol. 54, n° 18, p. 12, November 2019.

[9] B. L. C. B. B. Purgleitner, «Investigation of shredded glass fibre composites from post-industrial and post-consumer waste from wind turbine blades for reuse in structural epoxy resin plates,» *Fibres - MDPI,* vol. 14, n° 5, p. 13, April 2026.

[10] L. O. D. G. A. L. G. Oliveux, «Current status of recycling of fibre reinforced polymers: Review of technologies, reuse and resulting properties,» *Progress in Materials Science,* vol. 72, p. 39, July 2015.

[11] S. J. Pickering, «Recycling technologies for thermoset composite materials—current status,» *Composites Part A: Applied Science and Manufacturing,* vol. 37, n° 8, p. 10, August 2006.

[12] Y. D. K. V. A. W. D. J. R. Duflou, "Do fibre-reinforced polymer composites provide environmentally benign alternatives? A life-cycle-assessment-based study," *MRS Bulletin,* vol. 37, no. 4, pp. 374-382, April 2012.

[13] B. F. R. B. J. Joustra, «Structural reuse of high-end composite products: A design case study on wind turbine blades,» *Resources, Conservation and Recycling,* vol. 167, n° 105393, p. 10, April 2021.

[14] J. C. M. N. C. M. P. S. R. C. P. J. A. L. R. M. Novais, «Incorporation of glass fibre fabrics waste into geopolymer matrices: An eco-friendly solution for off-cuts coming from wind turbine blade production,» *Construction and Building Materials,* vol. 187, pp. 876-883, October 2018.

[15] S. T. d. F. J. Kupski, «Design of adhesively bonded lap joints with laminated CFRP adherends: Review, challenges and new opportunities for aerospace structures,» *Composite Structures,* vol. 268, n° 113923, p. 13, July 2021.

[16] C. K. C. I. K. H. K. N. C. J. S. Chou, «Failure analysis of wind turbine blade under critical wind loads,» *Engineering Failure Analysis - Elsevier,* vol. 27, p. 20, January 2013.

[17] P. B. V. J. Alzamora Guzman, «Effects of moisture on glass fibre-reinforced polymer composites,» *Journal of Composite Materials,* vol. 49, n° 8, p. 10, March 2014.

[18] J. Y. W. H. Z. J. W. S. J. J. E. T. A. S. Verma, «A review of impact loads on composite wind turbine blades: Impact threats and classification,» *Renewable and Sustainable Energy Reviews,* vol. 178, n° 113261, p. 23, May 2023.

[19] J. Ahamed, «Hybrid composite ply joints for integrating radiofrequency apertures in multifunctional aircraft structures,» *RMIT University,* p. 161, July 2018.

[20] J. P. T. W. R. P. M. A. S. Q. J. N. Baucom, «Tiled composite laminates,» *Journal of Composite Materials,* vol. 44, n° 26, pp. 3115-3132, 2010.

[21] M. Y. R. S. T. I. P. B. R. Malkin, «Bio-inspired laminate design exhibiting pseudo-ductile (graceful) failure during flexural loading,» *Composites Part A: Applied Science and Manufacturing,* vol. 54, pp. 107-116, 2013.

[22] M. R. W. S. R. H. B. G. Green, «Effect of stacking sequence on open-hole tensile strength of composite laminates,» *Composites Part A: Applied Science and Manufacturing,* vol. 38, n° 3, p. 867–878, 2007.

[23] R. D. a. G. F. J. H. M. R. Wisnom, «Delamination in asymmetrically tapered composites loaded in tension,» *Composite Structures,* vol. 35, n° 3, p. 309–322, 1996.

[24] C. G. D. M. F. d. M. P. P. Camanho, «Numerical simulation of mixed-mode progressive delamination in composite materials,» *Journal of Composite Materials,* vol. 37, n° 16, p. 1415–1438, 2003.

[25] M. R. W. M. J. W. Cui, «Effect of step spacing on delamination of tapered laminates,» *Composites Science and Technology,* vol. 52, n° 1, p. 39–46, 1994.

[26] F. K. A. A. A. S. A. E. U. S. V. L. B. N. Fedulov, «Influence of fibre misalignment and voids on composite laminate strength,» *Journal of Composite Materials,* vol. 49, n° 24, p. 2887–2896, 2015.

[27] C. G. D. P. P. C. J. C. A. Turon, «An engineering solution for mesh size effects in the simulation of delamination using cohesive zone models,» *Engineering Fracture Mechanics,* vol. 74, n° 10, p. 1665–1682, 2007.

[28] D. S. -. A. 2. Documentation, "Explicit dynamic analysis," Dassault Systèmes, 2024. [Online]. Available: https://docs.software.vt.edu/abaqusv2024/English/SIMACAEANLRefMap/simaanl-c-expdynamic.htm. [Accessed July 2026].

[29] D. S. -. A. 2. Documentation, "Quasi-static analysis with Abaqus/Explicit," Dassault Systèmes, 2025. [Online]. Available:

https://docs.software.vt.edu/abaqusv2025/English/SIMACAEGSARefMap/simagsa-m-Quasi-sb.htm. [Accessed July 2026].

[30] D. S. -. A. 2. Documentation, "Types of problems suited for Abaqus/Explicit," Dassault Systèmes, 2025. [Online]. Available: https://docs.software.vt.edu/abaqusv2025/English/SIMACAEGSARefMap/simagsa-c-ovwtypes.htm. [Accessed July 2026].

[31] D. S. -. A. 2. Documentation, "Defining the constitutive response of cohesive elements using a traction-separation description," Dassault Systèmes, 2024. [Online]. Available: https://docs.software.vt.edu/abaqusv2024/English/SIMACAEELMRefMap/simaelm-c-cohesivebehavior.htm. [Accessed July 2026].

[32] D. S. -. A. 2. Documentation, "About Cohesive Elements," Dassault Systèmes, 2024. [Online]. Available: https://docs.software.vt.edu/abaqusv2024/English/SIMACAEELMRefMap/simaelm-c-cohesiveoverview.htm. [Accessed July 2026].

[33] I. I. S. S.-S. E. J. B. L. M. Fernández-Cañadas, «Effect of adhesive thickness and overlap on the behaviour of composite single-lap joints,» *Mechanics of Advanced Materials and Structures,* vol. 28, n° 11, pp. 111-1120, 2019.

[34] Z. S. J.W. Hutchinson, «Mixed Mode Cracking in Layered Materials,» *Advances in Applied Mechanics,* vol. 29, pp. 63-191, 1991.

[35] C. G. D. Pedro P. Camanho, «Mixed-Mode Decohesion Finite Elements for the Simulation of Delamination in Composite Materials,» *NASA/TM-2002-211737,* pp. 1-37, 2002.

[36] F. A. Geminiano Mancusi, «Failure Criteria for FRP Adhesive Lap Joints: A Comparative Analysis,» *Mechanics of Advanced Materials and Structures,* vol. 17, n° 2, pp. 157-164, 2017.

[37] D. S. -. A. 2. Documentation, "Maximum or quadratic nominal stress damage," Dassault Systèmes, 2024. [Online]. Available: https://docs.software.vt.edu/abaqusv2024/English/SIMACAECAERefMap/simacae-t-prpmechanicaldamagemaxquads.htm. [Accessed July 2026].

[38] M. K. M. L. Benzeggagh, «Measurement of mixed-mode delamination fracture toughness of unidirectional glass/epoxy composites with mixed-mode bending apparatus,» *Composites Science and Technology,* vol. 56, nº 4, p. 439–449, 1996.

[39] R. Bouallala, "Mechanical performance of adhesively bonded innovative aeronautic carbon composites," *European Master Course in Advanced Structural Analysis and Design using Composite Materials,* pp. 1-111, 2023.

[40] D. S. -. A. 2. Documentation, "About Progressive Damage and Failure," Dassault Systèmes, 2024. [Online]. Available: https://docs.software.vt.edu/abaqusv2024/English/SIMACAEMATRefMap/simamat-c-damageoverview.htm. [Accessed August 2026].

[41] C. G. D. D. G. F. A. Leone, «Progressive damage analysis as a design tool for composite bonded joints,» *Composites Part B: Engineering,* vol. 77, p. 474–483, 2015.

[42] D. S. -. A. 2. Documentation, «Energy balance», Dassault Systèmes, 2024. [En línea]. Available: https://docs.software.vt.edu/abaqusv2024/English/SIMACAEGSARefMap/simagsa-c-qsienergybal.htm. [Último acceso: agosto 2026].

[43] D. S. -. A. 2. Documentation, "Strategy for evaluating the results," Dassault Systèmes, 2017. [Online]. Available: https://abaqus-docs.mit.edu/2017/English/SIMACAEGSARefMap/simagsa-c-strategyforevaluatingtheresults.htm. [Accessed August 2026].

[44] D. S. -. A. 2. Documentation, "Output of the energy balance," Dassault Systèmes, 2025. [Online]. Available: https://docs.software.vt.edu/abaqusv2025/English/SIMACAEGSARefMap/simagsa-c-ovwoutput.htm. [Accessed August 2026].

[45] M. Composites, "Biaxial (0°/90°) Fibreglass," Matex Composites, 2023. [Online]. Available: https://www.matex-frp.com/biaxial-090-2-product/. [Accessed August 2026].

[46] K. F. J. M. B. D. Främby, «Adaptive modelling of delamination initiation and propagation using an equivalent single-layer shell approach,» *International Journal for Numerical Methods in Engineering,* vol. 112, nº 8, p. 882–908, 2017.

[47] B. S. Publication, "China Gauges," 2023. [Online]. Available: https://www.china-gauges.com/Uploads/download/6527ab8b22858.pdf. [Accessed August 2026].

[48] F. Silva, "Scribd - Materiais Têxteis para Construção Pesada," Enercon GmbH, 2015. [Online]. Available: https://es.scribd.com/document/671110797/TD-Esc-02-de-en-10-050-Rev003-Overview-of-Woven-non-Woven-Fabrics-and-Mats. [Accessed August 2026].

[49] D. S. -. A. 2. Documentation, "Modelling with Cohesive Elements," Dassault Systèmes, 2024. [Online]. Available: https://docs.software.vt.edu/abaqus/v2024/English/SIMACAEELMRefMap/simaelm-c-cohesiveusage.htm. [Accessed August 2026].

[50] D. S. -. A. 2. Documentation, "Defining the Cohesive Element's Initial Geometry," Dassault Systèmes, 2024. [Online]. Available: https://docs.software.vt.edu/abaqus/v2024/English/SIMACAEELMRefMap/simaelm-c-cohesiveinit.htm. [Accessed August 2026].

[51] Z. O. G. L. G. Ji, «Effects of bondline thickness on Mode-I nonlinear interfacial fracture of laminated composites: An experimental study,» *Composites Part B: Engineering,* vol. 47, p. 1–7, 2013.

[52] Z. O. G. L. G. Ji, «Effects of bondline thickness on Mode-II interfacial laws of bonded laminated composite plate,» *International Journal of Fracture,* vol. 168, n° 2, p. 197–207, 2011.

[53] M. M. Y. Z. M. M. Y. Z. M. Y. Zaghloul, «Influence of Stress Level and Fibre Volume Fraction on Fatigue Performance of Glass Fibre-Reinforced Polyester Composites,» *Polymers,* vol. 14, n° 13, p. Art. no. 2662, 2022.

[54] M. M. P. Data, "E-Glass Fibre, Generic," MatWeb, [Online]. Available: https://www.matweb.com/search/datasheet_print.aspx?matguid=d9c18047c49147a2a7c0b0bb1743e812. [Accessed August 2026].

[55] S. C. -. P. Datasheet, "SR InfuGreen 810 / SD 882X: Green Epoxy systems for injection and infusion," Sicomin Composites, July 2023. [Online]. Available: https://sicomin.com/fiches-techniques/srInfuGreen810_sd882x.pdf. [Accessed August 2026].

[56] S. Topics, "Shear Modulus - an overview," ScienceDirect, [Online]. Available: https://www.sciencedirect.com/topics/engineering/modulus-of-shear. [Accessed August 2026].

[57] F. T. D. V. E. Jacquet, «Calculation of the transverse modulus of a unidirectional composite material and of the modulus of an aggregate. Application of the rule of mixtures,» *Composite Structures,* vol. 50, n° 1, p. 1–12, 2000.

[58] C. C. Chamis, «Simplified composite micromechanics equations for hygral, thermal and mechanical properties,» *NASA Lewis Research Centre, Cleveland, OH, USA, NASA TM-83320, E-1561,* 1983.

[59] C. V. V. A. H. Cardon, «Some Models for the Transverse Creep and Damage Behaviour of a Unidirectional Reinforced Polymer Matrix Composite,» *Progress and Trends in Rheology V,* p. 435–436, 1998.

[60] D. Zenkert, The Handbook of Sandwich Construction, Cradley Heath: EMAS Publishing, 1997.

[61] H. N. D. C. A. F. D. Y. P. C. L. C. J. A. B. U. K. K. Giasin, «Effect of fibre orientation on impact damage resistance of S2/FM94 glass fibre composites for aerospace applications: An experimental evaluation and numerical validation,» *Polymers,* vol. 14, n° 1, p. Art. 95, 2022.

[62] X. Z. Y. G. B. Liu, «Multi-scale analysis for assessing the impact of material composition and weave on the ultimate strength of GFRP stiffened panels,» *Journal of Marine Science and Engineering,* vol. 14, n° 1, p. Art. 108, 2023.

[63] W. G. L. A. G. T. C. A. C. J. S. K. H. T. H. L. Pinto, «Experimental and numerical comparison of impact behaviour between thermoplastic and thermoset composite for wind turbine blades,» *Materials,* vol. 14, n° 21, p. Art. 6377, 2021.

[64] M. P. Falaschetti, «Experimental and numerical evaluation of impact damage tolerance in composite materials,» *Alma Mater Studiorum Università di Bologna - PhD dissertation,* 2017.

[65] K. F. Y. C. G. Wei, «Crashworthiness and Failure Analyses of FRP Composite Tubes under Low Velocity Transverse Impact,» *Sustainability,* vol. 15, n° 1, p. Art. 56, 2023.

[66] H. M. W. S. L. R. Z. Jiang, «Modelling delamination of FRP laminates under low velocity impact,» *IOP Conference Series: Materials Science and Engineering,* n° 242, p. Art. 012088, 2017.

[67] D. S. -. A. 2. Documentation, "Three-dimensional structured meshing," Dassault Systèmes, 2025. [Online]. Available: https://docs.software.vt.edu/abaqusv2025/English/SIMACAECAERefMap/simacae-c-mgnconcmapped3d.htm. [Accessed August 2026].

[68] D. S. -. A. 2. Documentation, "What is mapped meshing?," Dassault Systèmes, 2024. [Online]. Available: https://docs.software.vt.edu/abaqus/v2024/English/SIMACAECAERefMap/simacae-c-mgnconcmappeddifference.htm. [Accessed August 2026].

[69] H. S. K. S. Khalid, «Progressive damage modelling of inter- and intra-laminar damages in open hole tensile composite laminates,» *Journal of the Computational Structural Engineering Institute of Korea,* vol. 32, n° 4, p. 233–240, 2019.

[70] A. International, *ASTM D3039/D3039M-17(2025), Standard Test Method for Tensile Properties of Polymer Matrix Composite Materials,* West Conshohocken, PA, USA, 2025.

[71] R. M. Jones, Mechanics of Composite Materials, 2 ed., Philadelphia, PA, USA: Taylor & Francis, 1999.

[72] B. V. A. Mukherjee, «Design guidelines for ply drop-off in laminated composite structures,» *Composites Part B: Engineering,* vol. 32, n° 2, p. 53–164, 2001.

[73] A. V. K. M. B. R. Vidyashankar, «Analysis of laminates with ply drops,» *Composites Science and Technology,* vol. 61, n° 5, p. 749–758, 2001.

[74] R. G. S. V. H. K. He, «Modified shear-lag model for analysis of a composite laminate with drop-off plies,» *Composites Science and Technology,* vol. 63, n° 10, p. 1453–1462, 2003.

[75] A. A. A. T. M. F. D. F. G. G. Corrado, «Mesoscale model for composite laminates: Verification and validation on scaled un-notched laminates,» *Polymers,* vol. 16, n° 12, Art. no. 1659, 2024.

[76] H. Y. F. L. D. Y. M. Xing, «An experimental study of failure mechanisms in laminates with dropped plies,» *Composites Science and Technology,* vol. 59, n° 10, p. 1527–1531, 1999.

[77] G. -. P. 3. F. g. Datasheet, "East Coast Fibreglass Supplies," [Online]. Available: https://www.ecfibreglasssupplies.co.uk/user/TechnicalDataSheet/100157.pdf?srsltid=AfmBOooB8HA6WpeTSF8zaW9gKXhhnyGc3yNyRNN0ZHHZbr1q8E8uJy3x. [Accessed August 2026].

[78] L. Innovations, "Fiber-Optic Strain Sensing," Luna, [Online]. Available: https://www.lunainc.com/capability/strain. [Accessed August 2026].

[79] CEYS, "Araldite Main Page," CEYS, 2026. [Online]. Available: https://www.go-araldite.com/es. [Accessed August 2026].

[80] L. T. B. Pan, «Advanced video extensometer for non-contact, real-time, high-accuracy strain measurement,» *Optics Express,* vol. 24, n° 17, p. 19082–19093, 2016.

[81] MTS, "MTS Exceed Electromechanical Test Systems," 2026. [Online]. Available: https://www.mts.com/en/products/materials/static-materials-test-systems/exceed-electromechanical. [Accessed August 2026].

[82] E. Technology, "Averaging Axial Extensometer, Model 3442AVG," Epsilon Technology, [Online]. Available: https://www.epsilontech.com/products/averaging-axial-extensometer-model-3442avg. [Accessed August 2026].

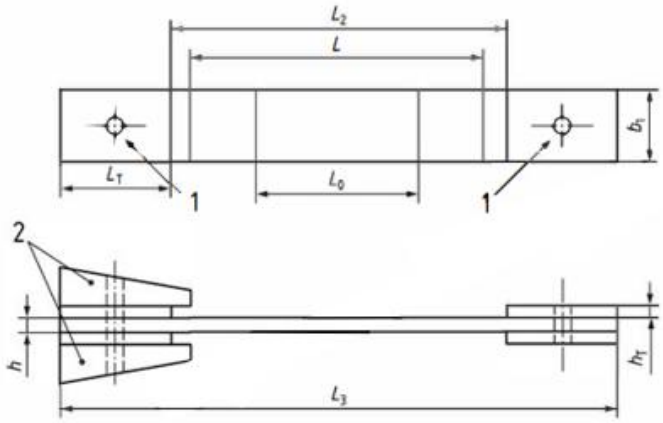
[83] TestResources, "ASTM D3039 Tensile Testing of Polymer Matrix Composite Materials," TestResources, 2026. [Online]. Available: https://www.testresources.net/applications/standards/astm/astm-d3039-tensile-testing-for-advanced-composite-materials. [Accessed August 2026].

THIS PAGE WAS INTENTIONALLY LEFT BLANK

ANNEX A

Presented in Annex A, the ISO 527-4:2023 norm for the determination of tensile properties of plastics, defining the test conditions for isotropic and orthotropic fibre-reinforced plastic composites specifies all the parameters that should be met when performing tensile tests for composite laminates. Here, the most important parameters have been compiled [47].

Overall geometry of the laminate specimen:



Key

1 centrings holes (optional), ϕD

2 jaws

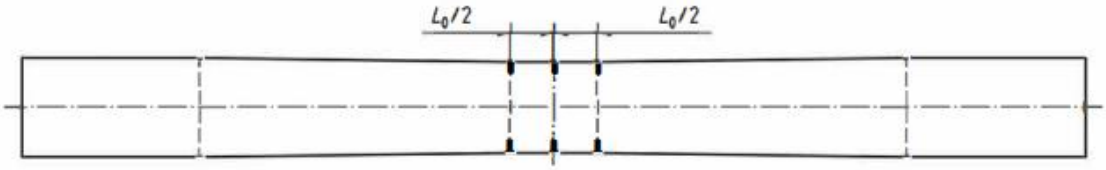
Symbol	Name	Dimensions in millimetres	
		Type 2	Type 3
L_3	Overall length	≥250	≥250
L_2	Distance between end tabs	—	150 ± 1
b_1	Width	25 ± 0,5 or 50 ± 0,5	25 ± 0,5 or 50 ± 0,5
h	Thickness	2 to 10	2 to 10
L_0	Gauge length (recommended for extensometers)	50 ± 1	50 ± 1
L	Initial distance between grips (nominal)	150 ± 1	150 ± 1
L_T	Length of end tabs	—	≥50
h_T	Thickness of end tabs	—	1 to 3
D	Diameter of centring holes	3 ± 0,25	3 ± 0,25

NOTE Requirements on specimen quality and parallelism are given in ISO 527-1:2019, 6.4.

Measurement points for the cross-section of the laminate specimen calculations:

The gauge marks shall conform to ISO 527-1:2019, 6.3.

Mark the parallel mid-section of the specimen when using specimen type 4. The first mark indicates the centre of the parallel mid-section. Two additional marks shall be placed in a distance of 12,5 mm from the centre (see Figure 6). The marks indicate the width and thickness measurement points of the specimen. In addition, the outer marks indicate the extensometer placement positions.



Speed of testing:

a) 5 mm/min for routine quality control;

b) 2 mm/min for qualification tests:

— when measuring the maximum elongation,

— when determining the tensile modulus of elasticity.